Design and Fabrication of Microoptical Elements in Sol-gel Glass For Photonics Applications

Yu Weixing

School of Electrical & Electronic Engineering

A thesis submitted to the Nanyang Technological University
in fulfillment of the requirement for the degree of
Doctor of Philosophy

2005

Statement of Originality

I hereby certify that the work embodied in this thesis is the result of original research and has not been submitted for a higher degree to any other university of institution.

05/05/2005

Date

Yu Weixing

Acknowledgments

There are many people who had assisted me to overcome many difficulties that I have encountered during my PhD study. I will like to take this opportunity to express my sincere appreciation to these people who had rendered great help to me in my research.

The first person I will like to express my gratitude to is my supervisor, Prof. Yuan Xiaocong, Larry. Prof Yuan had given me a thorough guidance during my entire research work. He has a wide knowledge in the optical field and is always pursuing researches that are in the forefront of optical technologies. What I have acquired from him is not only knowledge, but also methodologies in research. In addition, his professional attitude towards work and other things in life also benefits me greatly.

Next, I will like to express my appreciation to my family, namely my parents, my wife, and my siblings. It is their endless love that inspires me whenever I felt confused and depressed. I know that I must work hard so as not to disappoint them and hopefully, I will be able to provide them with a better life in future.

The third group of people I will like to thank is the technicians of Photonics Lab and Characterization Lab who had given me great help in my research.

Last but not least, I will like to thank all my friends who stood by me all these years.

Summary

Nowadays, optical communications have received great interest in industries due to its great communicating velocity and capacity and this has affected our daily lives significantly. All optical networks are being developed and it could become the next generation's communication method. At the same time, photonics is becoming more and more popular and has found applications in many fields such as optical communications, biophotonics and many others. With these tendencies, it will be very meaningful to fabricate microoptical elements cost-effectively. In addition, the discovery and expansion of its application in photonics and optical communications will be very exciting.

Along with these aims, we condense the solution into one simple objective, which is to lower the cost of microoptical elements. To achieve this, there are two ways. Firstly, we can develop a cost-effective optical material that can be used to fabricate microoptical elements. Next, we can also simplify and accelerate the fabrication process. Photosensitive hybrid sol-gel glass is a two-in-one solution to lower the cost of microoptical elements. This is because that it is a cost-effective optical material and the fabrication of microoptical elements only involves a single step.

In this thesis, a new recipe of SiO_2/TiO_2 photosensitive hybrid sol-gel glass that has great optical properties and a simple mass fabrication of microlens method have been developed.

With this new material, the traditional dry etching process is eliminated. Various facilities including contact imprinting with a gray scale mask, laser direct writing technique, electron beam lithography and holographic interference method are employed to fabricate microoptical elements including blazed gratings and refractive microlenses.

In our investigation, microoptical elements can be fabricated with two methods. One is the development-based method and the other is the self-development method. With the latter, high quality microoptical elements with smooth surface profiles can be obtained.

Next, a soft lithography method employing a polydimethylsiloxane (PDMS) elastic replica was developed to fabricate thick microoptical elements. With this method, a higher numerical aperture microlens was fabricated.

In addition, the fabricated sol-gel microlens was characterized by optical methods. Its focal length, point spread function and modulation transfer function were measured and compared with the theoretical ones.

Finally, we applied the fabricated high numerical aperture sol-gel microlens for fibre coupling. The whole coupling system was evaluated with Code V optical design software. The maximum coupling efficiency of the microlens designed with Code V can be up to 96%. The measured value of coupling efficiency is 60%, which is limited by the resolution of 10 micron of the alignment setup.

Although we have demonstrated the great potential of using photosensitive sol-gel glass to fabricate microoptical elements, much work is still needed to make the material more reliable and commercially available.

Table of contents

List of figures

List of tables

Chapter 1. Introduction

1.1. Motivation

With the fast development of photonics technologies, diffractive optics and micro-optics have been playing more and more important roles in photonics applications such as optics communications and bio-photonics. Microoptical elements such as microlenses have been used as key elements in many microoptical systems and applied in areas including optical coupling, optical interconnection and many others. When microlens is used as a coupler, it can improve the coupling efficiency from laser diode to optical fibre [1-2], optical fibre to optical fibre [3], optical fibre to waveguide, optical fibre to detector and other configurations. As most of the microoptical elements have continuous or multilevel surface relief structures, conventional methods like laser direct writing, electron beam lithography, multi-step binary masks and a grey scale mask have been used for the fabrication of such continuous structures. Figures 1-1 to 1-3 give a brief description of these methods. It is known that the first two methods are flexible and suitable to fabricate customized elements while the third method is suitable for mass production. However, all these three methods need several fabrication steps, where the first step involves the pattern generation in photoresist, and the last step is usually a dry etching process that makes permanent structures in the substrate.

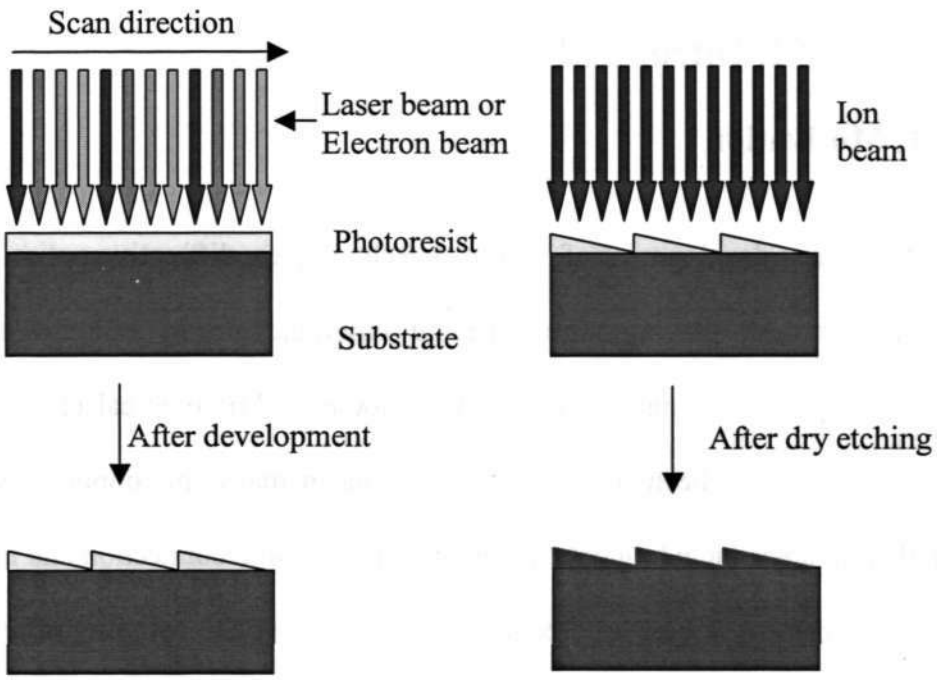

Figure 1-1: Fabrication of multi-level structures by varying dosage of laser beam or electron beam.

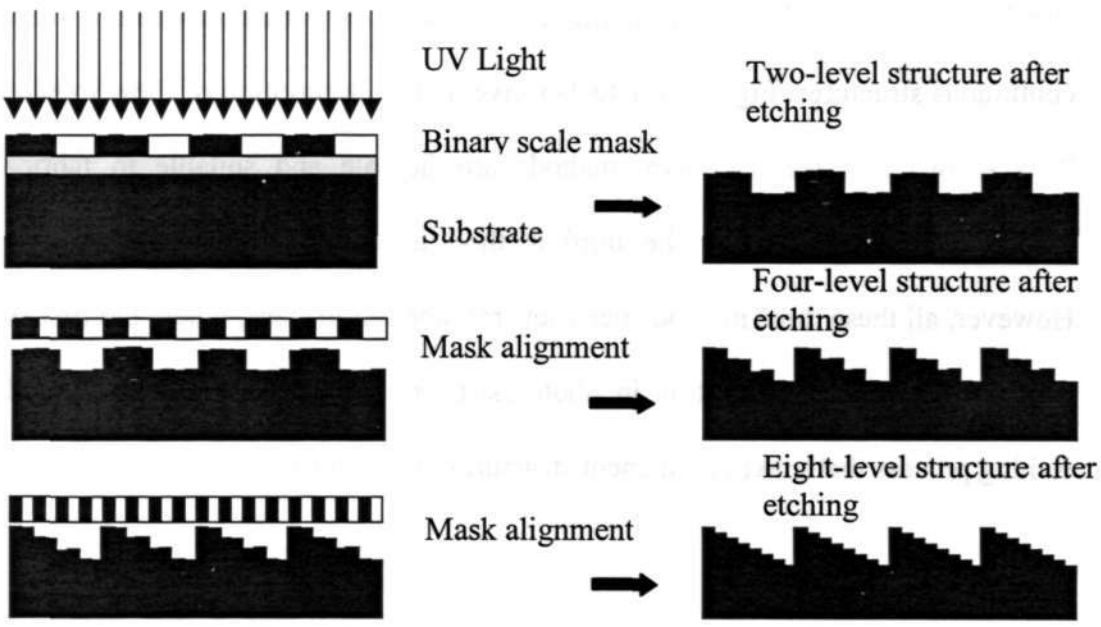

Figure 1-2: Fabrication of multilevel structures by multi-step binary mask alignment.

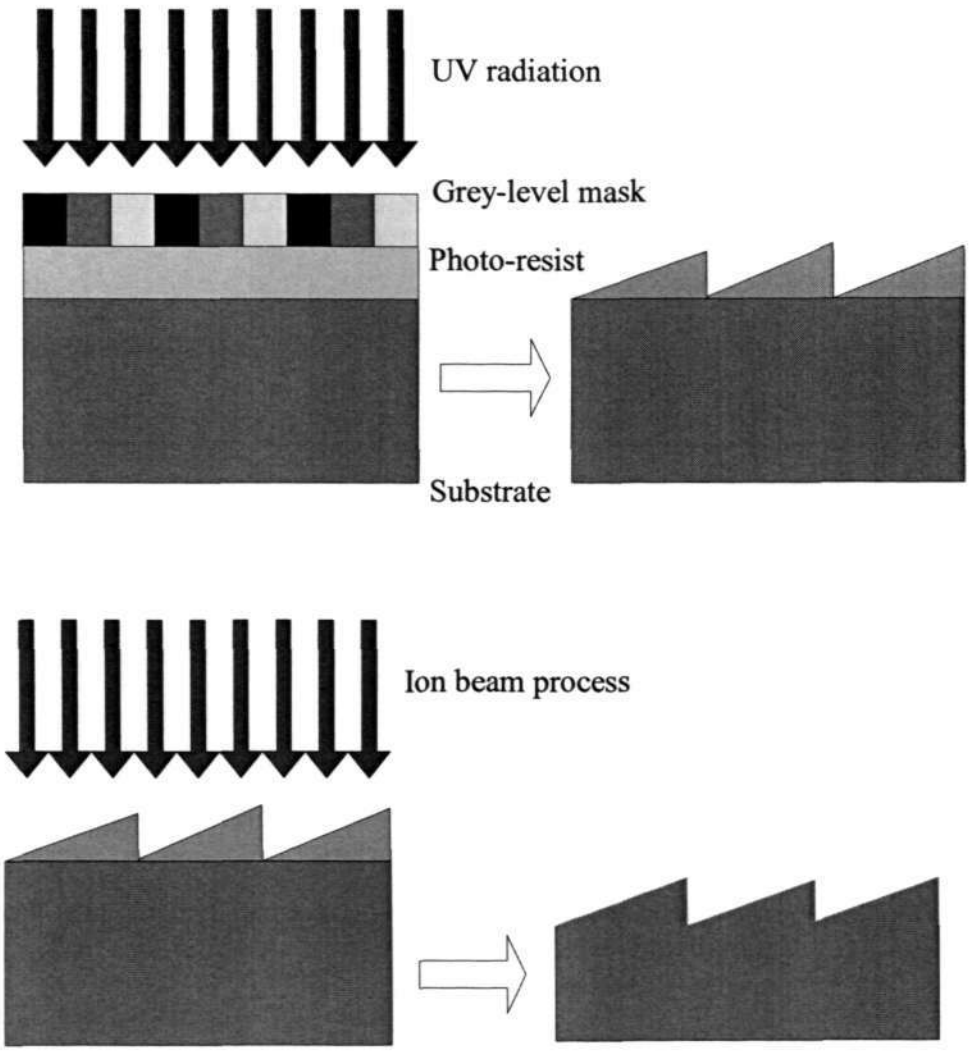

Figure 1-3: Fabrication of multi-level structures by grey scale mask.

From the above three figures, it can be seen that the last dry etching process is essential in the three methods so that the multi-level structure can be transferred into the substrate as a permanent element. Usually, the dry etching process is expensive and time consuming. Therefore, these make the cost of fabrication of microoptical elements extremely high and the production period very long. A very important question comes to our mind: "How can we lower the cost and shorten the process period of fabricating microoptical elements?" Hybrid photosensitive sol-gel material is a possible solution. This is because the fabrication of microoptical elements in hybrid photosensitive sol-gel material has two main advantages. They

are that this material is very cheap and the fabrication process involves only a single step as the usual dry etching process is eliminated. Figure 1-4 and Figure 1-5 present the fabrication process of multi-level structure in hybrid sol-gel material by using a grey scale mask and varying the laser or electron beam dosage in the lithographic method.

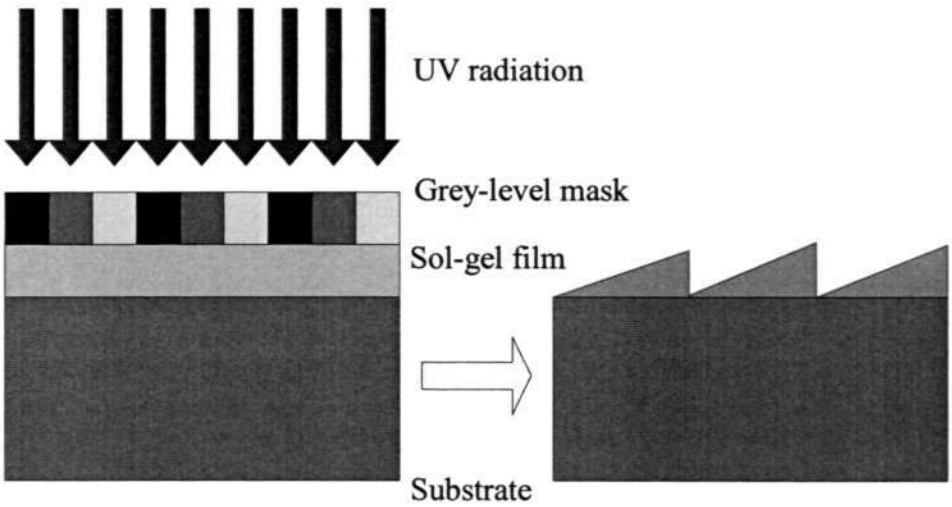

Figure 1-4: Single-step fabrication of multi-level structures by using grey scale mask in sol-gel film.

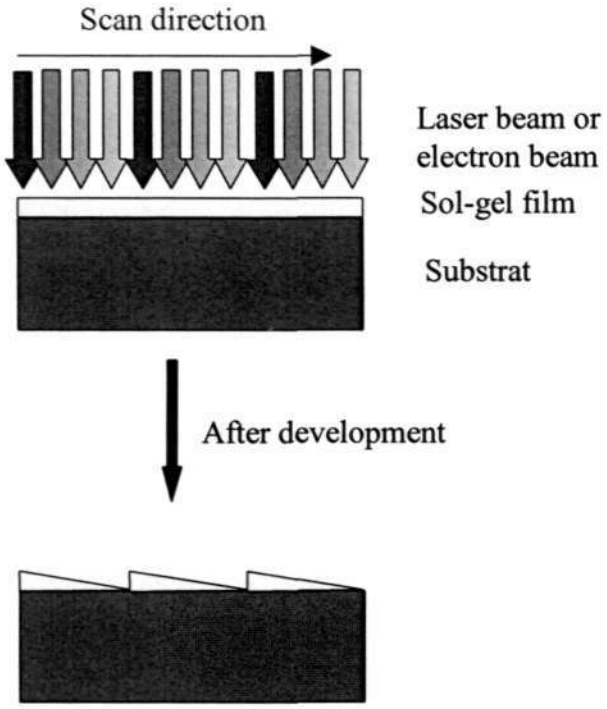

Figure 1-5: Fabrication of multi-level structure by varying dosage of laser beam or electron beam lithography.

It can be seen from the above figures that the application of the photosensitive hybrid sol-gel glass has eliminated the dry etching process in the conventional methods. Therefore, the fabrication process is simplified and accelerated significantly.

Based on the above reasons, the motivation of this thesis is focused on the development of a hybrid sol-gel glass and the application of this material in the fabrication of microoptical elements for photonics applications. Thereby, the cost can be reduced and the speed of the fabrication of microoptical elements can be accelerated.

1.2 Objective of the thesis

The objective of this thesis is to develop a photosensitive hybrid sol-gel glass and apply it in the fabrication of cost-effective microoptical elements for photonics applications. The main photonics application concerned in this work is the coupling of single mode fibre to single mode fibre by using a refractive microlens. The prime objectives are listed as follows,

1. To develop a new recipe of a photosensitive hybrid sol-gel glass with good optical properties.
2. To characterize the new photosensitive hybrid sol-gel glass through various techniques including contact imprinting with a grey scale mask, laser direct writing technique and electron beam lithography.
3. To develop a technique for the mass fabrication of microoptical elements using the photosensitive sol-gel glass.
4. To design a high-efficiency microlens coupler for single mode fibre to single mode fibre coupling by using the Code.V optical design software.
5. To fabricate the microlens according to the desired design and test its coupling efficiency in an optical coupling experiment.

1.3 Major contributions of the thesis

The major contributions of this thesis are summarized as follows:

1. The main novelty of this thesis is to develop a method for fabrication of microoptical elements with continuous surface relief structure in hybrid sol-gel glass. This method simplifies and cuts down the cost of the traditional method that employs an expensive and tedious microlithography plus a follow-on etching process.

2. A new recipe of the photosensitive hybrid sol-gel glass that possesses great optical properties has been developed. This hybrid material has a transmittance >90% in the whole visible waveband and the near infrared waveband. The film thickness can be >2μm after hard baking. Various fabrication methods including gray scale mask, laser direct writer, holographic interference lithography and electron beam lithography method were used to calibrate this kind of hybrid sol-gel material. After calibration, microoptical elements with continuous surface relief structure including saw tooth gratings, sinusoidal gratings, microlenses were fabricated.

   Fabrication of microoptical elements in this kind of sol-gel material makes the process simpler and the etching process used in traditional fabrication method has been eliminated.

3. A new recipe of a self-development photosensitive hybrid sol-gel glass has been developed. Microoptical elements with continuous surface relief structure can be formed in this material after optical lithography and without development process needed. Gray scale mask and laser direct writing were used to characterize this material. After characterization, microlens and saw tooth gratings were fabricated.

   By using this kind of sol-gel material for fabrication of microoptical elements, not only the etching process but also the development process have been eliminated so that the fabrication process is even simpler.

4. A novel mass fabrication method using a polydimethylsiloxane (PDMS) replica in soft-lithography for fabrication of microlenses in sol-gel glass has been developed. By using this method, Microlens with a high numerical aperture of 0.5 and thickness larger than 30μm in sol-gel glass can be

obtained. This method opens a new route for fabrication of microoptical elements with continuous surface relief structure in hybrid sol-gel glass. This new method also shows a very good resolution (10nm) and has a potential to be used for fabrication of nanooptical elements in sol-gel glass. This fabrication method has greatly extended the capability of previous two fabrication methods so that microoptical elements with a thickness larger than 30μm can be fabricated in sol-gel glass.

5. A high efficiency microlens coupler has been designed for fibre-to-fibre coupling. Microlens with a numerical aperture of 0.3 was fabricated in sol-gel glass by soft-lithography method.
6. The coupling efficiency of the fibre-microlens-fibre system was measured in an optical testing experiment.

1.4 Organization of the thesis

The whole thesis is organized into seven chapters.

In Chapter 1, a brief introduction of this thesis is given, including the motivations, the objectives and the main contributions.

In Chapter 2, an overview of the development of the photosensitive sol-gel glass and its application in photonics is given. A new recipe of the photosensitive hybrid sol-gel glass is developed and its general optical properties are characterized.

In Chapter 3, a development-based fabrication of microoptical elements in photosensitive hybrid sol-gel glass by using a variety of facilities is investigated. In this fabrication process, a development process to reveal the surface relief

structures is performed after exposing the photosensitive sol-gel film to UV light. With this method, gratings and microlenses were fabricated.

In Chapter 4, a novel self-development photosensitive hybrid sol-gel glass is characterized using a laser direct writer and a high energy beam sensitive grey scale mask. With these methods, preliminary blazed gratings and refractive microlens were fabricated.

In Chapter 5, a simple method for mass replicating microoptical elements in photosensitive hybrid sol-gel glass was developed. By using this method, thick microlens array were replicated.

In Chapter 6, the sol-gel microlens array fabricated by the soft-lithography method was characterized, in which the focal length, point spread function and modulation transfer function were measured.

In Chapter 7, an introduction of the Code.V optical design software is firstly reviewed and then a high efficiency microlens coupler is designed and applied to the fibre-to-fibre coupling.

Finally, in Chapter 8, a summary of the thesis is given and the recommendations for future work are discussed.

Chapter 2. Photosensitive sol-gel material synthesis and its photochemical mechanism and polymerization kinetics

In this chapter, we first give a brief review of photosensitive sol-gel material and its application in photonics, and then introduce a new recipe of photosensitive sol-gel material developed in the project. The photochemical mechanism and polymerization kinetics of the sol-gel material were also investigated.

2.1 An overview of photosensitive hybrid sol-gel glass and its applications in photonics

Although sol-gel optics has been developed for several decades, the development of the UV photosensitive hybrid sol-gel glass was only initiated about 10 years ago. From the open literatures, there are mainly three research groups developing this material for photonics applications. They are the Photonics Research Group of Montreal's Ecole Polytechnique, P.Q., Canada, VTT Electronics in Finland and the Photonics research group of Nanyang Technological University, Singapore.

For the Photonics Research Group of Montreal's Ecole Polytechnique, researchers, S.I.Najafi et al., have developed a SiO_2/ZrO_2 hybrid sol-gel glass since 1995, where they described a simple low temperature method for fabricating a low-loss single-mode integrated optical directional coupler in a photosensitive, hybrid, organically modified sol-gel silica glass [4]. The directional coupler was made in a 5μm thick film, obtained by dip coating. The refractive index of their material is 1.518. Using this method, an UV-light imprinted Bragg grating in sol-gel ridge glass waveguide with almost 100% reflectivity was fabricated by them. The grating with 97% and 95% reflection for TE and TM polarization respectively was written by the phase

mask technique in a single mode ridge waveguide for 1.55μm [5]. In 1998, S.Iraj Najafi gave a detailed description about the work of fabricating sol-gel glass waveguide and grating on silicon [6]. In that work, they optimized the fabrication parameters and obtained smooth side walls ridge waveguide, after which a refractive index modulation grating was made by inscription into ridge waveguides through a phase mask with 193nm (ArF excimer) radiation. At the same time, a new sol-gel route for fabricating ridge waveguide was introduced in reference [7]. In that work, a 4μm ZrO_2/SiO_2 photosensitive thin films was first dip coated in one step, and then the channel waveguides and power splitters were imprinted by UV light through the masks. The method shown in reference [7] is simple and reproducible and the fabricated waveguide has a low loss of 0.13dB/cm.

As for the researchers of VTT Electronics, they began their development of the relative sol-gel work from 1999. They had investigated and fabricated photonics components using sol-gel by several methods including the holographic interference technique, phase mask and electron beam lithography. In 1999, M.A.Fardad and M.Fallahi fabricated a multi-mode interference power splitter by using a mask and a mask aligner [8]. A 1×32 multi-mode interference power splitter for 1.55μm wavelength transmission was UV-imprinted in aluminosilicate material coated on SiO_2. At the same time, P.Ayras et al. fabricated diffraction gratings in sol–gel films by direct contact printing using an UV-mercury lamp [9]. The material used for the diffraction gratings is SiO_2/ZrO_2 hybrid sol-gel glass. Gratings with 1-μm period were fabricated in sol–gel films. In another work, P.Ayras et al. managed to fabricate multilevel structures in sol-gel thin films with a single step process [10]. They had used a grey scale mask to characterize the sol-gel film thickness after exposure and a maximum height of 1.5μm was obtained. Within

the same group, J.T.Rantala et al. had fabricated several diffraction gratings by using electron beam lithography in hybrid sol-gel glass [11]. In their experiment, electron beam dosages from 10 to 100 $\mu C/cm^2$ were able to crosslink the material and convert it into hybrid sol-gel glass. The sensitivity and the contrast of the material were found to be good as a line width of 0.5μm was obtained. From 2000, J.T. Rantala et al. began to fabricate micro-opto-mechanical structure in thick hybrid sol-gel films [12]. In their work, high quality thick films were obtained by a one-step spin-coating process and high grade structures could be fabrication by direct UV imprinting. A film thickness of 27.5μm and a maximum patterned thickness of 17.4μm with an aspect ratio of 0.6 had been achieved. The material has a maximum transmission of 97% between 400 and 1100nm, a refractive index of 1.49 and a RMS surface roughness of 14.8nm after development. The main purpose of that work was that they wanted to synthesis a hybrid sol-gel material that can be patterned with opto-mechanical and optical structures by UV imprinting simultaneously. Next, they tried to mount these micro-opto-mechnical structures onto the micro-optical table (MOT) that is lithographically patterned in a bulk-micromachined silicon wafer. In this way, passive and active microoptical systems can be integrated in a silicon wafer with a high accurate alignment of the variable microoptical elements.

In NTU, the photonics research group began to investigate and fabricate diffractive optical elements (DOEs) using hybrid sol-gel material from 1999. Instead of using SiO_2/ZrO_2 hybrid sol-gel glass, a novel SiO_2/TiO_2 hybrid sol-gel glass was developed. In 2000, Hongjin Jiang et al. reported this novel material and demonstrated its application in fabricating a diffraction grating using a single step holographic interference method [13]. In this work, diffraction gratings with periods

from 0.92μm to 4.45μm were fabricated. In another work by them, a diffractive lens was fabricated using the same material [14]. In the same year, X-C Yuan et al. characterized this material by using a high-energy beam sensitive (HEBS) grey scale mask. In addition, they also managed to fabricate one blazed grating with continuous surface relief structure [15].

In conclusion, we have found out that there are a number of researchers putting in effort in this field. Researchers in Canada are focusing their work in the fabrication of ridge waveguides and gratings. As for the researchers in VTT, they are focusing their effort in the fabrication of gratings and thick micro-opto-mechnical structures. They have also calibrated their material using a grey scale mask, though the responsive characteristic is nonlinear. The group of researchers from NTU is focusing their work in the fabrication of diffractive optical elements (DOEs). Similar to the researchers from VTT, the NTU group has also characterized their material using HEBS grey scale mask, although the calibration results show that the present material only exhibits a relatively narrow dynamic range of linear response. To obtain good quality DOEs, a linear response sol-gel glass is required so that the design and fabrication process can become easier.

In this project, a new photosensitive hybrid sol-gel glass based on the material developed by Jiang and Yuan in reference [15] was synthesized and characterized with different methods. This is to overcome a main shortcoming of the material in reference [15], which is the sol-gel film thickness is less than 1μm after hard baking. The new sol-gel material reveals good optical properties and the film thickness can be larger than 30μm, which are enough for the fabrication of any diffractive optical elements and many other refractive optical elements.

2.2 Synthesis of photosensitive sol-gel glass and its general optical properties

The hybrid sol-gel glass, which is shown schematically in Fig.2-1, is synthesized by two solutions. Solution I is a silicon oxide network, formed by the hydrolysis of prolylmethacrylate-substituted trimethoxysilane, 3-(trimethoxysilyl) propyl methacrylate (MAPTMS), in isopropanol and acidified water. In this case, the molar ratio is 0.04:0.048:0.035. Solution II is a titanium oxide network, formed by adding titanium propoxide ($Ti(OC_3H_7)_4$) into acetylacetone at a molar ratio of 0.01:0.04 in nitrogen environment and was agitated until homogenization was reached. The two solutions were then mixed up with a molar ratio of 4:1 (SiO_2:TiO_2). It should be mentioned that titanium was used to modify the refractive index of the silicon oxide network. The final mixture solution was allowed to age at room temperature for 30 hours with vigorous stirring. During the aging, the MAPTMS is hydrolyzed with water and followed with the condensation to form the silicate backbone. Figure 2.2 shows the silicate backbone formed during hydrolysis and condensation of MAPTMS. This negative-tone silicon titanium material was made UV photosensitive possible by adding a photoinitiator IRGACURE 184 (CIBA) with 4% wt to the sol-gel. Before being spun onto the pre-cleaned fused silica substrate, large particles in the mixed solution were removed by a 0.1 μm membrane filter attached to a syringe. A thin film layer of the sol-gel was spun onto a glass substrate at 1200rpm for 60secs and a film with thickness greater than 2.0 μm could be achieved easily.

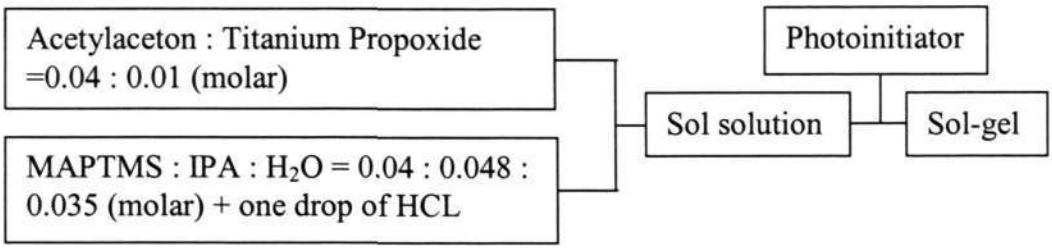

Fig.2-1. Scheme of preparing a new recipe of sol-gel material.

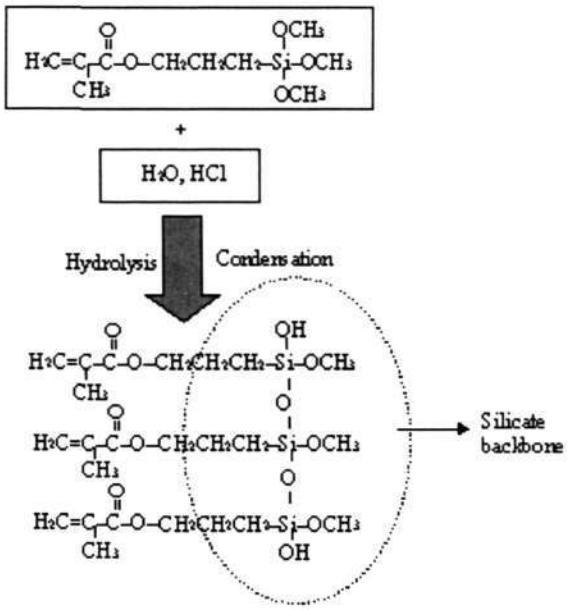

Figure.2.2. Partial elaboration of silicate backbone formed during MAPTMS hydrolysis and condensation.

We measure this material thickness and refractive index by using a prism coupler (Metricon Corporation). The refractive index and thickness of our hybrid sol-gel glass are 1.52 and 2.0 μm, respectively. The figure below shows the refractive index and thickness measurement results for sol-gel film by using prism coupler.

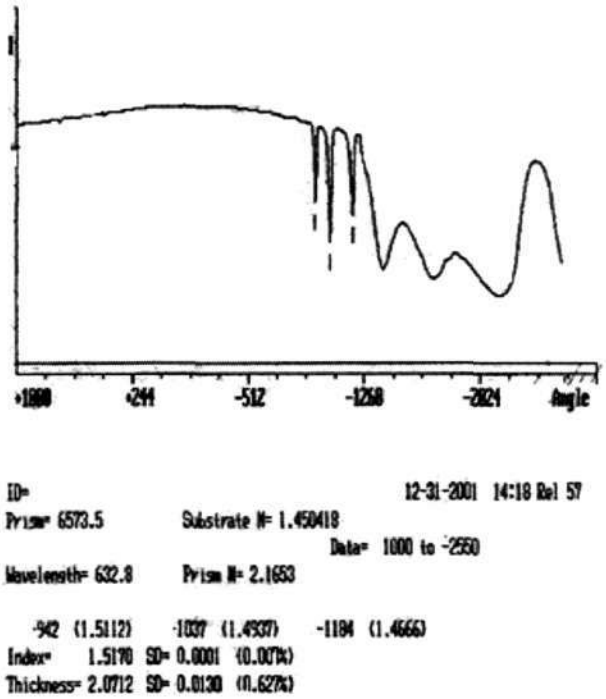

Figure.2-3. Thickness and index measurement results for sol-gel film by prism coupler.

Where, the standard deviation (SD) displayed is simply the standard deviation of the multiple estimates computed about the average. If three or more modes are found, multiple estimates of thickness and index will be generated. Once we have multiple estimates, the measurement result is the average of the multiple estimates, while the percentage following the SD is calculated by dividing the SD by the average. Here the standard deviation of the measured refractive index and thickness were very small, 0.0001 and 0.013 μm respectively

Fig 2-4 shows the graph of film thickness against spinning speed. It can be seen that with this recipe, the maximum film thickness can reach up to 4μm.

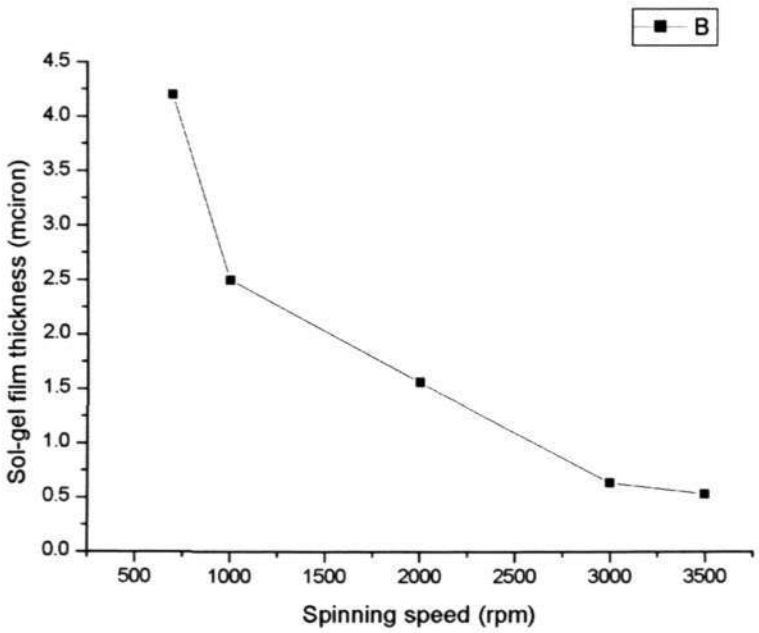

Fig.2-4. Sol-gel film thickness against spinning speed.

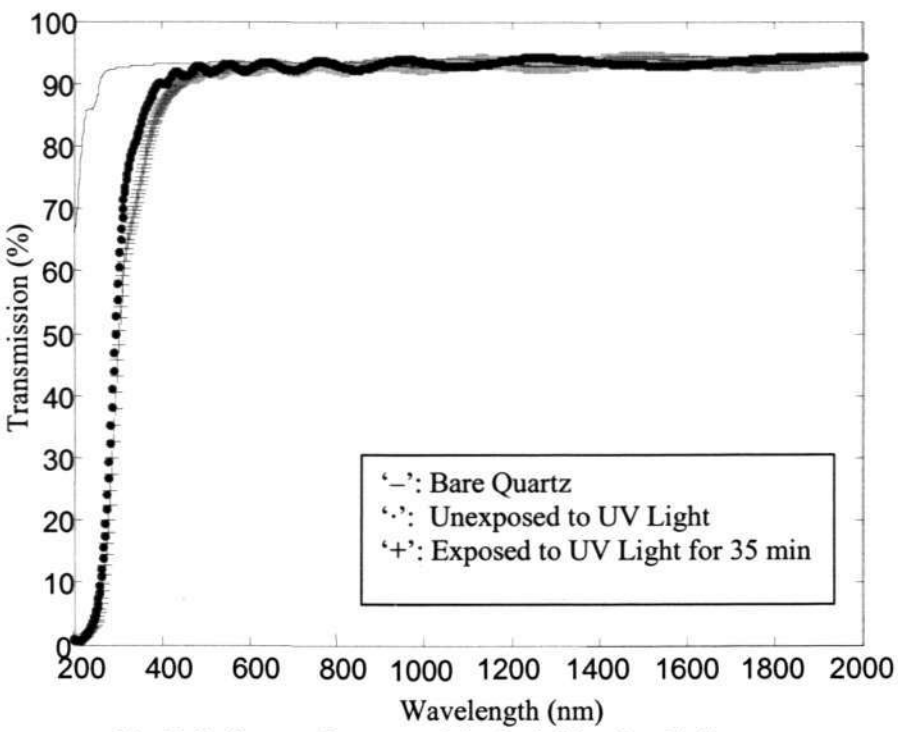

Fig.2-5. Transmittance of the hybrid sol-gel glass.

The transmittance of the sol-gel glass for a wavelength range of 200 – 2000nm measured by a spectrophotometer is presented in Figure 2-5. The straight-line curve, dotted curve, and plus-symbol curve are the transmission spectrum of bare quartz, sol-gel film unexposed to UV light, and sol-gel film exposed to UV light for

35 min respectively. From Fig.2-5, the transmission of the sol-gel film without UV exposure is more than 90% in the wavelength range of 415nm - 2000nm, while for the sol-gel film with UV exposure, the wave band shifts to 454nm - 2000nm. This figure depicts a good optical property for sol-gel glass. Due to its high transmission spectrum from visible band to far infrared band, this material can be used as a good alternative in integrated optics and optical communication system.

The surface roughness is also an important parameter for investigation of the sol-gel film. We characterize its surface roughness by using an atomic force microscope (AFM). Fig.2-6 and Fig.2-7 show the three-dimensional surface profile of sol-gel film without UV exposure and with UV exposure for 35 min respectively. The figures show that the values of the root mean square of the two film samples are 0.741 nm and 1.593 nm respectively, which are considered as small values for optical surfaces. Comparing these two figures, we realized that the surface roughness was increased after exposure.

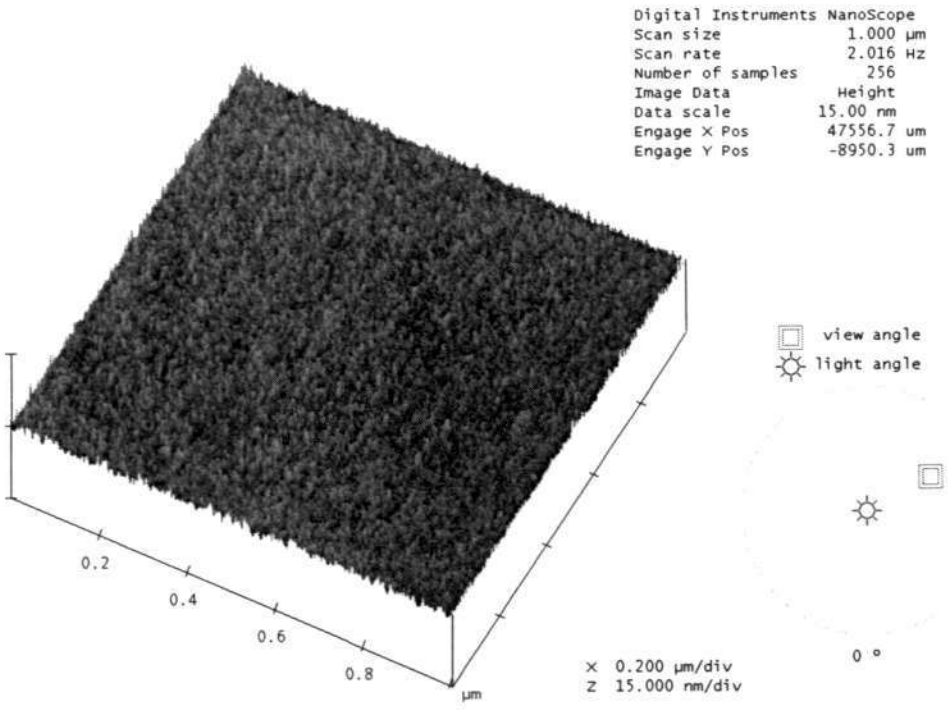

Fig.2-6. The surface roughness of sol-gel film before exposure to UV light.

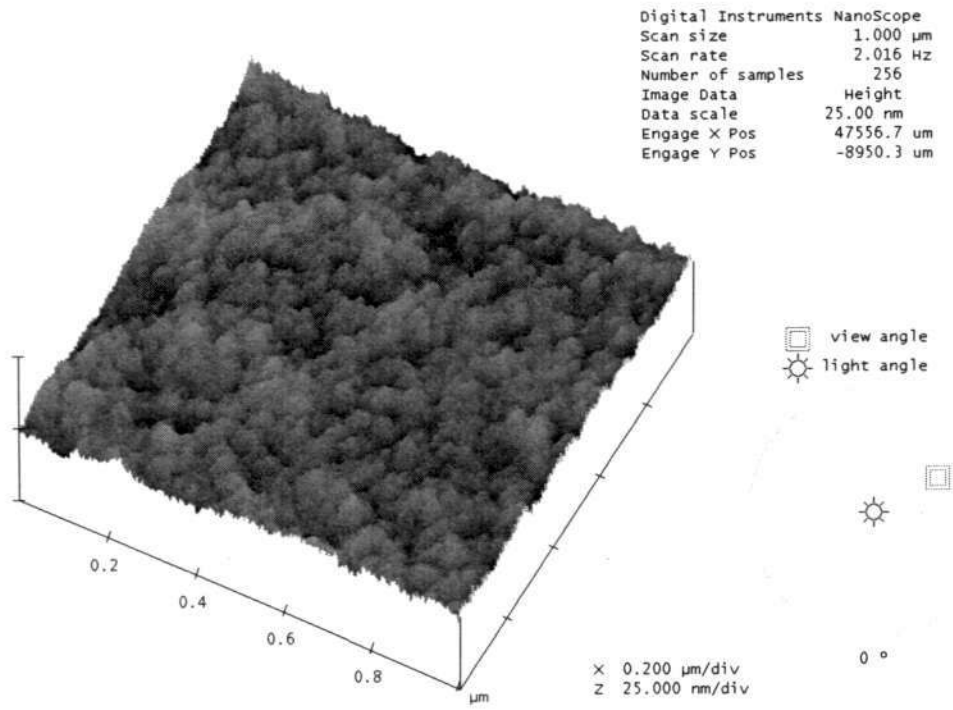

Fig.2-7. The surface roughness of sol-gel film after exposure to UV light.

Another important property of sol-gel glass is its glass transition temperature. If this material has a relatively high glass transition temperature, the corrugated pattern will be stable without changing its shape, which will be more reliable for the microoptical systems built with this sol-gel film. The glass transition temperature of sol-gel material was measured by Differential Scanning Calorimetry technique. The figure 2-8 shows the experiment setup for differential scanning calorimetry,

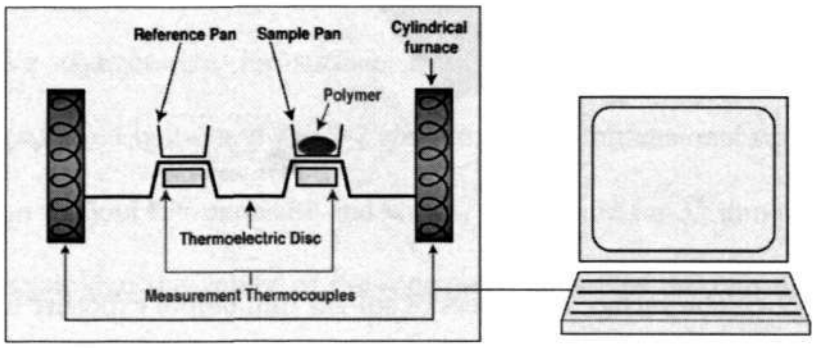

Figure.2-8. Experiment setup for differential scanning calorimetry.

Where, the computer controls the furnace to heat two pans with the same heat rate. For two pans, one is empty and the other is with sol-gel glass. When we start heating two pans, the computer will plot the difference in heat flow against temperature. That is to say, we're plotting the heat absorbed by the sol-gel glass against temperature. This plot reflects the heat capacity against heat flow. The heat capacity is defined as the amount of heat the sol-gel material takes to get a certain temperature increases. We get the heat capacity by dividing the heat supplied by the resulting temperature increase. The glass transition temperature falls in the range of temperature where the heat capacity begins to increase. This is because the heat capacity of sol-gel material increases when temperature is bigger than glass transition temperature.

The final experiments result for measurement of glass transition temperature of sol-gel material is shown in the following figure,

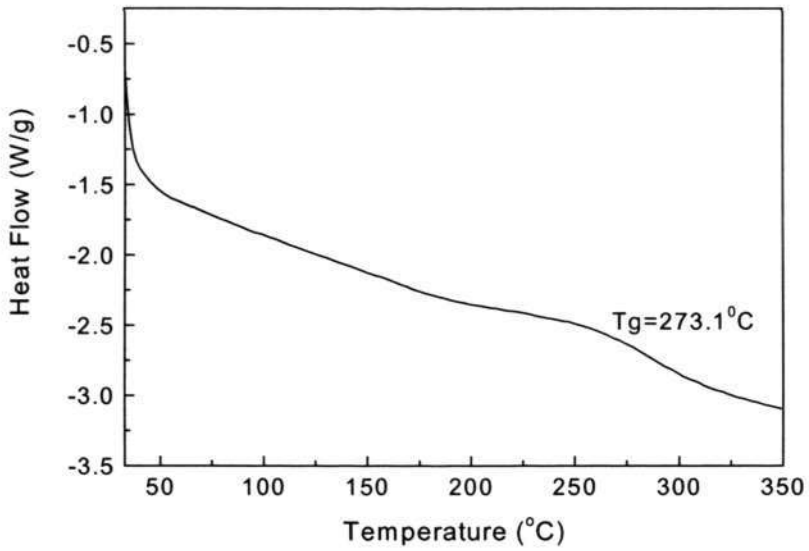

Figure.2-9. The measured heat flow against temperature for sol-gel material.

It can be seen from the figure, the heat capacity change happens in the temperature range that the middle point is 273℃.

This measurement result is reasonable because this hybrid sol-gel material is a kind of amorphous polymer before its crystallization. Some researchers also obtained a glass transition temperature of 290℃ for their sol-gel material by this method [16].

Moreover, we irradiated the sol-gel samples patterned with some structures such as gratings with a high power laser from 40W to 100W for several minutes, and we found that the structures in sol-gel glass did not change under the high power laser radiation. This shows that the optical elements made in hybrid TiO_2/SiO_2 sol-gel glass have a great resistance to a high power laser source and it implies that this material can be also useful in applications with high power laser sources.

2.3 Photochemical mechanism and polymerization kinetics of hybrid material when exposed to UV light

Photosensitive hybrid sol-gel material contains organic and inorganic components. Usually, inorganic silica glasses are used for the fabrication of optical components due to their good optical and mechanical properties. If one wants to produce a microstructure in inorganic silica glasses, conventional multi-step fabrication method will be involved. There are some milling methods available as single step fabrication solution in practice, for example the focused ion beam and the precision diamond cutting methods. However, as these two machines are very expensive and the fabrication processes are time consuming, they are not suitable for mass fabrication.

By introducing organic components into inorganic silica network through sol-gel synthesis process, one can obtain a more flexible method to fabricate microoptical elements. When photoinitiator is added into the sol solution, as the hybrid material is sensitive to UV light, it is possible to pattern the structures in the film directly through lithographic methods. More importantly, after lithography and hard bake, the film will be condensed into hybrid organic-inorganic glass and no further pattern transfer needed.

Photoinitiator is a key component in the single-step sol-gel fabrication method. It is photodecomposed into radicals to initiate the polymerization of organic components in hybrid material, and this makes the exposed regions of hybrid film unresolvable to organic solvents such as ethanol, acetone and isopropanol. After lithography and soaking in the organic solvent, the desired pattern is revealed. With a further

hardbaking process, the patterned film can be condensed into an organic and inorganic glass with patterned structures.

2.3.1 Photochemical reaction mechanism

In this section, a detailed investigation of the photochemical mechanism of photoinduced polymerization is presented.

The photoinduced polymerization components in our recipe are MAPTMS and photoinitiator. These two chemical structure images are as follows,

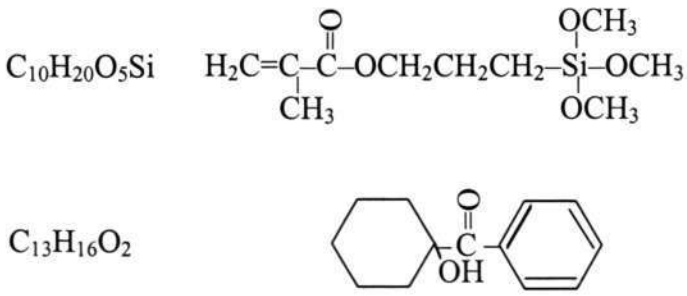

Fig.2-10. Chemical strucutres of MAPTMS (top) and Photoinitiator (bottom).

These two chemicals are both soluble in ethanol solution. The reason why we chose to use 1-hydroxycyclohexyl phenyl kethone ($C_{13}H_{16}O_2$) as photoinitiator is because of its low absorbance in 365nm, which is usually the peak emission wavelength of the mask aligner. Since the absorbance of the UV light by photoinitiator is very small, the penetration thickness of the hybrid sol-gel film by UV light will be larger. Fig.2-11 shows the absorbance spectrum of this photoinitiator in UV waveband (www.sigmaaldrich.com). It is clearly seen that the absorbance of this photoinitiator in 365nm is less than 0.1%.

When photoinitiator is irradiated by UV light, it can be decomposed into two radicals. These two radicals can initiate polymerization by either reacting with

polymerizable methacryl groups or making a new molecule by the coupling of two benzoyl radicals. This process is shown in the Fig 2.12.

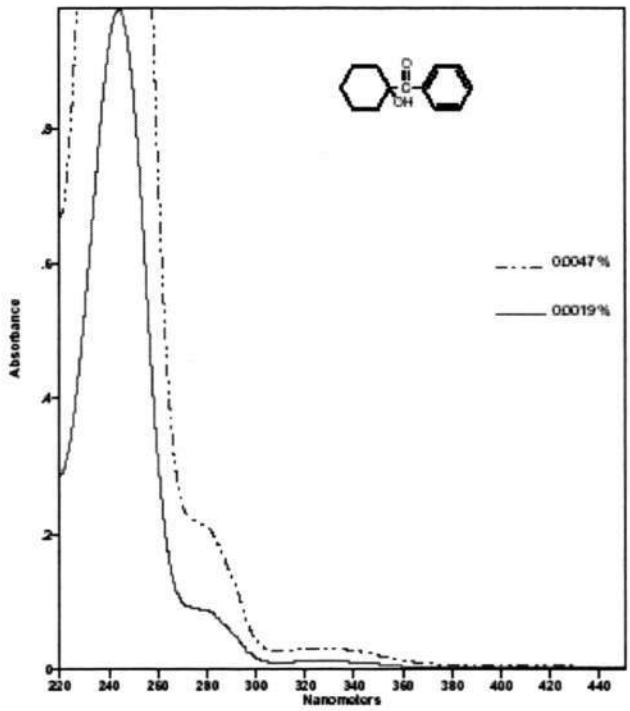

Fig.2-11. The absorbance spectrum of photoinitiator in UV waveband (www.sigmaaldrich.com).

Photodecomposition

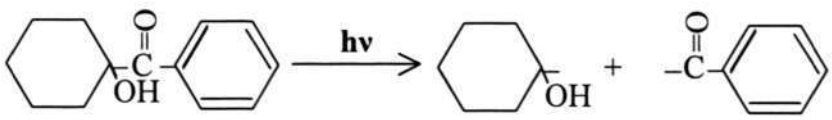

Coupling of benzoyl radicals

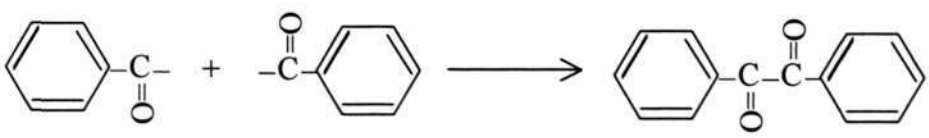

Polymerization initiation

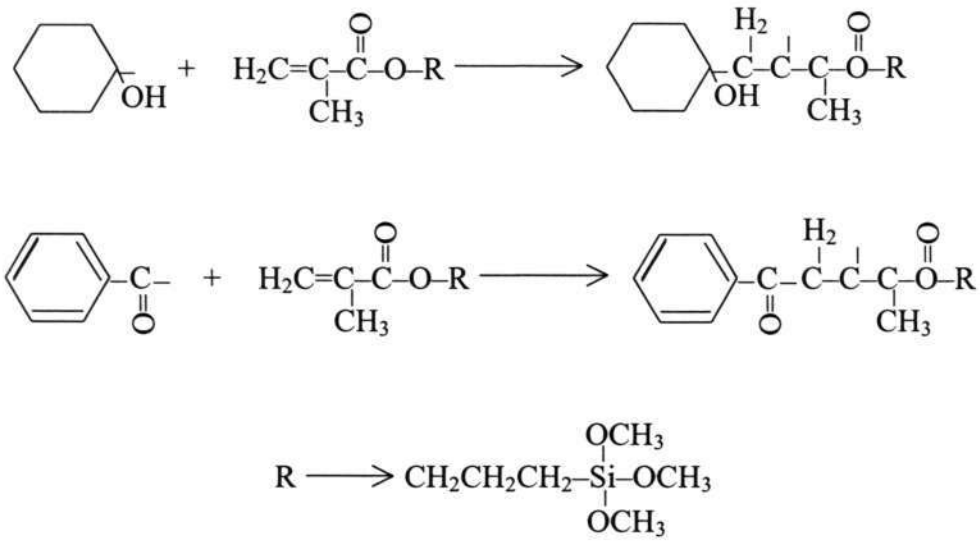

Fig.2-12. Schematic diagram of photochemical reactions when sol-gel film is exposed to UV light.

2.3.2. Polymerization kinetics

When photosensitive hybrid sol-gel film is exposed to UV light, photoinitiator is decomposed into radicals and the polymerization is initiated by the consumption of C=C bond in methacryl group of MAPTMS. At the beginning of UV radiation, the rate of forming radicals is much slower than the consumption of radicals when they combine with the C=C bonds to initiate polymerization of methacryl group in the MAPTMS. Next, the combination of radicals with C=C bonds slows down since the monomer components need to propagate. As a result, the consumption rate of radicals is slowed down as well. After a short time, the formation and consumption rates of radicals will reach the same rate, which means that the chemical reaction has reached a steady state. The polymerization kinetics at steady state for most free radicals initiated polymerization can be formulated as follows [17]:

$$-\frac{dM}{dt} = k_p M \sqrt{\frac{f k_d I}{k_t}}$$

where M is the total concentration of all radical chains, I is the concentration of photoinitiator, and f is the fraction of initiator radicals that actually starts polymerization of methacryl group of MAPTMS. K_p, K_t, and K_d represent the rate constants for propagation, termination, and dissociation of initiator respectively. Here, I, K_t, K_d and f are independent of M. The polymerization progress can be expressed by the consumption of C=C bonds in the methacryl group, while the C=C bond stretching mode band area reflects the concentration of C=C bonds in the methacryl group. Therefore, the C=C bond stretching mode band area is proportional to the methacryl monomer concentration and the reduction of the band area represents the polymerization degree. The following figure shows the FTIR spectra of methacryl groups in the hybrid films with different UV illumination time. The photochemical reaction was monitored by using a Fourier transform infrared (FTIR) spectrometer. The FTIR spectra of hybrid materials was also reported elsewhere [18-20]. Figure 2-13 shows the FTIR spectra of the sol-gel films for different UV exposure time from 0 to 40 min. It should be noted that a 5-min prebake at 85°C was implemented on a hotplate before exposure to remove the excessive solvent after spin coating. However, there was no postbake after the UV exposure. In the FTIR spectra, the bands at 1719 and 1638 cm^{-1} in Figure 2-13 represent the carbonyl group C=O stretching mode and the vinyl group C=C stretching mode respectively. As seen in Figure 2-9, the C=C stretching mode becomes weak when UV exposure time was increased and the C=C stretching mode disappears when the exposure time was further increased to 40 min. This indicates that the polymerization of the sol-gel film proceeds with the increase of the UV exposure time. As for the C=O stretching mode, its peak shifts from 1719 to 1726

cm^{-1} with the increase of UV exposure time, demonstrating that the carboxyl group does not conjugate with the carbon double bond. Concurrently, condensation also happens during the polymerization, which is indicated by the diminishing of a series of bands at 1169 cm^{-1} (-CH3 rock), 936 cm^{-1} (Si-OH) and 816 cm^{-1} (Si-O-C) while the Si-O-Si band at 1039 cm^{-1} becomes clear and pure. The band at 915 cm^{-1} should be assigned to Si-O-Ti bonds.

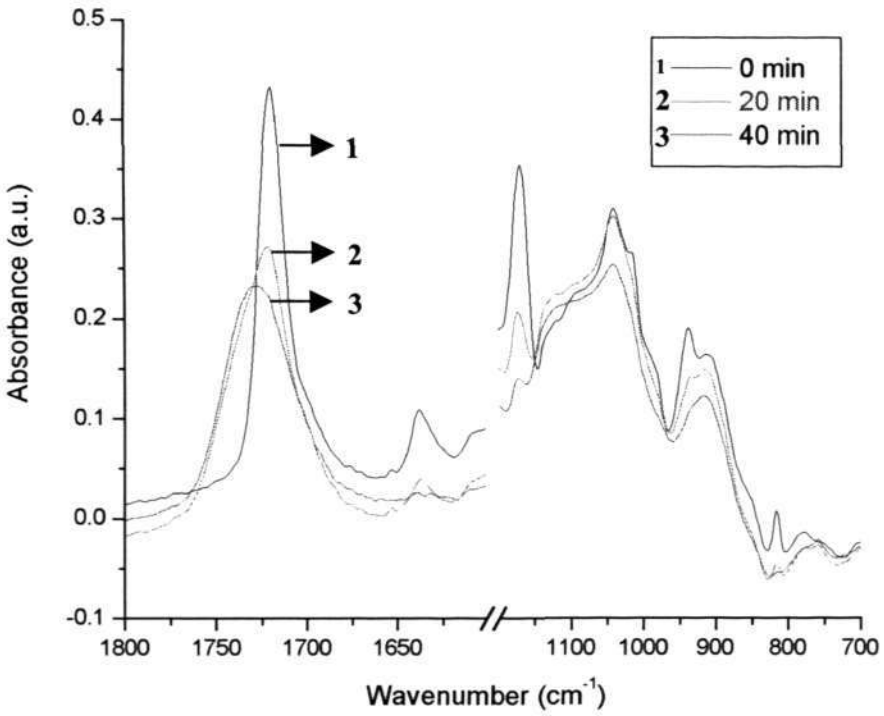

Figure 2-13. FT-IR absorption spectra of the hybrid films with different UV exposure time.

Figure 2-14 shows the transmittance of the hybrid film under different exposure time. The transmittance was measured by a spectrophotometer in a wavelength range from 200nm to 1000nm. Here, the hybrid film was coated on a pre-cleaned microscope glass slide. It is seen from Figure 2-14 that the transmittance became large as the exposure time was increased. When the exposure time was increased to

40 min, there was a significant increase in the transmittance and the absorption edge drops to 349nm. As for the case of 20 min and 0 min of UV exposure, the absorption edges are 431nm and 442nm respectively, which show that the increase in transmittance is small. We attribute the increase in transmittance to the polymerization and condensation of hybrid films induced by the UV irradiation.

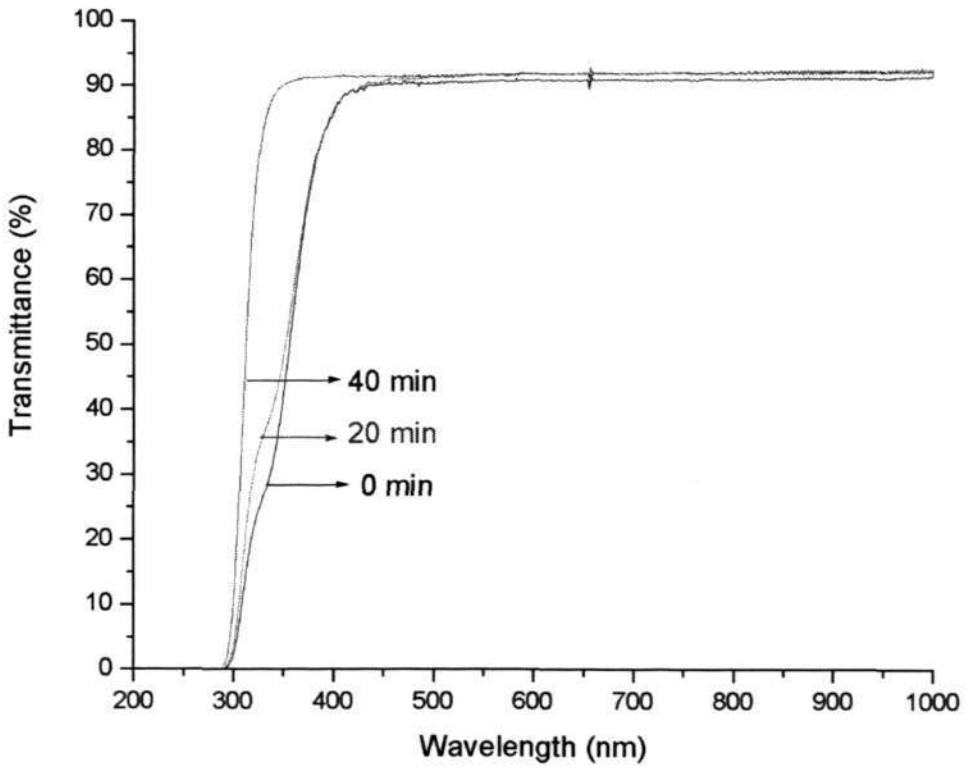

Figure 2-14. Transmittance of the hybrid material.

2.4 Conclusions

In this chapter, we introduced a novel recipe of TiO_2/SiO_2 photosensitive hybrid sol-gel material. This material has good optical properties and the transmittance is over 95% in the whole visible and near infrared wave band. The glass transition temperature was measured as 273.1°C, which means that the microoptical elements possess a great resistance to high temperature environment. In addition, several

high power laser sources with powers of 40W to 100W were used to irradiate the microoptical elements in the hybrid sol-gel glass and the results obtained showed that there is no change in the shape of microoptical elements fabricated in sol-gel glass.

Finally, the photochemical mechanism and polymerization kinetics of this sol-gel material was investigated. An UV-Visible spectrometer and a FTIR spectrometer were used to monitor the transmittance and the chemical bonds changes as a function of different UV irradiation on the hybrid sol-gel material.

Chapter 3. Fabrication of microoptical elements in development based photosensitive hybrid sol-gel glass

In this chapter, we investigate the fabrication of microoptical elements in a development based photosensitive hybrid sol-gel glass. Development based hybrid sol-gel materials, like conventional photoresist, will reveal its imprinted structures formed by UV exposure only after a development process. As our hybrid sol-gel material is a negative tone resist, those areas exposed to UV light remain after development in ethanol solution, while those unexposed areas are washed away. To obtain a microoptical element with an arbitrary surface relief structure, one must be able to control the sol-gel film thickness that remained after exposure and development. Therefore, a calibration process involving the investigation of the relationship between exposure dosage and remained film thickness is needed. In this chapter, we will calibrate hybrid sol-gel film by several lithographic methods including laser direct writing technique, electron beam lithograph technique and negative grey scale high-energy beam sensitive (HEBS) glass mask. The calibration work is to define a relation between UV light or electron beam intensity and sol-gel film thickness after the development and post baked processes. The thickness of the sol-gel film is measured by a Dektak Surface Profiler (Veeco Metrology). Based on the calibration results, microoptical elements with desired height can be formed in the hybrid sol-gel glass.

3.1 Synthesis of development-based photosensitive sol-gel glass

Synthesis of the development based photosensitive hybrid sol-gel glass is shown in Figure 2-1. In the following sections of this chapter, different fabrication facilities were used for the fabrication of microoptical elements in this photosensitive hybrid

sol-gel glass. The common step of these fabrication methods is that a development process is always needed to reveal the designed surface relief structure after exposure.

3.2 Fabrication of microlens array and blazed gratings in the development based photosensitive hybrid sol-gel glass by using high-energy beam sensitive grey scale mask

There exists various lithographic techniques for the fabrication of micro-optical components, for example, direct writing techniques (UV laser and electron beam), photolithographic mask projection and contact printing techniques are widely used for manufacturing micro-optical diffractive/refractive elements. Generally, the photoresist-based fabrication involves two steps. Firstly, the microstructures on the photoresist are patterned following exposure and development processes. Secondly, the structure is transferred into the substrate by etching. It is known that the sol-gel material has an advantage over the conventional photoresist based fabrication techniques due to its single step process without etching. For 3D surface relief refractive and diffractive microlenses, a high-energy beam sensitive (HEBS) grey scale mask is utilized in the process to provide a reliable and simple method in a single UV exposure. The technique using the sol-gel material with a HEBS grey scale mask has considerable potential for the low-cost mass production of high quality silica-based micro-optical components. Considering the requirements of low cost and mass production in industries, we explored the sol-gel material characterization with the HEBS mask for microlens fabrication in a single step UV exposure. As a result, the surface profile depths on the sol-gel were measured as a function of a range of optical densities (OD) and the characterization results helped

us understand the fabrication of a microlens on the sol-gel using the HEBS grey scale mask.

3.2.1 Fabrication of microlens array

In this section, we show some results of fabrication of microlens array in the development based hybrid sol-gel glass by employing a grey scale mask. The fabrication process is schematically shown in Figure 3-1, where a refractive microlens determined by the mask optical densities translates the surface profile information into the sol-gel thin film. In the fabrication process, a thin sol-gel film is firstly spun coated on a substrate and the photosensitive sol-gel film is then exposed through a HEBS grey scale mask. On the mask, different optical density values will determine different doses that are absorbed in the sol-gel film. As our SiO_2/TiO_2 sol-gel is a negative tone photosensitive material, the areas exposed to the highest dose remained due to cross-linking after development. However, those with the lowest dose were dissolved in the developer.

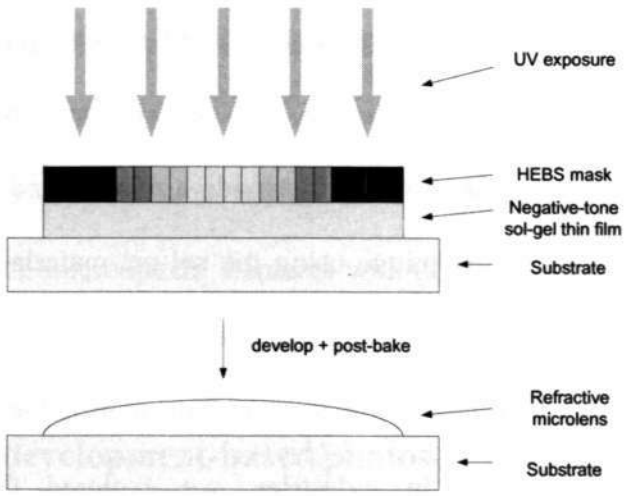

Fig. 3-1. Schematic diagram of microlens fabrication using the HEBS grey scale mask.

To fabricate arbitrarily shaped micro-optical components, it is necessary to characterize the sol-gel material with an HEBS calibration mask, which was specially designed for negative-tone sol-gel material by Canyon Materials, Inc [21]. The calibration helps us build a calibration curve of the remaining height of sol-gel glass after development versus the optical densities in the mask. The calibration plate has 200 grey levels and each grey level consists of one test patch of 100 μm by 100 μm in size. The 200 grey levels are determined by the optical density values ranging from 0.126 to 1.5. Within this range, the grey levels are ascribed optical density values according to the linear equation

$$OD = 0.126 + 0.0069 \times i \qquad (3\text{-}1)$$

where $i = 0,1,2,\cdots,199$. Optical density OD is defined by the following formula,

$$OD = \log\frac{1}{T} \qquad (3\text{-}2)$$

where T is the transmission of the optical light through the gray level in beam sensitive gray scale mask. The UV exposure was implemented on a Q 2001CT UV-mask contact aligner (Quintel Corporation) with a peak emission at 365 nm wavelength and an irradiance of 15 mW/cm^2.

Since the sol-gel is a negative-tone material, the heights of the film thickness remaining are directly determined by the OD values of the HEBS calibration mask. Greater ODs correspond to smaller UV irradiation, which eventually leads to smaller heights of film thickness remaining on the substrate. It is our intention to establish a calibration curve for the sol-gel material over a dynamic range of optical densities. For a given OD value fabricated on the HEBS mask, the sol-gel material will have a corresponding height after development. Figure 3-2 presents a characterization of the sol-gel with the HEBS mask. The depths of the test patch

were measured with a Dektak surface profiler (Veeco Metrology). Based on the experimental observations, it was found that the exposure time is also an important parameter in the fabrication process and different exposure time may result in a different calibration curve. In order to set up a dynamic optical density response, we have found out that the exposure time between 35 min and 37 min provides a stable and good dynamic response for optical density values between 0.12 and 1.2. It is seen in the figure that the sol-gel material exhibits a linear-like response over 156 grey scale levels. This characteristic is convenient for generating any arbitrary surface profile. The sol-gel material also shows little polymerization for OD values beyond 1.2.

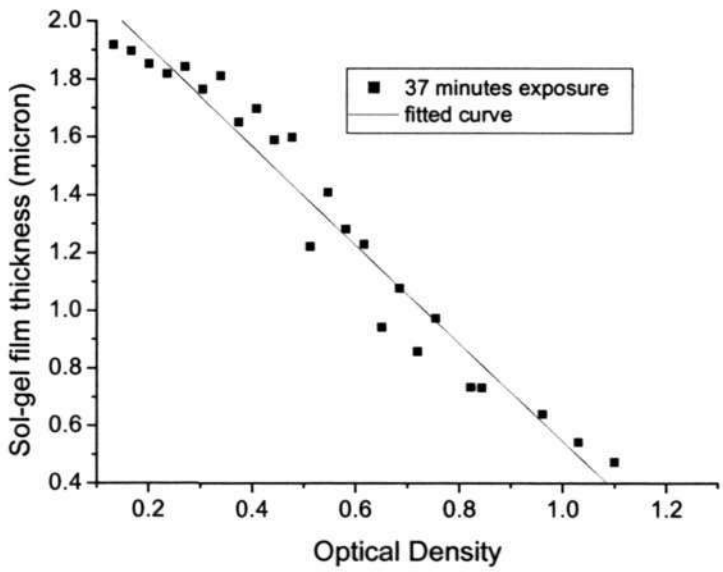

Fig.3-2a. Characterisation of sol-gel film thickness as a function of optical densities of an HEBS mask exposed for 37 minutes

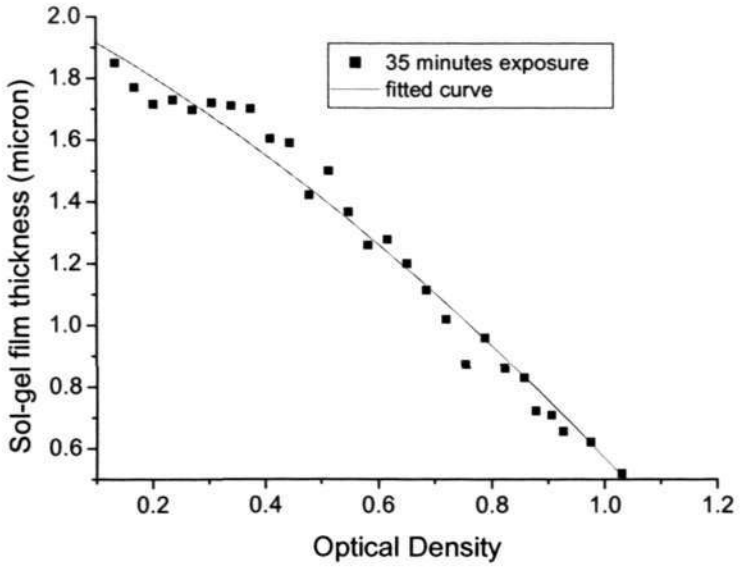

Fig.3-2b. Characterisation of sol-gel film thickness as a function of optical densities of an HEBS mask exposed for 35 minutes

Based on the calibration results, a refractive microlens was fabricated on the sol-gel glass. Figure 3-3 shows the 2D and 3D surface profiles of the microlens measured by a laser interferometer (WYKO NT 2000). The single microlens is a positive lens with a 50 μm diameter. Optical density values on the calibration mask are set between 0.129 and 1.017 in such a way that the OD values are decreased from the centre to the outermost edges of the lens. Therefore, the surface profile can be formed on the sol-gel material following the respective OD values. The microlens, formed under the same fabrication conditions as stated above, has a maximum height of about 1 μm at the lens centre (see Figure 3-3). The HEBS grey scale mask is a calibration mask provided by Canyon Materials Inc. Detailed information about the OD values for generating the refractive lens is not available with the calibration mask. It is our intention here to setup the calibration curve for the sol-gel material so that we can compare the actual profile with the desired one when the OD values are generated for a specific design in future. For a specific microlens design, we

need to generate concentric rings with different calibrated OD values that define the surface profile. Comparing with the techniques using a set of binary masks or halftone grey mask for generating grey scale structures, the surface quality provided by the HEBS method is better because the HEBS has a higher grey scale resolution. It is reported that the OD levels in the range of 0.126 and 1.5 can be produced by electron-beam direct writing to a precision of ± 0.001 [20]. In the fabrication process, the sol-gel thin film was first exposed for 35 min before undergoing the development and post-baking processes.

In addition, a refractive negative microlens array was fabricated on the sol-gel glass. Figure 3-4 and Figure 3-5 show the surface profile of the positive and the negative microlens array measured by a laser interferometer (WYKO NT 2000) respectively. The single lens is a 50 μm diameter positive lens. Since the OD values are set in a way that the OD values are arbitrarily decreased from the centre to the outermost edge of the lens, an arbitrary surface profile is therefore formed on the sol-gel material following the respective OD values after UV exposure.

We characterized the positive microlens array with a beam profiler. Figure 3-6 shows the focal spot of the positive microlens array measured with a beam profiler.

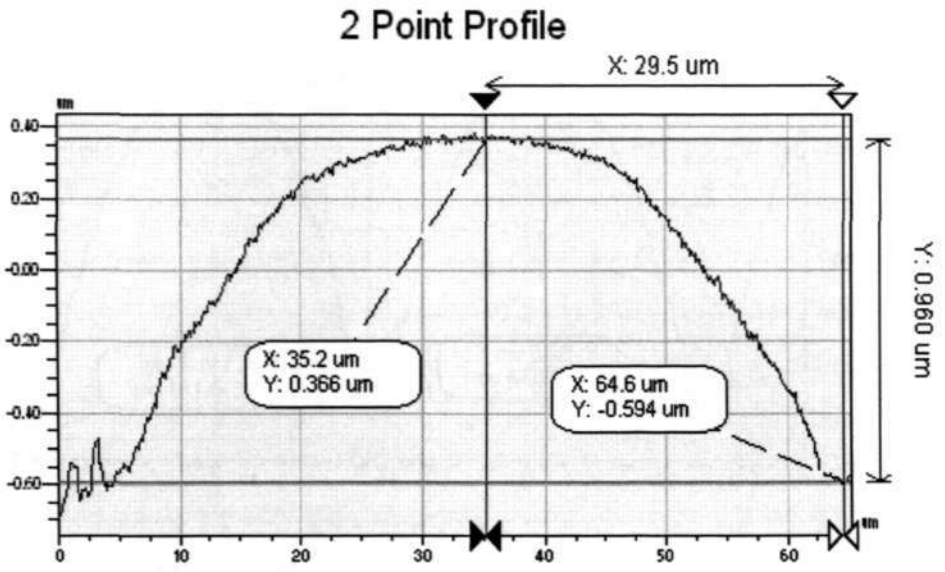

Figure 3-3(a). 2-D profile for a single microlens.

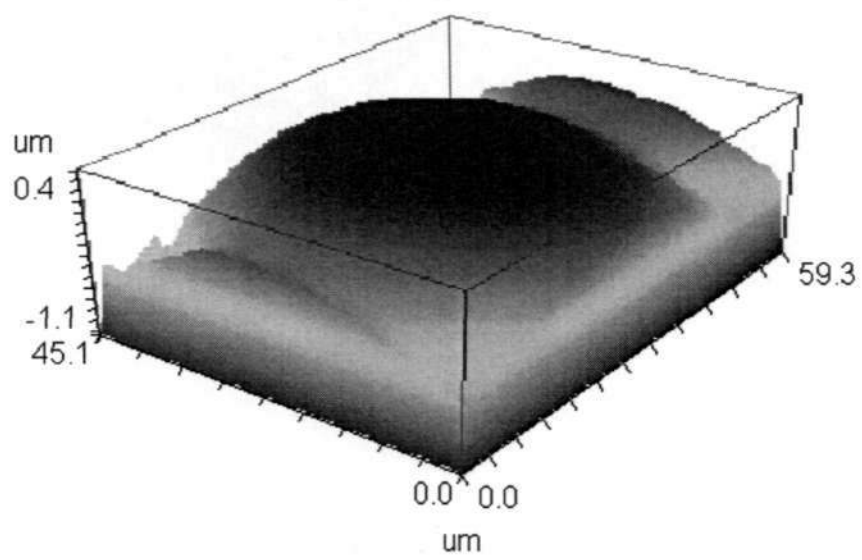

Figure 3-3 (b). 3-D profile for a single microlens.

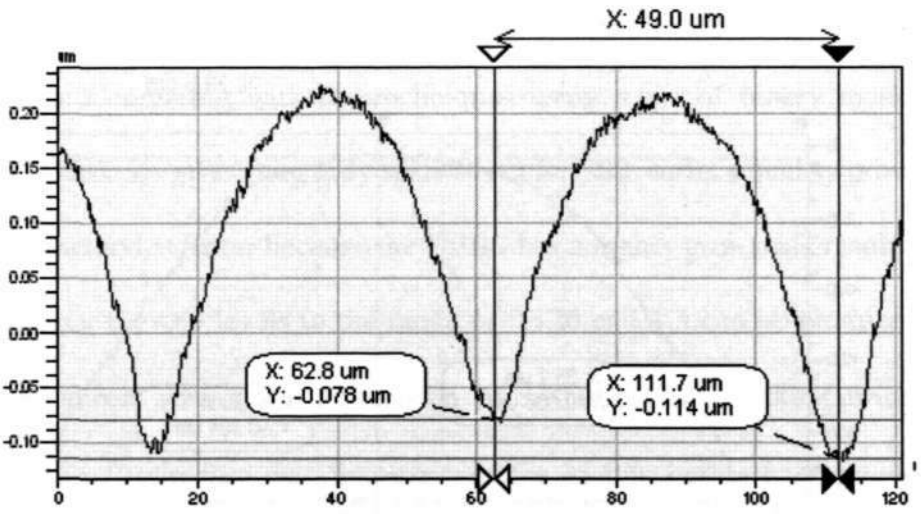

Fig. 3-4a. 2D profile of a 2×2 microlens array.

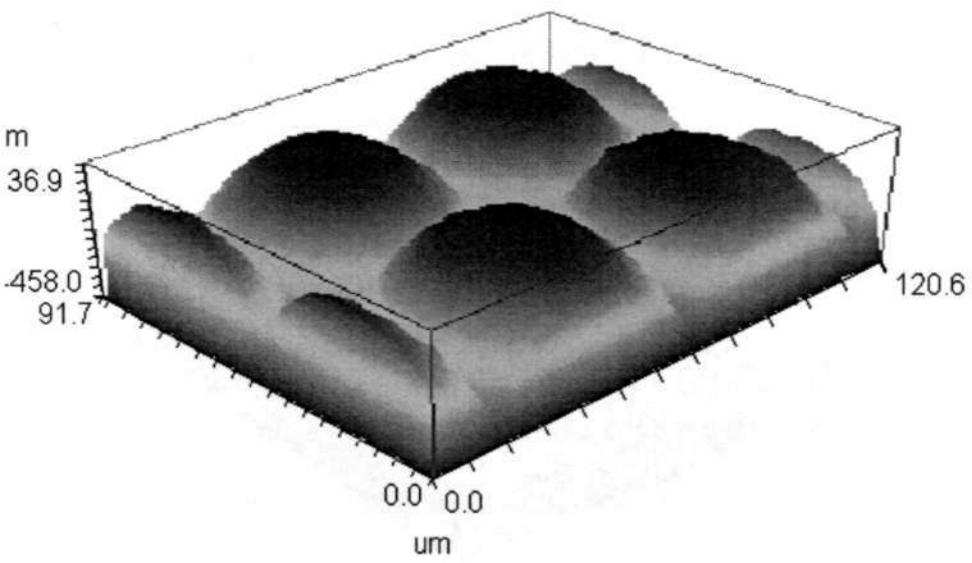

Fiurge 3-4b. 3-D profile of one 2X2 array.

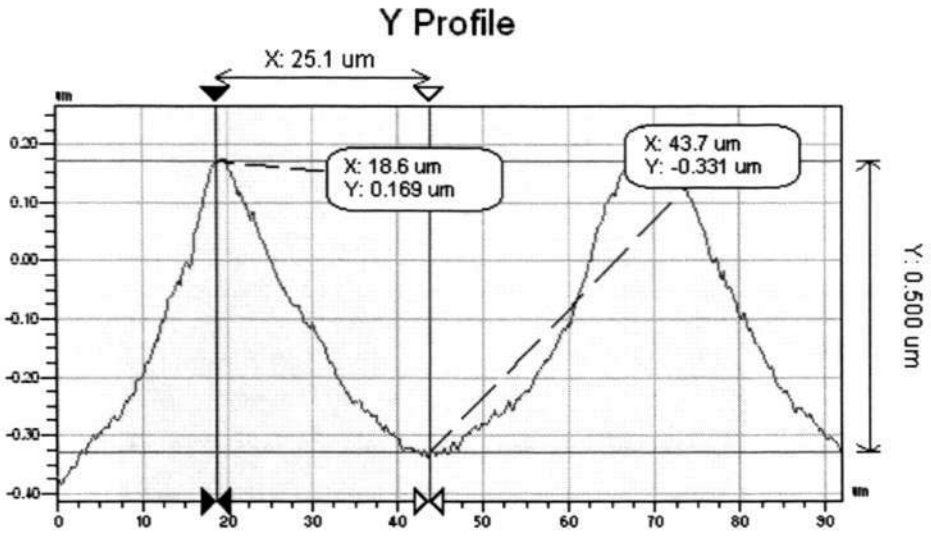

Fiurge 3-5(a). 2-D profile for negative microlens.

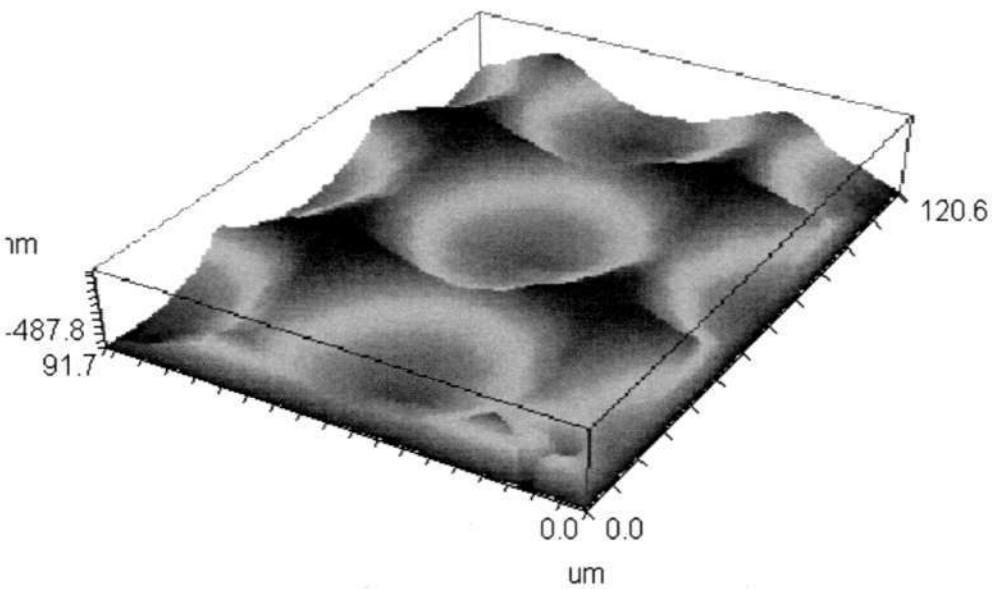

Figure 3-5b. 3-D profile for negative microlens.

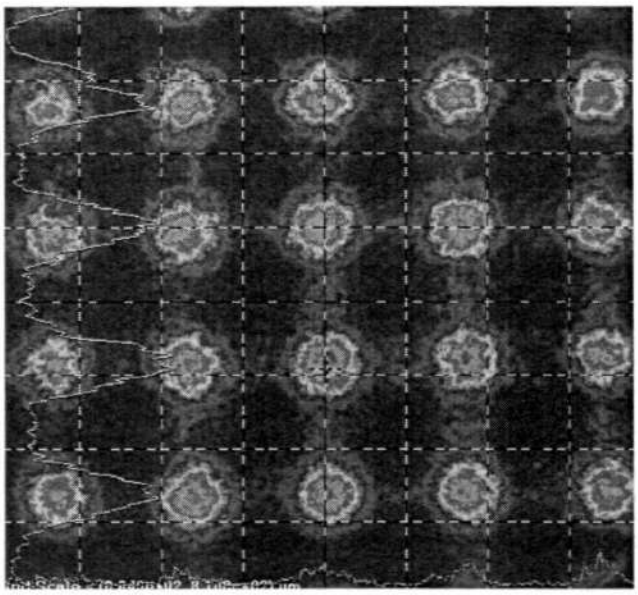

Fiurge 3-6(a). 2-D profile of optical intensity distribution of the focal spot. The grid size is 20μm.

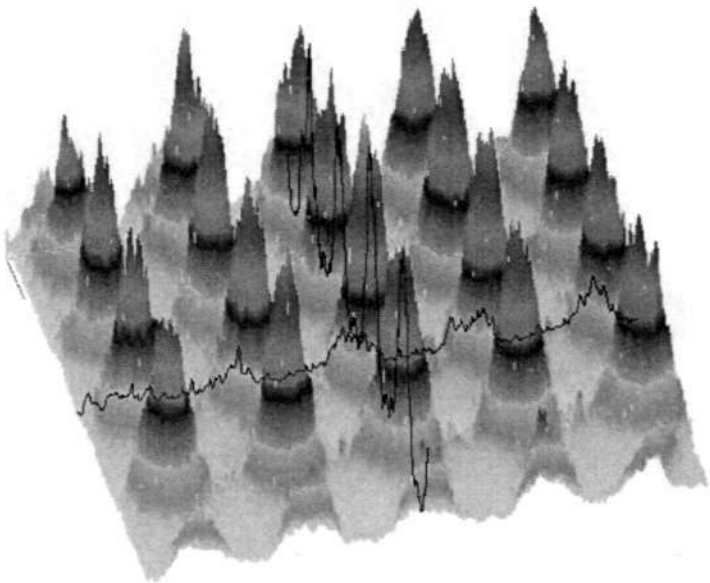

Fig. 3-6(b). 3-D profile of optical intensity distribution.

3.2.2 Fabrication of blazed gratings

In this section, we show some results for the fabrication of blazed gratings with development based hybrid sol-gel glass by using a grey scale mask. The

experimental setup used in the fabrication process is the same as that shown in Fig.3-1. Figure 3-7 shows the surface profile of a blazed grating with a pitch of about 20μm and a height of approximately 1.206μm. The surface profile of the grating was measured using an optical interferometer.

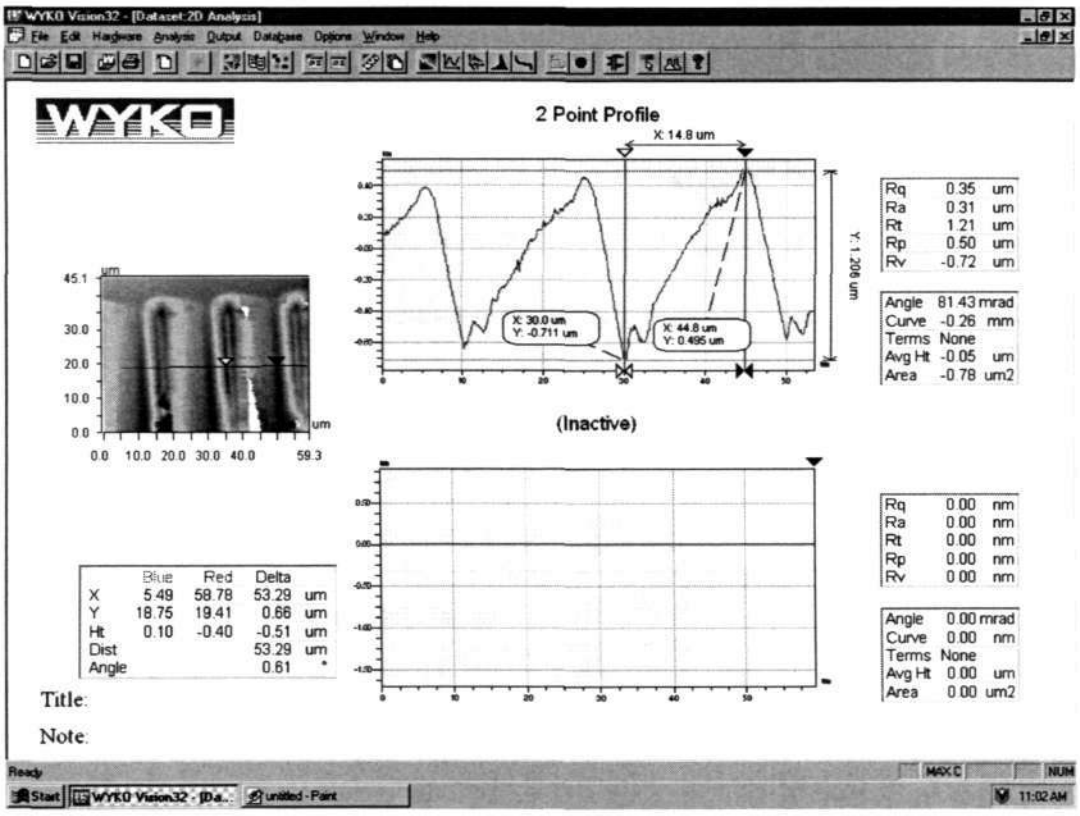

Figure 3-7. Surface profile of blazed gratings with a pitch of about 20μm.

Figure 3-8 shows the surface profile of another blazed grating with a pitch of about 10μm and the height of the gratings is about 900nm.

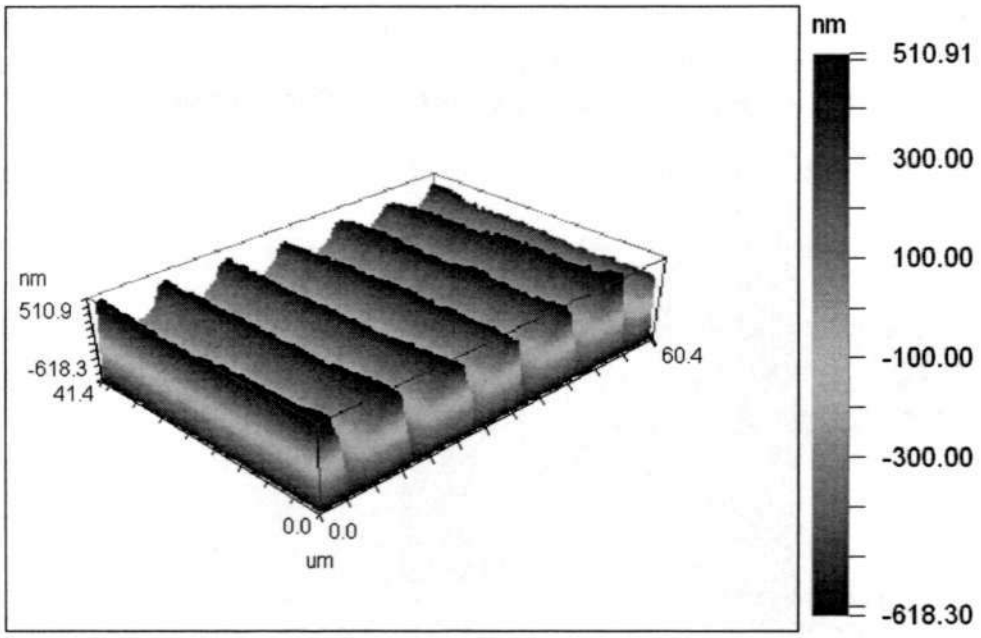

Figure 3-8a. 3-dimensional surface profile of blazed grating with a pitch of 10μm.

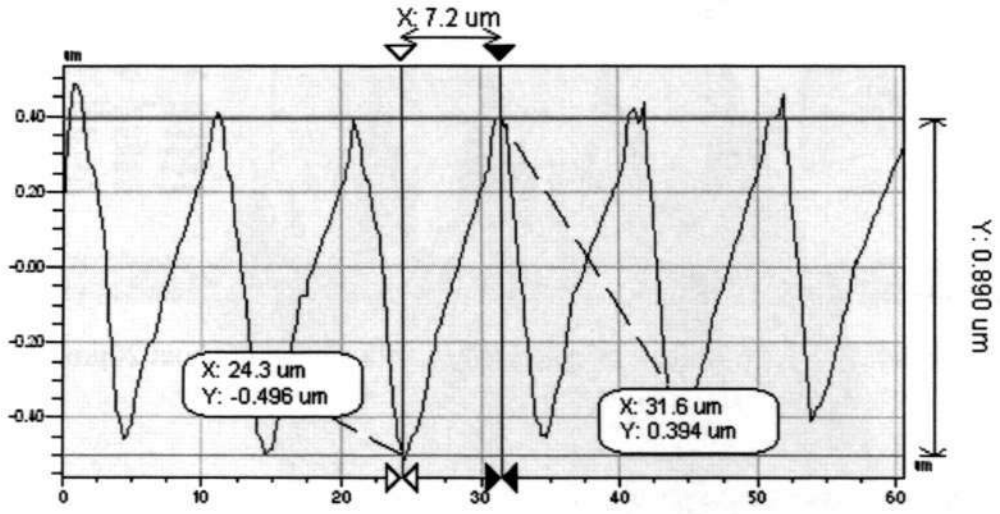

Figure 3-8b. 2-dimensional surface profile of blazed gratings with a pitch of 10μm.

3.3 Fabrication of continuous surface relief gratings in photosensitive development based hybrid sol-gel glass by using laser direct writing technique

Laser direct writing is a mature and flexible lithography technology, which has been developed for decades. This technique is more suitable for the fabrication of prototype structures with flexibility and versatility in the laboratory. Neumann et al. have successfully fabricated surface relief structure in dry, self-developing photopolymer films by using direct laser writing [22].

In this section, we describe the fabrication and characterization of a continuous relief structure in hybrid sol-gel glass by laser direct writing. The sol-gel glass used in our experiment is an organically modified SiO_2/TiO_2 hybrid glass synthesized at room temperature. As an example, a blazed grating was fabricated in the sol-gel material.

The laser source employed in our laser writing system is a 325 nm He-Cd laser with a maximum power of 200 mW. An acousto-optic modulator (AOM) was used as a beam blanker to control the 1^{st} diffraction order by making the AOM "on" and "off" for deflection of the beam from the aperture stop. The laser beam was focused onto the sol-gel samples through an optical microscope. The laser writing system has a lateral resolution of about 3 μm. Figure 3-9 shows a schematic diagram of the laser direct writing system setup.

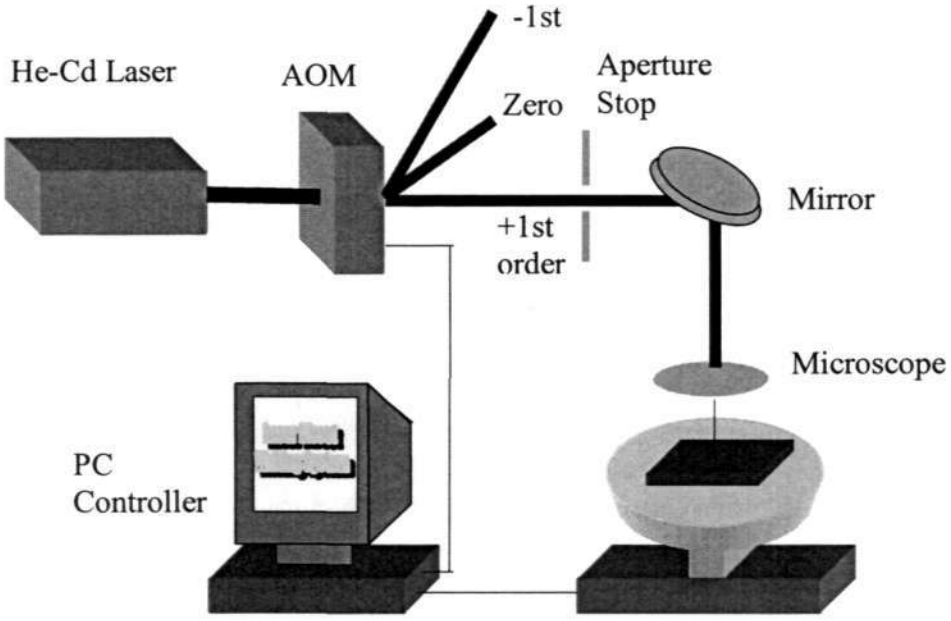

Figure 3-9. Schematic of the laser direct writing system.

The laser beam intensity is controlled by an Acousto-Optics modulator (AOM). The range of AOM value is from 0 to 10. The relationship between AOM value and optical intensity of UV laser beam was obtained by measuring the intensity of laser beam when varying the AOM value. One generic equation that shows the relation between laser beam intensities and values of AOM is represented as follows:

$$AOM = -0.08146 \times In\left(1.2625 \times 10^{-16} I\right) + 2.00119 \times \left(I - 0.5\right)^{0.3189} \qquad (3\text{-}3)$$

Figure 3-10 shows the relationship between the UV beam intensities and the AOM values. It is clearly seen from Figure 3-10 that the UV beam intensity has a nonlinear relationship with the value of AOM.

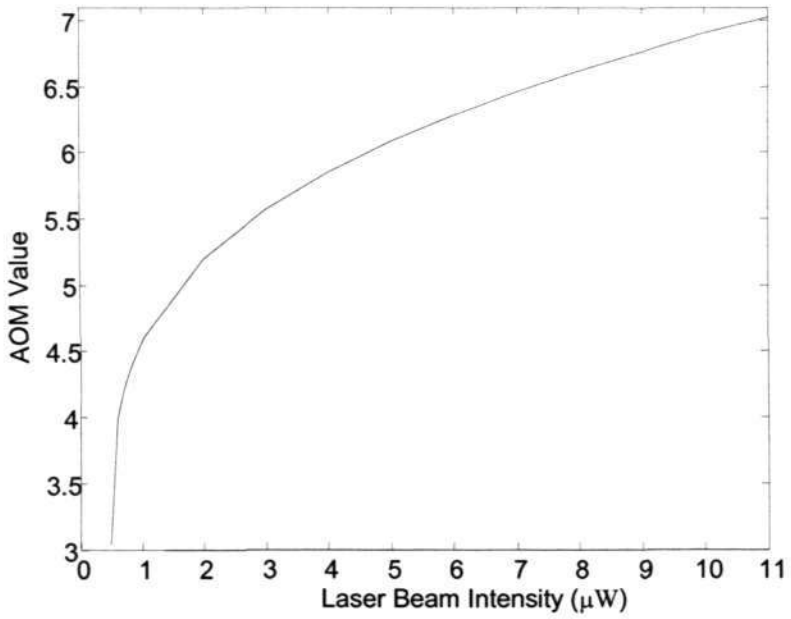

Fig.3-10. UV beam intensity as a function of the AOM value.

The relationship of the polymerized sol-gel film thickness and the value of AOM is shown in Figure 3-11. The plot shows that the thickness of the hybrid sol-gel glass was reduced to zero or reached a maximum height when the values of AOM are <3.25 or >5.5 respectively. It can be observed from Figure 3-11 that the thickness of our hybrid sol-gel glass has a nearly linear response to the AOM values between 3.25 and 5.5. This characteristic is very important, as it would make our design simpler. As the UV beam intensity responses nonlinearly to the values of AOM, we can conclude that the thickness of hybrid sol-gel glass is nonlinearly related to the UV beam intensities. Therefore, we should not design and fabricate micro-optical elements according to the relationship between sol-gel film thickness and the laser beam intensity. Instead, we should make use of Fig.3-11, which is linear, to help us design and fabricate micro-optical elements. In addition, by substituting the values of the thickness and the refractive index of sol-gel together with the wavelength of

0.6328 μm, we can calculate the value of the phase difference. The following expression is used for this calculation,

$$\Delta\Phi = \frac{2\pi(n-1)h}{\lambda} \qquad (3\text{-}4)$$

where n = 1.52, ? = 0.6328 and h is the thickness of hybrid sol-gel glass. A phase difference from 0 to 2p is obtainable with reference to Figure 3-16, which makes it possible to fabricate various free space 3D micro-optical elements.

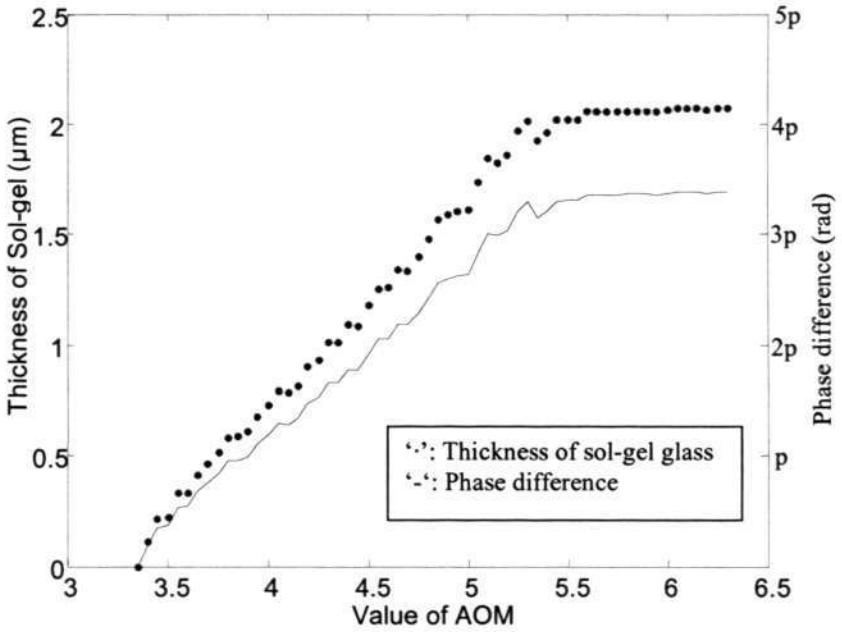

Figure 3-11. '.' Sol-gel film thickness as a function of the AOM value, '-' Phase difference caused by sol-gel film thickness as a function of the AOM value.

By using laser writing lithographic technique, we have designed and fabricated a blazed grating. The grating thickness is measured by a Dektak Surface Profiler (Veeco Metrology). Figure 3-13 shows the surface profile of the blazed grating. This blazed grating has a maximum height of 1.17μm, which is 0.05μm smaller than the expected height of 1.22μm. This is likely due to the shrinkage of the hybrid sol-gel glass during post baking. In addition, the humps on the grating surface are

probably caused by the big step size of the AOM. By reducing the step size of the AOM, we believe that a better surface can be obtained.

Figure 3-12 shows the photograph of a blazed grating fabricated by us and Figure 3-13 shows the surface profile of a blazed grating with three periods.

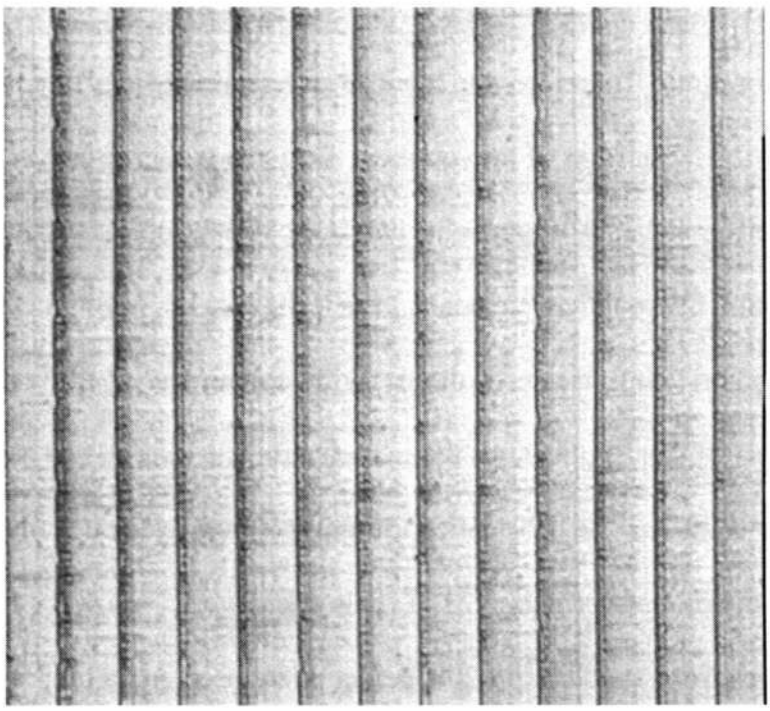

Figure 3-12. Photograph of a blazed grating.

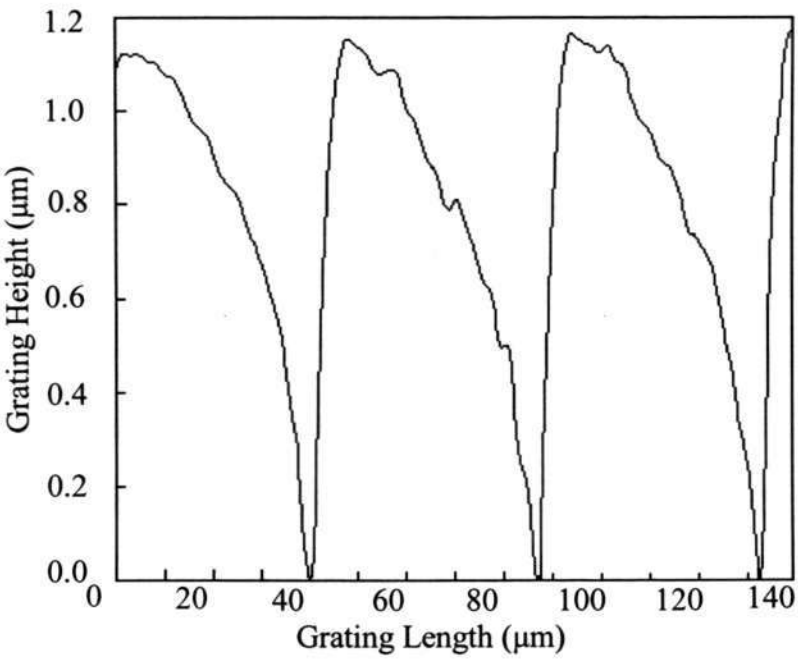

Figure 3-13. Surface profile of a blazed grating with three periods.

3.4 Fabrication of refractive microlens in photosensitive sol-gel glass by using electron beam lithography

When mask aligner and laser direct writer are used for the fabrication of microoptical elements, the minimum feature size is usually limited to 1μm due to the resolution limit. Therefore, the mask aligner and the laser direct writer are not suitable for the fabrication of microoptical elements with submicron sized features. However, electron beam lithography has been widely used for the fabrication of high-resolution microoptical elements. This technique has been successfully used as a tool for fabricating master patterns with submicron sized features in mask fabrication as well as applications in microelectronics. Recently, it has been used by J.T.Rantala et al for the fabrication of microoptical elements in photosensitive SiO_2/ZrO_2 hybrid sol-gel glass [23, 11]. In their work, relatively higher electron beam dosages from 10μc/cm^2 to 2000μc/cm^2 were used and a binary grating with a 500 nm line width and a 1μm pitch was obtained. In this section, we present the fabrication of microoptical elements such as microlens in a SiO_2/TiO_2 photosensitive hybrid sol-gel glass with the electron beam lithography technique.

The electron beam exposure of the sol-gel film was implemented on a SEM (LEO982), which was upgraded and controlled by an ELPHY Quantum software. An accelerating voltage of 25 keV and a beam current of 80 pA were employed in the electron beam lithography. Calibration of the sol-gel film thickness as a function of dosages was carried out by writing a binary grating with a period of 15 μm. After exposure, the sol-gel film was developed in isopropanol-2 (IPA) for 1 minute to remove the unexposed areas. The film thickness was measured by a Dektak Surface Profiler (Veeco Metrology).

Usually, the photoinitiator is added into the sol solution to make it photosensitive. When exposed to UV light, the free radicals formed by the photoinitiator can cause a subsequent 3-D polymerization in the hybrid sol-gel film. Therefore, it divides the sol-gel film into a soluble part in the unexposed areas and an insoluble part in the exposed areas. However, for electron beam exposure, the high energy of the e-beam is strong enough to break the chemical bonds such as double carbon bonds. The polymerization of sol-gel film could happen in the exposed regions even without photoinitiator and this phenomenon was reported in our previous work in [24].

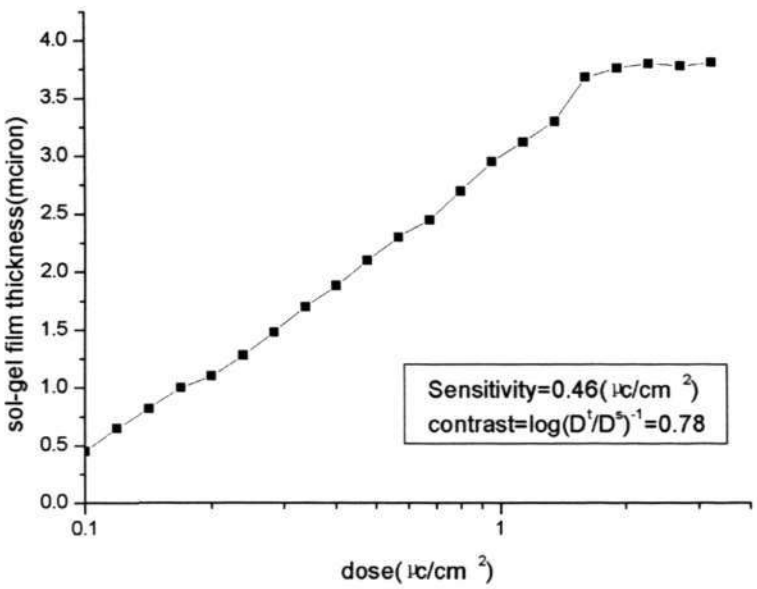

Fig.3-14. Sol-gel Film thickness versus electron beam dosage.

Figure 3-14 shows the relationship between the sol-gel film thickness and electron beam dosages. It is noted that a good linear relationship exists between the sol-gel film thickness and the electron beam dosages, which is useful for the control of exposure parameters in the fabrication. We can see from the Figure 3-14 that the film thickness after exposure can be as large as 4μm, and this may make the

fabrication of refractive microoptical elements such as refractive microlens possible. The measured contrast value is 0.78, which is determined by,

$$contrast = \log\left(D^t / D^s\right)^{-1}, \tag{3-5}$$

where D^t is the dosage required for 100% crosslinking of the film and D^s is the dosage corresponding to a point where the cross-linking starts. The sensitivity of the sol-gel material is 0.46 μC/cm^2, defined by the dosage that causes the remaining film thickness to be 50% of its original thickness.

Based on the above calibration results, we have fabricated one microlens with 250 μm diameter and 2.05 μm sag height as an example. The solid line in Fig.3-15 shows the surface profile of the fabricated microlens measured by surface profiler. The theoretical surface profile is represented by a dotted line in the same figure as a comparison. As can be seen, the resulted surface profile is very close to the designed one although the sag is slightly lower and the diameter is slightly smaller due to the shrinkage during postbaking. However, the slightly rough surface profile prompts us to optimize the process in future.

To enhance the surface corrugation quality of the lens, we should optimize the electron beam lithography process by using more grey levels (presently we use only 13 grey levels). This will enable us to fabricate a better spherical surface and thus improve the surface smoothness. In addition, defocusing the electron beam during exposure will also produce a smoother surface profile. Another alternative will be to lower the sensitivity of the sol-gel. With a lower sensitivity, a smaller step size in EBL point-to-point writing will be possible and this may result in a smoother surface profile. With the current high sensitivity, the smallest step size is about 0.5 μm. The disadvantage of lower sensitivity is that it requires a longer exposure time.

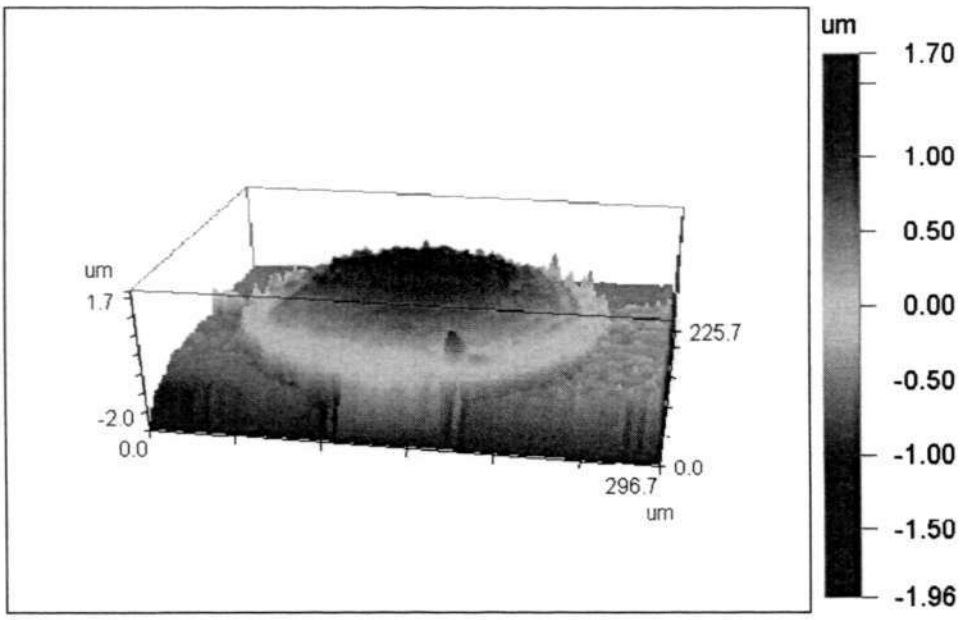

Fig.3-15a. Measured 3D profile of the microlens with a diameter of 250 μm and sag height of 2.25 μm.

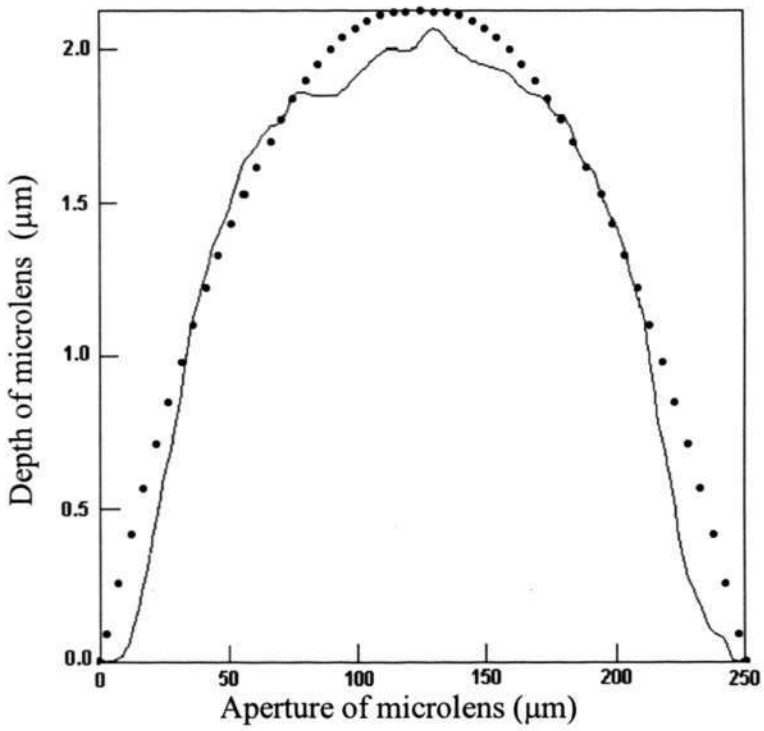

Fig.3-15b. Measured surface profile of the microlens with a diameter of 250 μm and sag height of 2.05 μm.

3.5 Fabrication of sinusoidal profile gratings in photosensitive hybrid sol-gel glass by using holographic interference method

Many methods including contact imprinting in mask aligner, laser direct writing, electron beam lithography and holographic interference, have been used for fabrication of gratings. In these methods, contact imprinting and laser direct writing techniques are suitable for fabrication of gratings with a pitch for several micron, while electron beam lithography and holographic interference can produce a grating with a submicron period. Electron beam lithography is a relatively expensive technology and is not suitable for fabrication of gratings in a large field. Holographic method can produce gratings with a fine pitch in a large area. Additionally, this technique is simple and it can be easily controlled.

Holographic interference method is using a two-beam interference pattern that has a sinusoidal intensity distribution to imprint a sinusoidal grating into the photosensitive sol-gel film. This method has been used by many authors for fabrication of diffraction gratings with the pitch size as small as 500nm [25].

In this section, an investigation of this method for fabrication of diffraction gratings is presented extensively.

The optical setup is shown in Figure 3-16, where a laser beam was filtered by a pinhole to produce a spherical wave. A rotation stage with a mirror and a sample plate were mounted in far field from pinhole so that the waves received on the sample plane and the mirror plane are approximately plane waves. The grating period will be decided by the laser wavelength and the angle between the two-interference waves, which can be determined by,

$$T = \lambda/(2\sin\theta) \qquad (3\text{-}6)$$

where, λ is the wavelength, in our case it is 325nm for a He-Cd laser. With this setup, gratings with submicron sized period can be fabricated. The following pictures show some preliminary results.

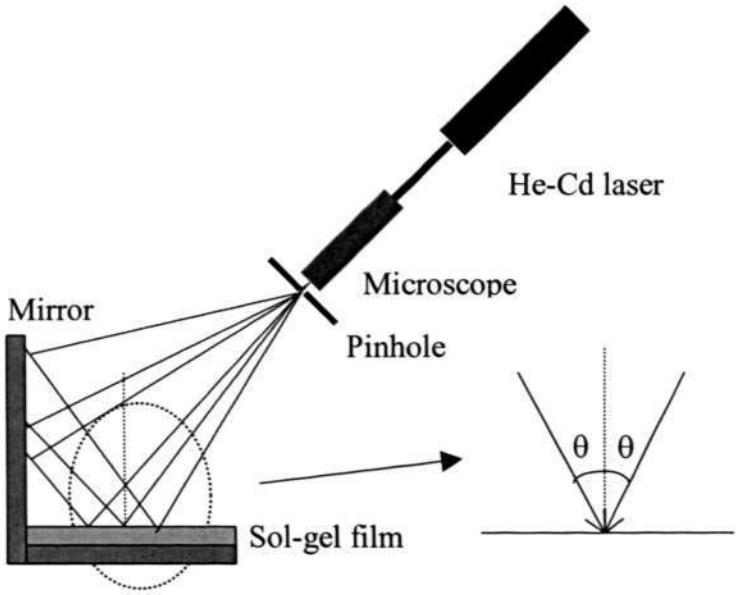

Fig.3-16. Optical setup for holographic interference.

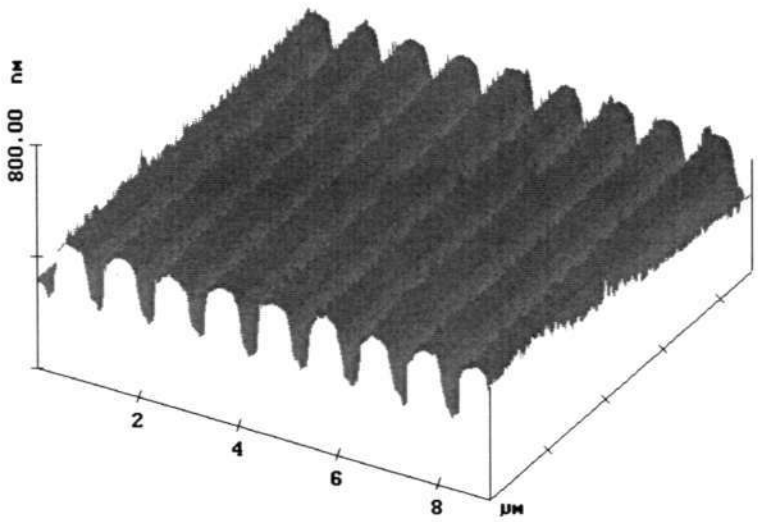

Fig.3-17 AFM picture of a 1μm pitch sinusoidal grating.

Fig 3-17 shows a sinusoid grating with a period of 1μm and a depth of about 200nm. It is seen that the grating profile is a sinusoidal profile. However, it should be noted, the exposure time and other parameters should be controlled carefully to avoid the profile divergency from sinusoid.

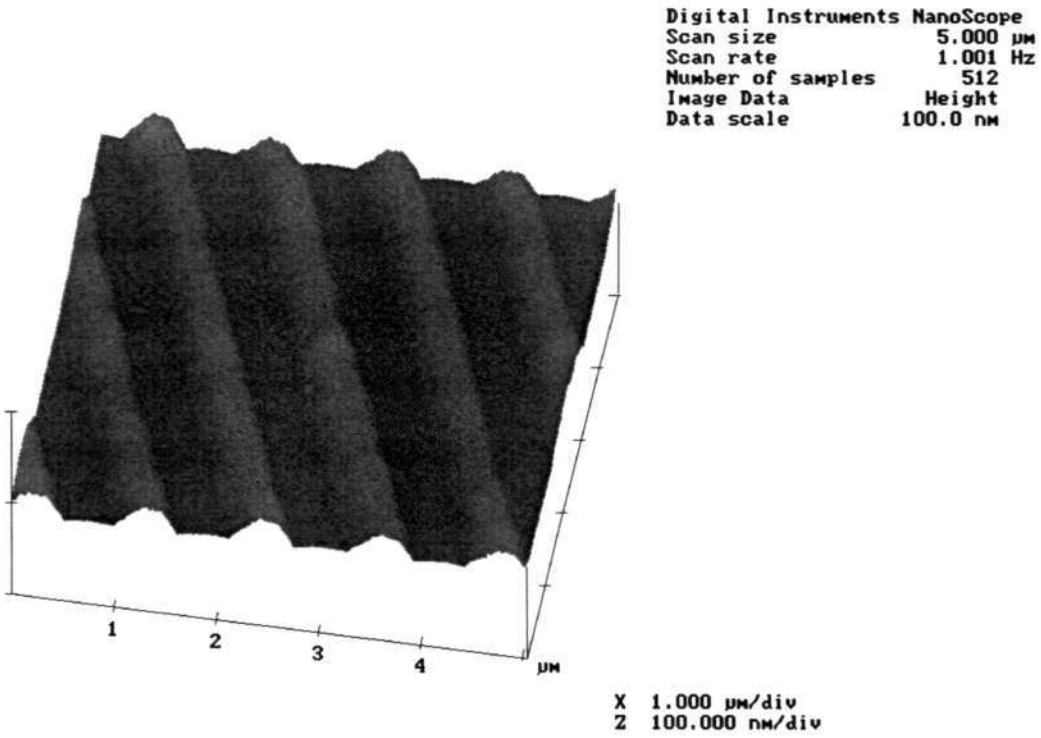

Fig. 3-18. AFM picture of a 1μm grating with insufficient exposure time.

This picture shows a grating with a period of 1μm and the line width is about 500nm. Clearly, the grating profile is different from sinusoidal, which is because the exposure time is not long enough so that the intensity smaller than peak intensity is not big enough to polymerise the sol-gel film.

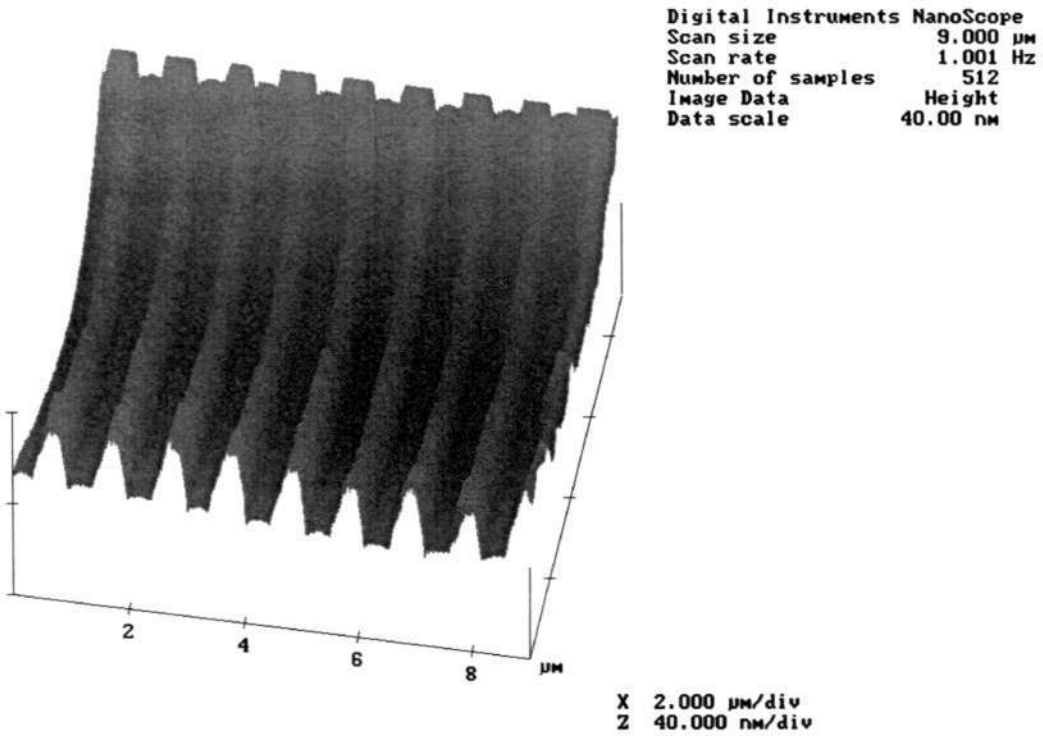

Fig.3-19. A sinusoidal grating imaged at the edge of the grating field.

This picture shows a grating formed at the edge of the interference field. The grating line is curved and the reason for that is explained as follows,

Ideally, the grating is formed by the interference of two plane waves. For the experiment setup shown in Fig.3-16, the interference fringes are actually formed by two spherical waves. The interference pattern is a coherent family of hyperbolae [26], and thus it has a phase discrepancy from the linear grating. The discrepancy is calculated from,

$$\phi(x,y)=\frac{2\pi}{\lambda}\left(\sqrt{(a+x)^2+y^2+c^2}-\sqrt{(a-x)^2+y^2+c^2}-\frac{2ax}{\sqrt{a^2+c^2}}\right) \qquad (3\text{-}7)$$

where, the parameters used in this equation is shown in the following figure,

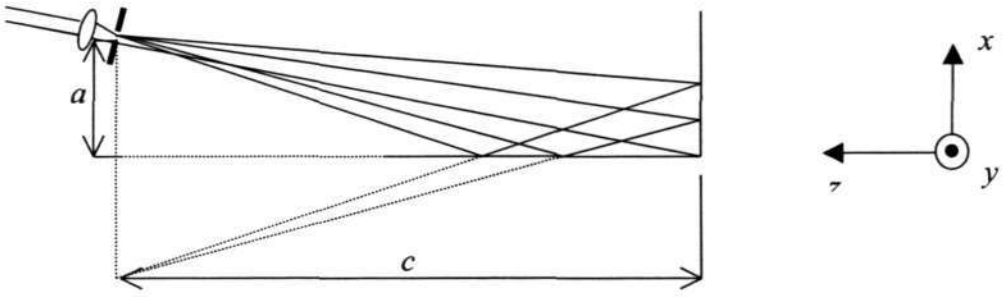

Fig.3-20. Parameters used in equation (3-7).

The last term in equation 3-7 is the linear phase of a grating that has a period of $p = \frac{\lambda}{2\frac{a}{\sqrt{a^2+c^2}}}$. This is consistent with equation of 3-6 with $\frac{a}{\sqrt{a^2+c^2}} = \sin\theta$.

The θ is the beam incident angle shown in Fig.3-16. If we assume the first two terms have equal values, the interference pattern formed from two spherical waves will be a linear grating with the same period as that of two plane waves. The conditions for the first two terms have equal values are,

$$c >> a \;\&\; c >> x \qquad (3\text{-}8)$$

Where $c >> a$ means the interference fringe is formed in a far field and usually c is larger than 1 meter and $c >> x$ means the spherical wave can be approximated as a plane wave over small distance. Thus, the final interference fringe will be a linear grating with the conditions of 3-8 are satisfied. If the conditions of 3-8 are not satisfied, the final interference fringe will sure has a slight curvature due to the phase discrepancy from linear gratings described in equation 3-7. Hence, we can conclude the curved gratings lines observed at the edge of the interference field is due to the interference field is not far away from point source or the spherical wave can not be approximated as a plane wave at the edge of the interference field.

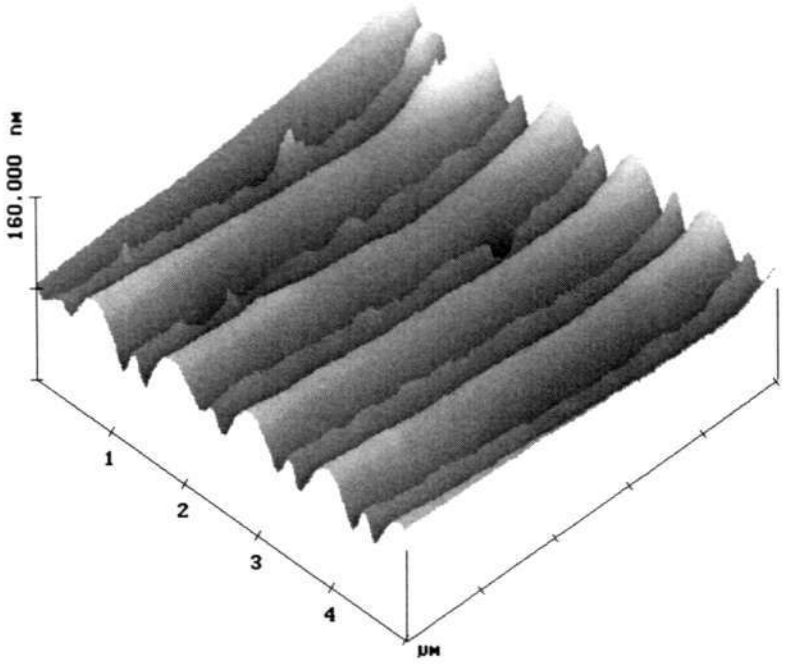

Fig.3-21. AFM picture of a 1μm pitch grating with a overexposure of UV light.

This picture shows a grating formed from a longer exposure time. As the grating pitch is very small, 1μm, so the proximity effect (means the exposure area is affected by the backscattered light or electron from adjacent area) which affects the grating profile becomes very important. It is observed that there is a subpeak formed in the valley between the main peaks. This can be eliminated by controlling of the exposure time accurately. In addition, during the development process, some resolved particles of gel film are not removed away. These particles attached to the grating surface and causes the surface to be rough.

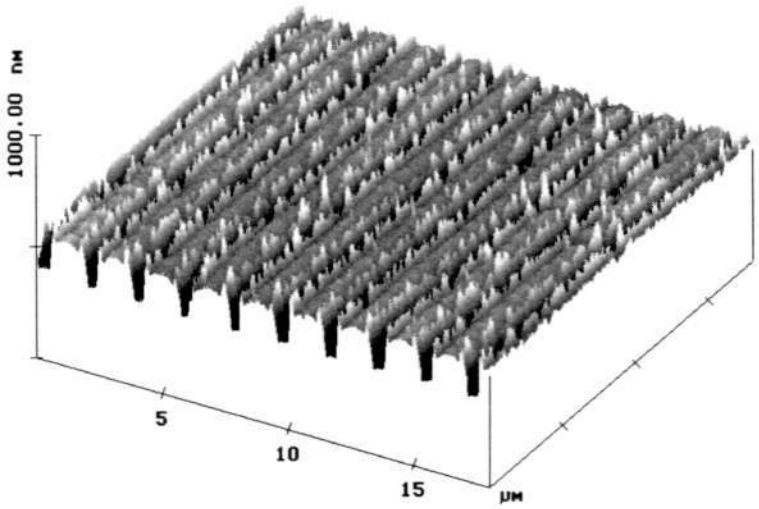

Fig.3-22. A 2μm-pitch grating fabricated with an overexposure time.

This picture shows a grating with a pitch of 2μm. Clearly, the grating profile is approximately binary, which is significantly divergent from sinusoidal. This phenomenon also results from a longer exposure time. However, in this case, there is no subpeak formed. We believed that this is because the grating period, being larger, will be less affected by the proximity effect compared to smaller gratings periods.

3.6 Discussions and conclusions

In this chapter, fabrication of microoptical elements in photosensitive hybrid sol-gel glass by using high energy beam sensitive grey scale mask, laser direct writing technique, holographic interference and electron beam lithography was demonstrated. It can be seen from the fabrication of microoptical elements by using

grey scale mask that exposure time is a very important parameter which can determine the final surface relief thickness after development. This conclusion is also applicable for holographic interference method used for fabrication of sinusoidal grating. As for laser direct writer and electron beam direct writer, the most important parameter is the exposure dosage, which controls the final surface relief thickness of sol-gel glass after development. However, when compared with previous two methods, it is a challenge to get a relatively smooth surface by using these two direct writing methods. The reasons lie in two aspects. One is the step size and the other is the influence of the proximity effect. Generally speaking, the smaller the step size, the smoother the surface profile. However, with the reduction of the step size, proximity effect will be a significant problem that will reduce the whole surface relief thickness. For previous two methods, the grey scale mask can provide a minimum step size of 100nm and the holographic interference method is a continuous optical intensity distribution field, thus a smooth surface profile can be easily obtained. The only parameter that affects on surface roughness is the development process, which is a wet etching process where chemical reaction takes place during development.

In addition, laser direct writing and holographic interference method can provide a large working field. Therefore a large size of microoptical elements can be made that usually several centimeters square or more is possible. While for grey scale mask and electron beam lithography, the working field is relatively small due to the expensive high-energy beam sensitive glass and the low freedom of the deflection of electron beam by condense magnetic lens. Therefore the geometrical size of the fabricated microoptical elements is limited to several millimeters.

It is also noted that the sol-gel material with a new recipe reveals a good linear response to UV light, which is a great improvement compared with the calibration results of reference [15]. Synthesis of the sol-gel in reference [15] is shown in Figure 3-23. The calibration curve of reference [15] is shown in Figure 3-24. With a linear sol-gel material, it is easier for us to design and fabricate microoptical elements with a linear surface profile such as blazed profile gratings. Figure 3-25 and Figure 3-26 show the blazed gratings fabricated with the same grey scale mask. Clearly, with the improved linear sol-gel material, it shows a better and smoother surface profile. The mask has a period of 20 μm and there are 10 grey levels in each period. The grey levels are realized by the optical densities ranging from 0.12 to 1.12 linearly.

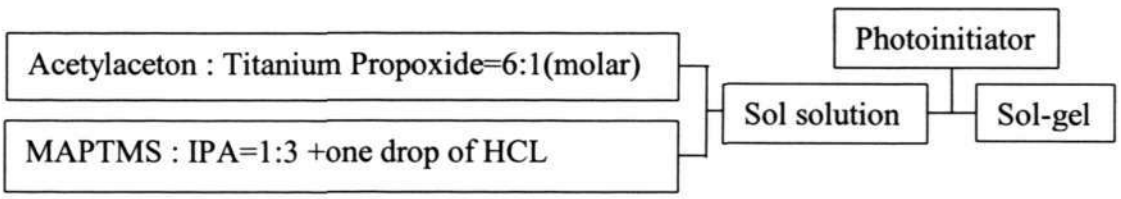

Fig.3-23. Schematic of sol-gel synthesis in reference [15].

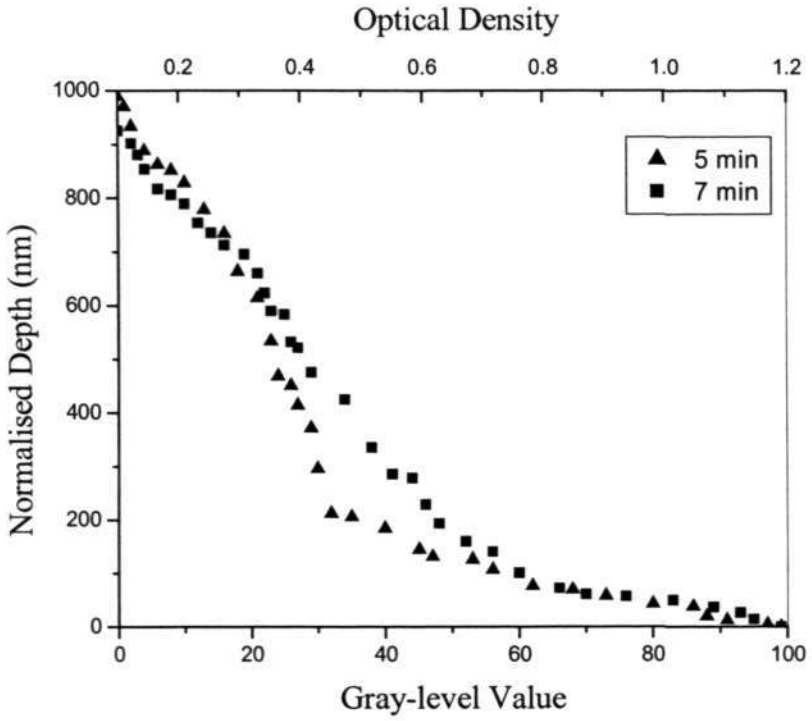

Fig.3-24. Calibration curve of sol-gel in reference [15].

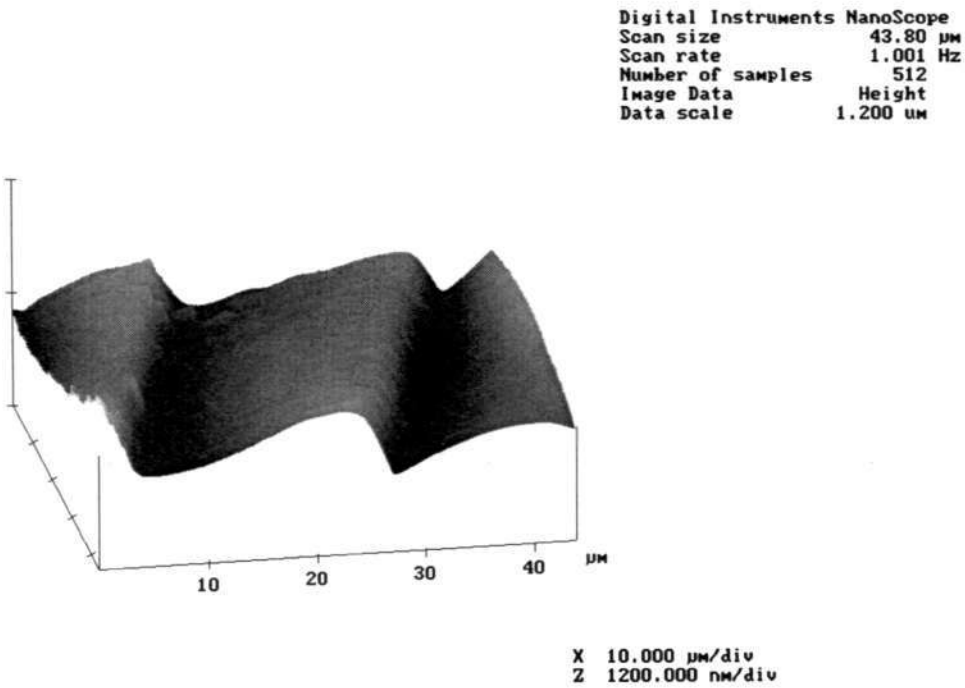

Fig.3-25. Blazed grating fabricated with sol-gel in reference [15].

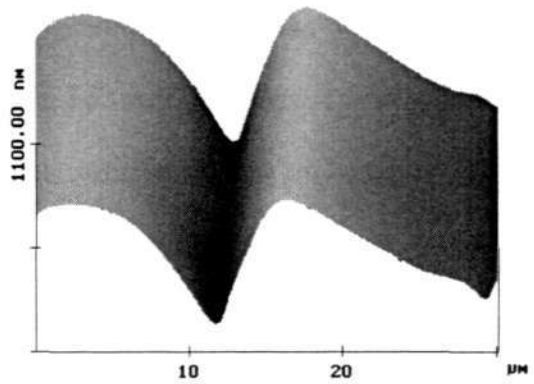

Fig.3-26. Blazed grating fabricated with new recipe of sol-gel material.

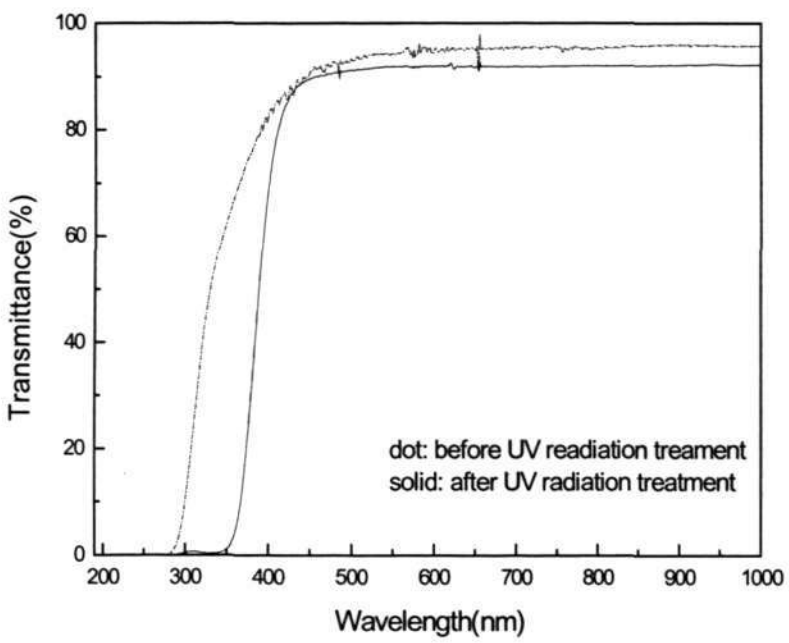

Fig.3-27. The transmittance of the sol-gel synthesized in reference [15].

A reasonable interpretation can be obtained by understanding the transmittance of the previous and present sol-gel materials, which are shown in Figure 3-27 and

Figure 2-3 respectively. Comparing the figures, we can see that the transmittance of the sol-gel material synthesized with the new recipe has a slight shift to the ultraviolet band in Figure 2-3, which is known as the ultraviolet shift effect. The shift means that the sol-gel material has greater transmittance and hence smaller absorption in the area close to the UV cut-off point. In Figure 3-13, the UV cut-off wavelength is 275 nm with the old recipe of sol-gel synthesis. However, in Figure 2-3, the cut-off wavelength has been extended to 200 nm for the new recipe. For the mask aligner with an emission peak at 365nm, the absorption of the sol-gel material is reduced from 30% in Figure 3-13 to 14.5% in Figure 2-3. It is known that the small absorption resulted in less UV sensitivity of the sol-gel material, which consequently improved the linearity of the dynamic response.

As for the ultraviolet shift effect of the transmittance curve, we believe that it is caused by the improved inorganic-organic composite structure of the SiO_2/TiO_2 films. For the composition of the improved sol-gel synthesis, the recipe has been modified by adding deionised water to the sol-gel. It is understood that, with introduction of the deionised water, the sol solution is hydrolyzed more efficiently and also the condensation also happens. Therefore, the silicate backbone is formed in the modified sol-gel film. While for the old recipe in reference [5], there is no deion water, so the hydrolysis never happens and the silicate backbone should not exist in the sol-gel film. It is believed that the existence of the silicate backbone results in the ultraviolet shift effect of the transmittance curve.

In conclusion, we have demonstrated that the fabrication of microoptical elements in photosensitive hybrid sol-gel glass. However, to get a microoptical elements, several parameters should be controlled accurately such as exposure time, exposure dosage, developing time and so on.

Chapter 4. Fabrication of microoptical elements in self-development photosensitive hybrid sol-gel glass

Self-development of photosensitive sol-gel film means that the corrugation can be formed only with a single-step exposure and without further development process needed. In practice, two response forms, i.e. trough or ridge, to UV light were used to fabricate optical structures. For the trough formation, demonstrated by D.Blanc *et al*, a pre-cure of the sol-gel film under UV exposure was performed so that the monomers in the film was consumed, and then followed by a longer time exposure to form the grooves in exposed regions due to polymerization and densification of the film [27]. With the same material, a submicron period diffractive grating was also fabricated through a phase mask with a period of 1 micron [28]. A model based on elastic deformation under photo-induced stress has been developed by D.Blanc *et al* to explain the relief formation in this material [29]. In this case, the volume growth (means the film thickness will increase and thus the volume increase upon UV light exposure) phenomenon happens when the sol-gel film is exposed to UV light and thus the ridge is formed in the exposed regions. The volume growth effect was reported by Neumann for photopolymers and by Rantala for hybrid sol-gel materials in [22] and [30] respectively. Rantala explained the phenomenon based on a theory of monomer diffusion model. However, a monomer diffusion theory can only explain this phenomenon partially. It is learnt that during UV exposure, the monomers in the exposed regions are consumed and the monomers in the unexposed regions migrate into the exposed regions to continue the polymerization reaction. As a result, the ridge is formed in the exposed regions due to the film stress caused by monomer diffusion.

The self-development technique has an advantage over the one-step sol-gel fabrication processes in terms of easy fabrication and good quality of the micro-optical elements. The elimination of the development step will significantly improve surface roughness of the micro-optical elements in sol-gel glass.

In this chapter, we synthesized a new self-development photosensitive sol-gel glass and applied this material for fabrication of microoptical elements with multilevel structures by using various methods.

4.1 Synthesis of self-development photosensitive sol-gel glass

The hybrid sol-gel material was prepared by hydrolysis of 3-(trimethoxysilyl) propyl methacrylate (MAPTMS) in isopropanol and acidified water with a molar ratio of 0.04:0.048:0.053, then 0.01 mol of titanium propoxide ($Ti(OCH)_4$) was hydrolyzed in 0.04 mol of acetylacetone in nitrogen environment. After 30 minutes, the two solutions were mixed with a molar ratio of 4:1 (Si:Ti). After 24 hours aging in room temperature, the sol solution was made photosensitive by adding into 3% (weight) of photoinitiator (bis (2,4,6-trimethylbenzoyl)-phenylphosphineoxide) and 1% (weight) of 1-hydroxycyclohexyl phenylketone and followed by another 30 min aging. The final sol solution was filtered and distilled so that it can be viscous enough to obtain a 10micron thick film with a spin speed of 3000rpm. The refractive index of this material is 1.50 when measured by a prism coupler.

4.2 Fabrication of continuous surface relief gratings in self-development photosensitive sol-gel glass by a laser direct writer and an user defined grey scale mask

In this section, we intend to explore the volume growth effect in the hybrid sol-gel glass for fabrication of 3-D micro-optical elements. It will be interesting to see that the volume growth can be controlled point-to-point by UV laser beam dosages for different profile heights. The experimental results indicated that the surface corrugation stabilizes after the postbake process.

In the experiment, the self-development photosensitive hybrid sol-gel glass was tested and characterized with a He-Cd laser (λ=325 nm) direct writing system. The ridges induced in the hybrid sol-gel film were defined by different laser beam intensities which were controlled by an acousto-optic modulator (AOM). Finally, different period saw-tooth gratings were successfully fabricated in the self-development sol-gel glass.

When the photosensitive hybrid sol-gel glass was exposed to the UV laser beam, a surface expansion phenomenon was induced and surface corrugation humps were formed in the exposed regions. As a result, a surface relief structure can be created in the photosensitive hybrid sol-gel glass without the development process needed. Fig.4-1 demonstrates the surface expansion phenomenon by applying the laser beam onto the samples to fabricate an array of lines with 100μm spacing. The laser beam intensity has a Gaussian distribution. It can be seen from the figure that surface expansion occurred in the exposed areas, where the surface corrugation followed the beam intensity shape. Between the test patterns, there were small

humps due to the proximity effect of the writing beams and monomers diffusion from the neighboring regions.

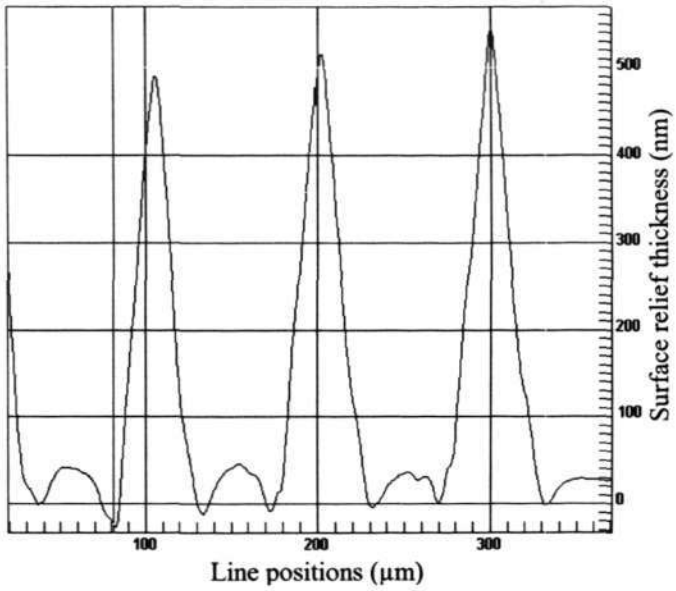

Figure 4-1. Surface relief thickness versus line positions.

Postbaking should be applied to the samples so that the structure can be hardened and stable. During the postbaking process, the temperature was raised to 160 °C. Fig.4-2 shows the corrugation depth change as a function of the postbaking time. It can be observed that 30 minutes of baking is enough to stabilize the structure.

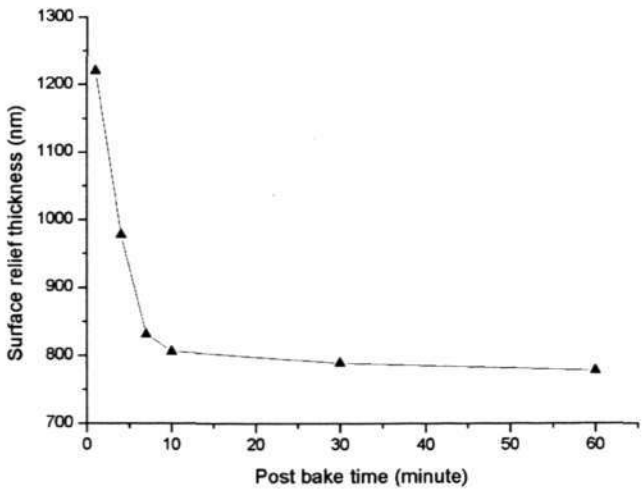

Figure 4-2. Surface relief thickness against post bake time.

To fabricate 3D surface relief structures with arbitrary profiles, one should be able to control the depth of the surface corrugation. We managed this process by controlling the laser beam intensity exposed onto the sol-gel film. Fig.4-3 shows the surface relief depths versus the laser beam intensities graph. It is observed that the surface corrugation depth increased when the laser writing dosage increased. This phenomenon is different from the dry polymer case reported in reference [21], where the maximum surface relief did not correspond to the maximum light intensity as a result of dye bleaching.

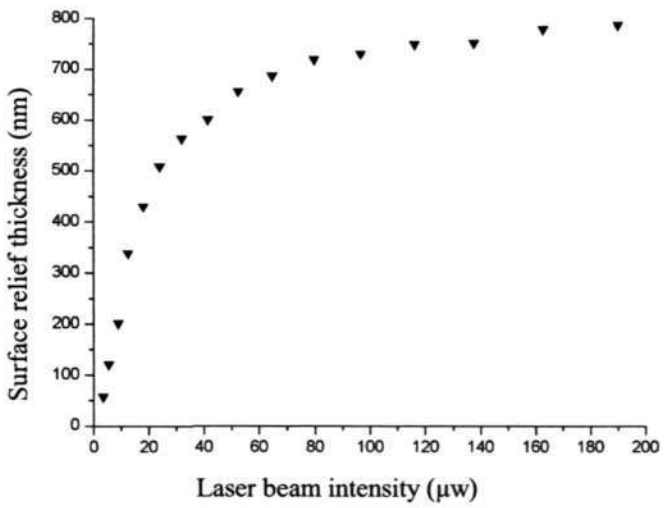

Figure 4-3. Surface relief thickness as a function of laser beam intensity.

As an example, the self-development sol-gel material was used for the fabrication of saw-tooth gratings. For different heights of the gratings, we need to expose the hybrid sol-gel film with the respective laser beam dosages as indicated in Fig.4-3. Furthermore, a critical calibration was implemented to choose an optimum point-to-point step size in laser writing for a smooth surface profile. We have tested three different step sizes with 7 μm, 5 μm and 3 μm respectively. The surface corrugation profiles were measured by a Dektak surface profiler (Veeco Metrology) and the

results are shown in Figure 4-4. From the figure, we can see that the best and the smoothest surface profile was produced by the smallest step size. This indicates that the volume growth response in the sol-gel can be controlled by the exposure dosage and the point-to-point step size. The grating in Fig 4-4c with a period of 27μm and a depth of 198nm was characterized with a He-Ne laser (λ = 633 nm). The experiment setup is shown in Figure 4-5. Both the measured transmission diffractive efficiencies and simulation results calculated based on the rigorous coupled-wave theory are listed in Table 3, where the results were obtained with normal incidence for truncated diffraction orders. It is seen that the measured results are in good agreement with the theoretical predictions. It is believed that the minor differences of the results are due to the imperfect surface relief structures and the variation of the refractive index that was affected by the monomer diffusion.

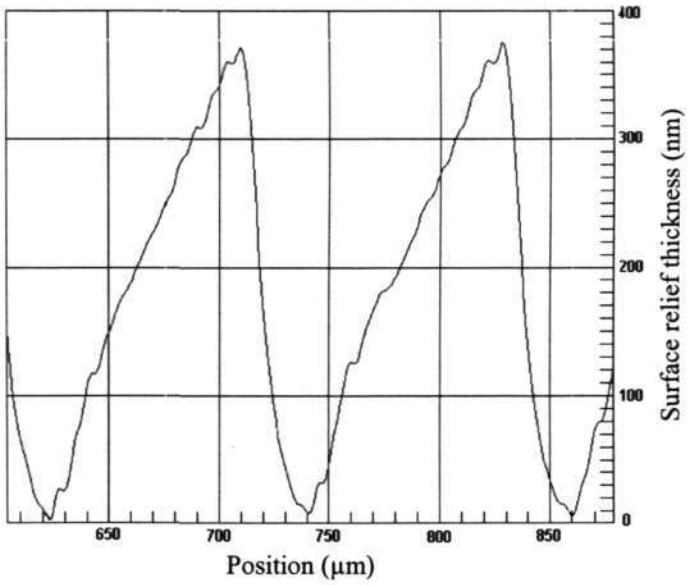

Figure 4-4a. Saw-tooth gratings fabricated with a step size of 7 μm.

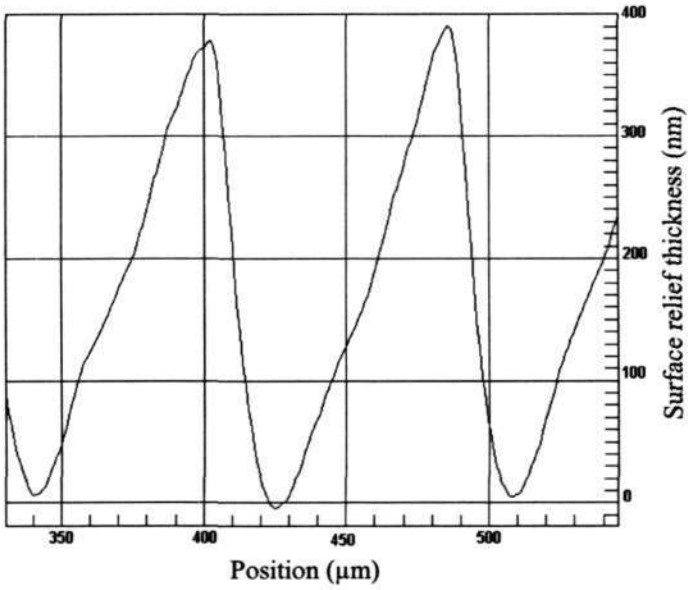

Figure 4-4b. Saw-tooth gratings fabricated with a step size of 5 μm.

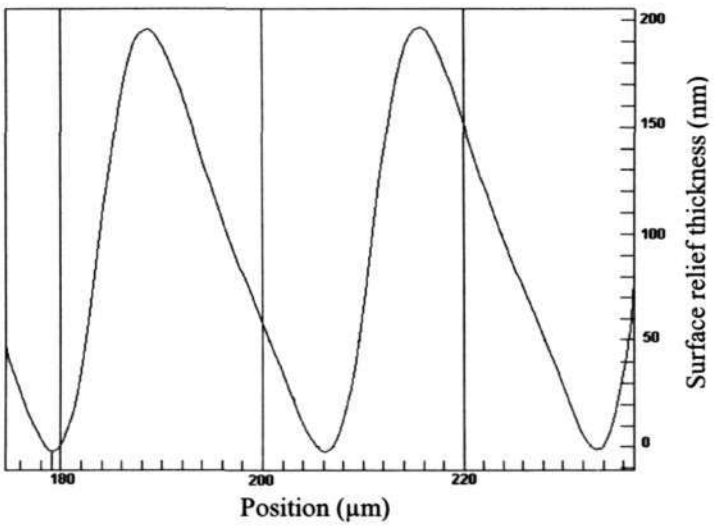

Figure 4-4c. Saw-tooth gratings fabricated with a step size of 3 μm.

Diffraction orders	-2	-1	0	+1	+2
Diffractive efficiency calculated (%)	0.64	3.09	88.68	1.60	0.48
Diffractive efficiency measured (%)	0.49	3.79	89.34	2.22	0.14

Table 4-1. Comparison of measured and calculated diffractive efficiency of a 27μm pitch grating.

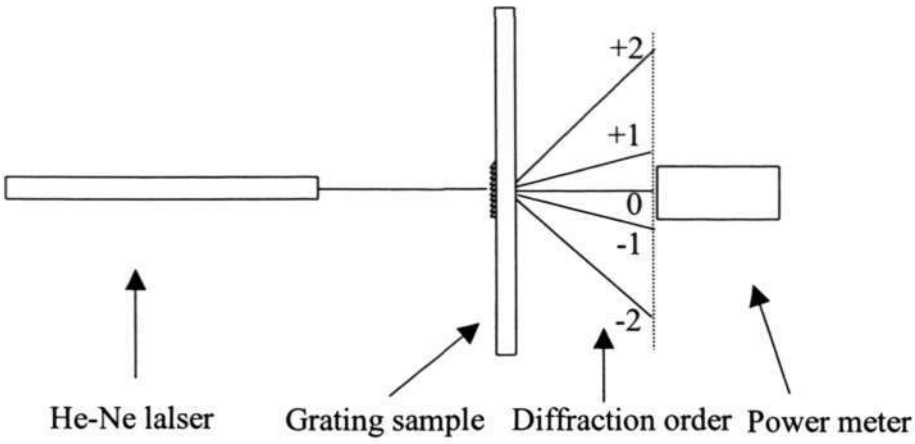

Fig4-5. Experiment setup for characterization of the grating in Fig.4-4c.

It is learnt from the preliminary results that the fabrication was limited by the volume growth mechanism and the laser direct writing system. Firstly, the spatial resolution was lowered by the surface stress induced when the monomers transferred from the unexposed regions to the exposed ones. Secondly, the overlapped point-to-point exposure due to the focused laser beam probe size could result in a reduction of the total relief thickness. As seen from Fig 4-3 and Fig 4-4, although the maximum surface relief thickness can be as large as 800 nm, the real heights of the gratings were limited to 400 nm. In addition, it is also observed that the smaller the step size, the smaller the grating height.

In conclusion, we have demonstrated the fabrication of continuous micro-optical structures in the self-development photosensitive hybrid sol-gel glass by laser direct writing. The depth of surface corrugation due to the volume growth in the exposed area was controlled by the laser beam intensity. With the calibration results, several saw-tooth gratings were fabricated with different step sizes of 7 μm, 5 μm and 3 μm. It is noted that the surface corrugation can be precisely controlled by the exposure dosage as well as the point-to-point lithographic resolution of the laser

direct writing system. The intrinsic surface roughness due to the chemical reactions in the development process has been eliminated.

In the previous section, we have showed how an acousto-optical modulator controlled laser direct writing system was used to form a continuous relief structure in a hybrid sol-gel glass. However, the roughness of the elements produced was limited by the step size used in writing. To get a smooth surface profile, reflowing technique could be used [31-32]. However, the reflowing technique is limited if we wish to obtain a quality spherical profile. If one expects a quality arbitrary surface profile, using a grey scale mask could be another option. High energy beam sensitive grey scale mask, a patent product of Canyon material Ltd. Inc, is an alternative for controlling the exposure light intensity onto sol-gel samples. It can confine the definite optical density within a very small region, say several hundred nanometers, and thus provide a fine control of volume growth of sol-gel film. With this method, a very smooth and user-defined surface profile can be expected. Grey scale mask has been widely used for fabrication of micro-optical elements with continuous relief structure in photoresist or photosensitive sol-gel film [33-34]. It is the reaction mechanism that leads to the formed ridge or trough to have a sinusoidal like shape, unlike a binary structure if a binary mask was used during UV exposure. Definitely, this will lower the resolution and increase the roughness of the surface profile when one tries to control the depth of the profile locally. If a grey scale mask was used, the grey levels should be utilized fully so that the surface roughness can be lowered as much as possible. However, increase of the grey levels of the mask will sacrifice the total depth of the structure formed due to the proximity interaction of the neighboring grey levels.

In this section, we try to investigate the self-development hybrid sol-gel film by using various period sizes in a saw-tooth grating mask. The resulted profile and the surface roughness were monitored by an AFM.

The grey scale mask used was induced by an electron beam in a high energy beam sensitive (HEBS) glass and includes three different period blazed gratings, 22μm, 11μm and 6μm with the same optical density range. The grey scale levels were generated by electron beam exposure with a fixed beam current of 93 pA and accelerating voltage of 25 KeV with different exposure time. The electron beam dosage was generated from 20 $\mu C/cm^2$ to 640 $\mu C/cm^2$.

To realize arbitrary surface relief structure, the relationship between the electron beam dosage used to induce grey levels in HEBS glass and the locally volume growth in photosensitive hybrid sol-gel glass should be first defined. A calibration grey level array with 21 lines, each having a dimension of 20μm×200μm was defined in HEBS glass by electron beam with a dosage range from 20$\mu c/cm^2$ to 640$\mu c/cm^2$. Next the sol-gel glass was exposed to UV light through the calibration plate. The UV exposure was implemented by a Q 2001CT UV-mask contact aligner (Quintel Corporation) with a peak emission at a 365 nm wavelength and an irradiance of 15 mW/cm^2. Figure 4-6 shows the schematic of the experiment setup using a grey scale mask. Figure 4-7 shows the relationship between the sol-gel volume growth and the electron beam dosage. The sol-gel samples used in this experiment have a thickness of 20μm. The calibration curve reveals a nonlinear response of surface relief thickness to the electron beam dosage. Once the relationship between the volume growth and the electron beam dosage is defined, we can make grey scale masks for microoptical elements with arbitrary surface

relief structure. Three period saw-tooth gratings were defined in the HEBS mask. When writing the masks, the electron beam dosage was varied from 20μc/cm^2 to 640μc/cm^2. In addition, the number of grey levels was not the same for different periods. The larger the grating period, the more grey levels were allocated.

Fig 4-8 illustrates the volume growth phenomenon of the sol-gel film. It can be seen clearly from the figure that a saw-tooth profile grating was imprinted into the sol-gel film. The region outside the grating region possesses a higher depth is as there is no grey level. Therefore this region is exposed with a maximum light intensity. Furthermore, the peak of the grating is a bit lower than the depth of the outside region due to the minimum grey level in this region.

Figure 4-9 shows the gratings fabricated with a period of 21μm, 11μm and 6μm respectively. It can be seen that the depth of the gratings is reduced as the grating period reduces. The depth of the 21μm grating is 125nm, which is the maximum of the three. As for the 11 μm and 6 μm period gratings, the depth is reduced to 50nm and 10nm respectively. It is noted that the surface profile of the 6μm period grating is the roughest, as it has the least number of grey levels used in one period. The grey levels used in one period for gratings with period of 21 μm, 11 μm and 6 μm are 21, 11 and 6 respectively. For each grey level, the width is 1 μm and it is written with a step size of 0.25 μm in e-beam exposure.

The reduction of the grating depth corresponds to the reduction of the grating period, which can be explained from two aspects. One is from the mass transmission or monomer diffusion theory. It is learnt that MAPTMS monomers diffuse from the unexposed area to the exposed area. This monomer diffusion can be controlled by a grey distribution of optical density. In the saw-tooth grating

fabrication case, the monomer diffusion was confined periodically and in each period, the monomers diffuse in accordance to the grey distribution of optical density. As a result, a saw-tooth surface relief profile was formed during UV exposure. For different periods of the grating, the monomer diffusion was confined periodically in a different region. The smaller the grating period, the lesser the monomers can be controlled in each period. As a result the grating depth will be smaller as well. The second reason is due to the proximity effect. In practical fabrication, the smaller the pitch size, the smaller the grating depth obtained when the same range of optical density was used.

In addition, the surface roughness was measured in the exposed area shown in Fig 4-9. The root mean square (Rms) of surface roughness in a 500nm×500nm square is 0.443nm (comparable with BK7 glass) which enables us to obtain a quality optical surface.

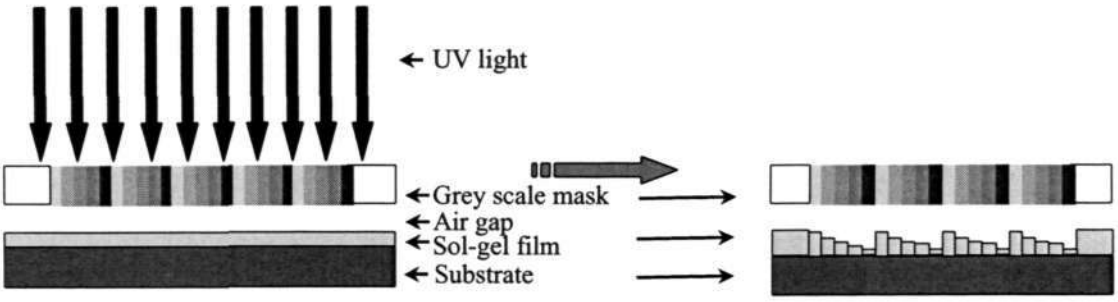

Fig.4-6 Schematic diagram of the experimental setup using a grey scale mask.

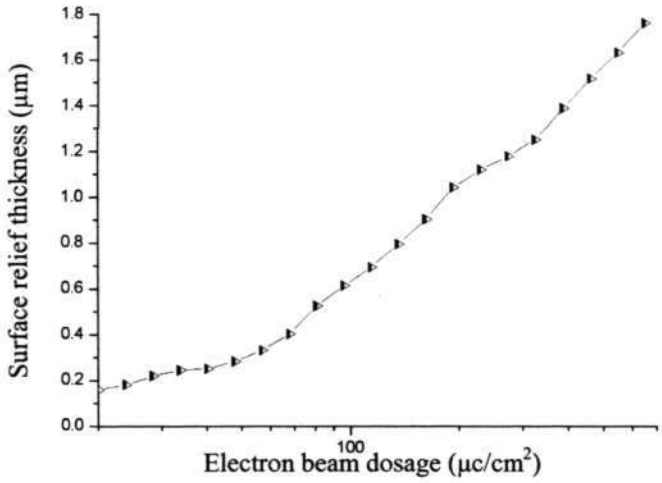

Fig.4-7. Calibration curve of sol-gel surface relief thickness against electron beam dosage.

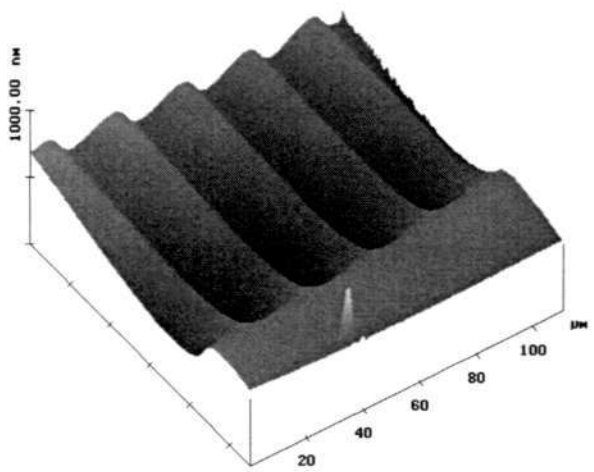

Fig.4-8. Illustration of volume growth phenomenon.

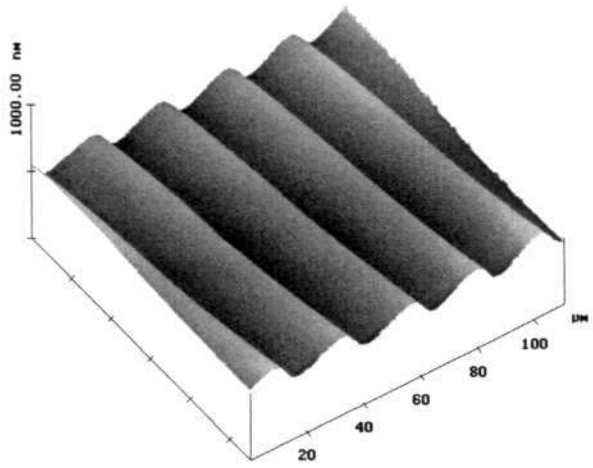

Fig 4-9a. AFM picture of Saw-tooth gratings with a period of 21µm.

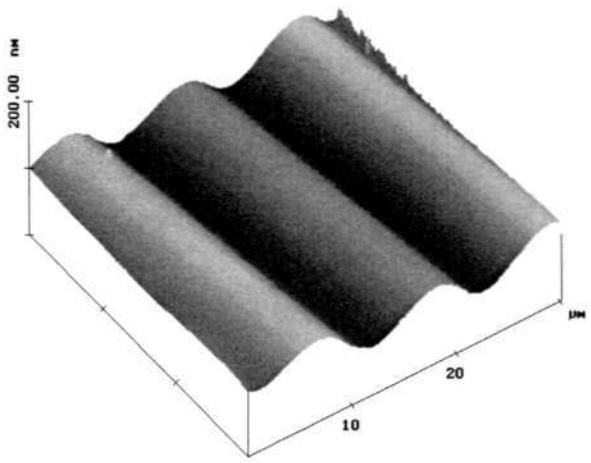

Fig 4-9b. AFM picture of Saw-tooth gratings with a period of 11 µm.

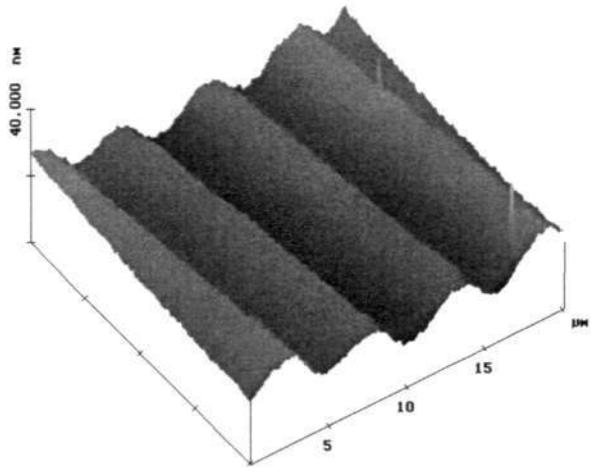

Fig.4-9c. AFM picture of Saw-tooth gratings with a period of 6μm.

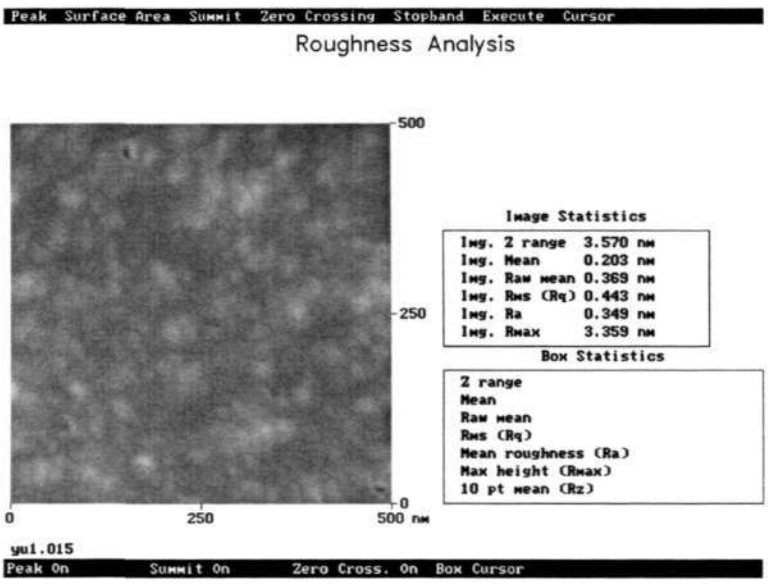

Fig.4-10. Surface roughness in exposed area.

In above fabrication results, the period of the saw-tooth grating is in the scale of 20μm or less. As can be seen, the surface relief thickness of these gratings is very small, less than 200nm. So we can conclude it is more suitable for fabrication of microoptical elements with a large size in self-development sol-gel glass. To demonstrate that grey scale mask technology is more suitable for fabrication of

large size microoptical elements with multilevel structures, a commercialized grey scale mask from Canyon from the Cayon Materials Inc. was used for the calibration. The calibration plate has 100 grey levels and each grey level consists of 3 test strips. Each test strip is located in an area of 204.8μm × 819.2μm size and assigned with one optical density (OD) value. The OD values of the grey levels are determined by,

$$OD = 0.12 + 0.0101 \times i ,$$

where $i = 0,1,2,\cdots,99$. Therefore, the 100 grey levels correspond to optical-density (OD) values ranging from 0.12 to 1.12. For the self-development sol-gel film, each grey level will determine a respective volume growth in the exposed area after UV curing. The UV exposure was implemented by a Q 2001CT UV-mask contact aligner (Quintel Corporation) with a peak emission at 365nm wavelength and an irradiance of 15mW/cm^2.

The material used here undergoes a volume growth effect in the UV exposed areas, and the amount of the growth determined by the OD values in the mask. A schematic diagram of the fabrication technique is shown in Fig.4-6. It is noted that there is an air gap between the sol-gel film and the mask so that there will be enough room for the volume growth in the exposed area. The gap also prevents the mask from touching to the sol-gel material.

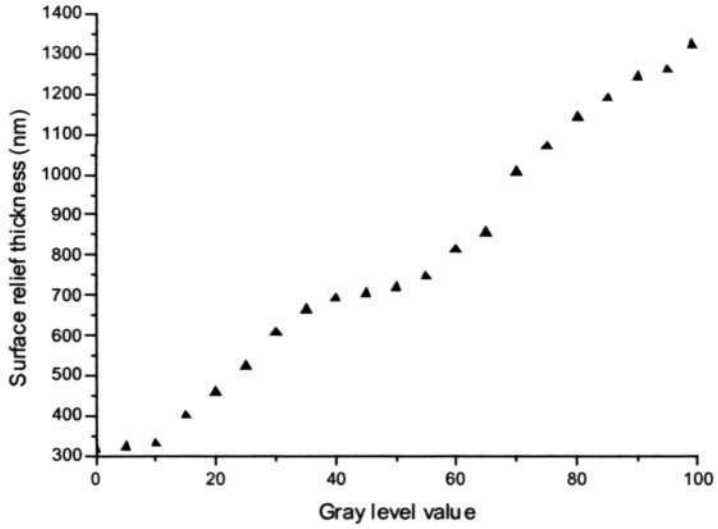

Figure 4-11. Surface relief thickness against grey level value.

In the experiment, various exposure times had been tested using the same grey scale mask and it was found that the optimum exposure time was about 2 min. The sol-gel samples used in this experiment had a thickness of 10μm. Fig.4-11 shows the calibration results with the optimum exposure time. It is seen in the figure that the depth of surface relief has a non-linear response to the optical densities. In addition, the total calibration depth exceeds 1.2 μm in this experiment. Since the sol-gel material has a refractive index about 1.5, it is implied that the volume growth could realise a phase change of 2p in visible light applications.

It should be noted that the minimum depth for grey level one is about 300 nm but not 0. This is because the OD value in this grey level is 0.12 which means that the transmission of light is 76% calculated from the equation

$$OD = \lg(1/T),$$

Where T is the transmission rate of the light.

Based on above calibration results, as an example, we present some results to show the fabrication of blazed gratings as follows. The blazed gratings were designed with 10 grey levels with OD values ranging from 0.12 to 1.12. Fig.4-12 and Fig 4-13 show the surface profile of blazed gratings with a period of 200 μm and 100 μm respectively. It is seen that the gratings have excellent surface smoothness. This is because in the volume growth process, the chemical reactions in the development process based fabrications were omitted. The effective depths of the gratings are 924 nm and 943nm respectively, which are smaller than the maximum depth predicted in the calibration. This is due to the proximity effect of the adjacent points between the maximum and minimum OD values over the grating periods.

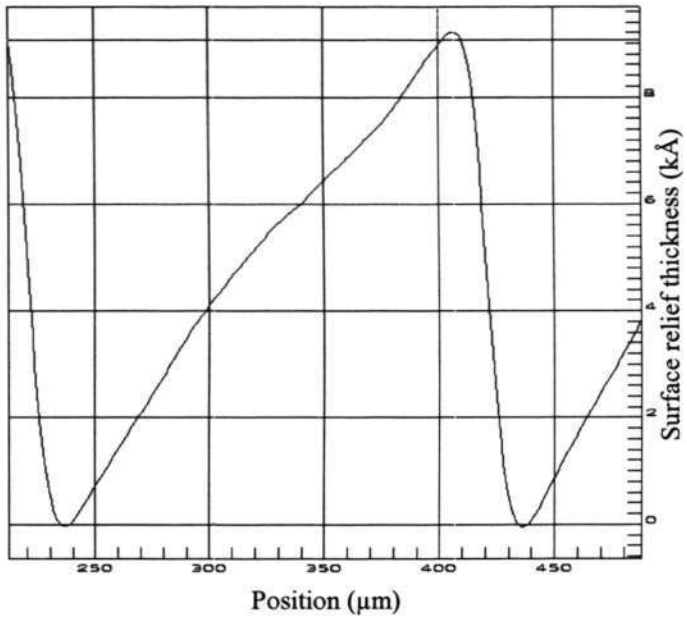

Figure 4-12. Surface profile of blazed gratings with a period of 200μm.

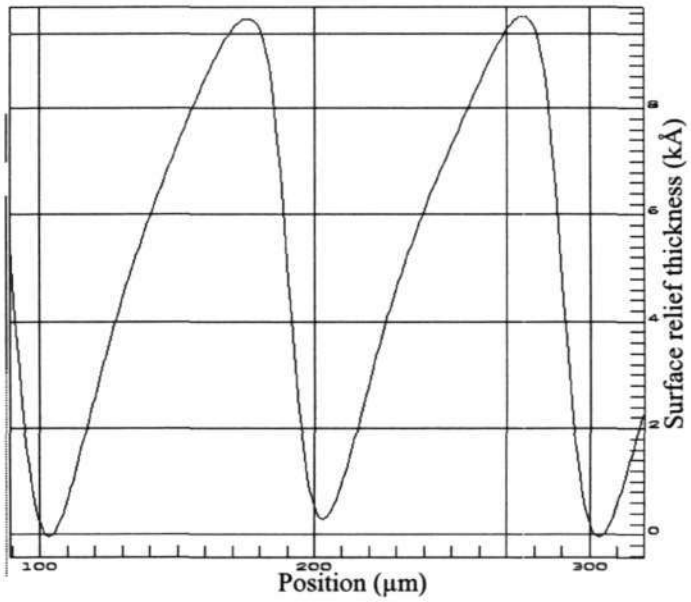

Figure 4-13. Surface profile of blazed gratings with a period of 100μm.

4.3 Fabrication of refractive microlens in self-development photosensitive sol-gel glass by an user defined grey scale mask

In the following, we will demonstrate the fabrication of refractive microlenses with a user defined grey scale mask. Microlens usually have a relative large aperture size, about 100μm. Therefore, one can apply the grey scale mask technique in self-development for fabrication of microlens. Since we will use the grey scale mask to fabricate microlens, to begin with, it is necessary to establish a relationship between the amount of volume growth in the sol-gel glass and the optical density of the grey scales required on the HEBS mask. For this purpose, we have divided the calibration sample into 21 grey scale levels and each sub-sampling area has a dimension of 10μm ×300μm. The grey scale levels were generated by electron beam exposure with a fixed beam current of 93 pA and accelerating voltage of 25 KeV with different exposure time. The electron beam dosage was varied nonlinearly from 20 $\mu C/cm^2$ to 640 $\mu C/cm^2$ in the 21 levels. The n-th level is given by $20\times1.19^{(n-1)}$ ($\mu C/cm^2$), where n is the grey level number. It is noted that the

higher the e-beam dosage, the darker the grey level and the smaller the growth of the volume.

With the user defined grey scale calibration mask, the sol-gel film was characterized to reveal the volume growth response to the optical densities. This step was implemented on a Q 2001CT UV-mask contact aligner (Quintel Corporation) with a peak emission at a 365 nm wavelength and an irradiance of 15 mW/cm^2. After UV exposure, it is seen that the HEBS mask with the user defined optical densities had built the corresponding surface relief heights into the permanent sol-gel glass. Based on the findings of the volume growth response, we need to further establish the relationship between the volume growth and the electron beam dosage that will be used to generate the optical densities. With this relationship, it is only necessary to find out the electron beam dosages for a grey scale mask, whereas the tedious measurement of the optical densities at micrometer resolution can be omitted. In this experiment, we used sol-gel samples that have a thickness of up to 40μm. Figure 4-14 shows the relationship between the surface relief thickness and the electron beam dosage. As the HEBS mask was designed as a light-field mask, which means that the optical densities were only generated within the shape of testing pattern, the measured surface relief thickness represents the height differences between the areas patterned with the grey levels and the outskirts without grey levels. Comparing the height difference between the spot which was incident with the maximum e-beam dosage of 640μc/ cm^2 with the adjacent transparent areas on the HEBS glass, it can be observed from Fig.4-14 that the maximum surface relief thickness produced can be as big as 3.6μm.

To achieve an arbitrary surface profile, one has to define the electron beam dosage exposed to the HEBS glass for each pixel height. For design convenience, the calibration curve is fitted to the following polynomial,

$$Y = -26.38119 + 307.34829 \times X - 46.1826 \times X^2 + 3.55569 \times X^3$$

where Y and X represent the electron beam dosage and the surface relief thickness respectively. Based on this experimental curve, a grey scale mask for a microlens was designed and fabricated in HEBS glass by electron beam lithography (EBL). Figure 4-15 demonstrates a 3-D profile of the microlens fabricated in the self-development photosensitive hybrid sol-gel glass. The surface profile was measured by a laser interferometer (WYKO NT 2000). This microlens has a diameter of 140 μm and a depth of 2.13 μm. It can be seen from the figure that the microlens is sunk into a circular well in the sol-gel film; this is so because the volume growth in the outskirts was maximized by UV exposure without going through grey levels. Figure 4-16 illustrates a comparison of the fabricated two-dimensional microlens surface profile and the ideal original shape. It can be clearly seen that there is excellent agreement between the profiles in the central areas. However, it is noted that there is a larger deviation in the outer area of the microlens, which could produce spherical aberration. Further detailed analysis of spherical aberration was implemented with CodeV software (Optical Research Associates), and the calculated results show that the spherical aberration of the fabricated microlens is approximately two times larger than that of a perfect spherical microlens with the same diameter and sag height. We believe that there are two main reasons why the fabricated surface profile deviated from the theoretical values. The first reason is imperfect fitting of the calibration curve in the lower dose area, as shown in Fig. 4-14. The thickness in this area is less than 500 nm, and it affects the focusing

property of light waves largely through the outer ring zone. The other reason is shrinkage of the film owing to further condensation during postbaking. All these disadvantages can be overcome if we can optimize the various fabrication parameters as a single parameter.

Surface quality is a very important parameter for an optical element. Figure 4-17 shows the surface roughness property measured by an atomic-force microscope in a 500 nm × 500 nm area on the top surface of the fabricated microlens. The root-mean-square value is 1.183 nm, which is just larger than the 1-nm limit that corresponds to 4% reflectance. Thus the resultant microlens surface shows good optical smoothness.

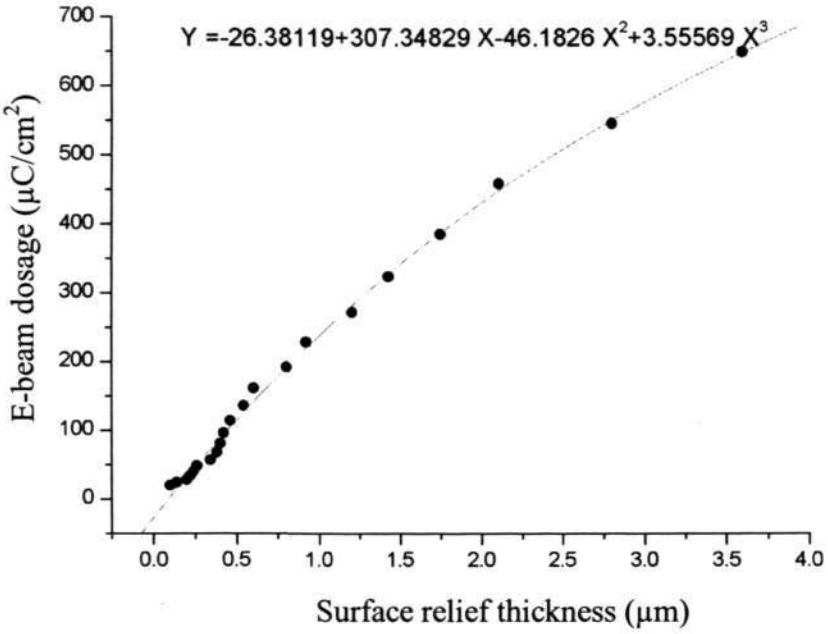

Fig.4-14. Electron beam dosage versus surface relief thickness.

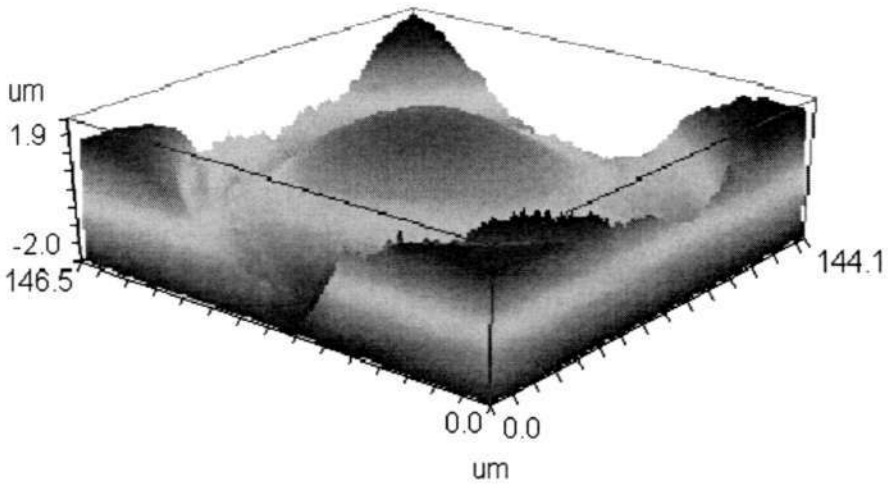

Fig.4-15. 3D profile of the microlens fabricated in self-development sol-gel glass.

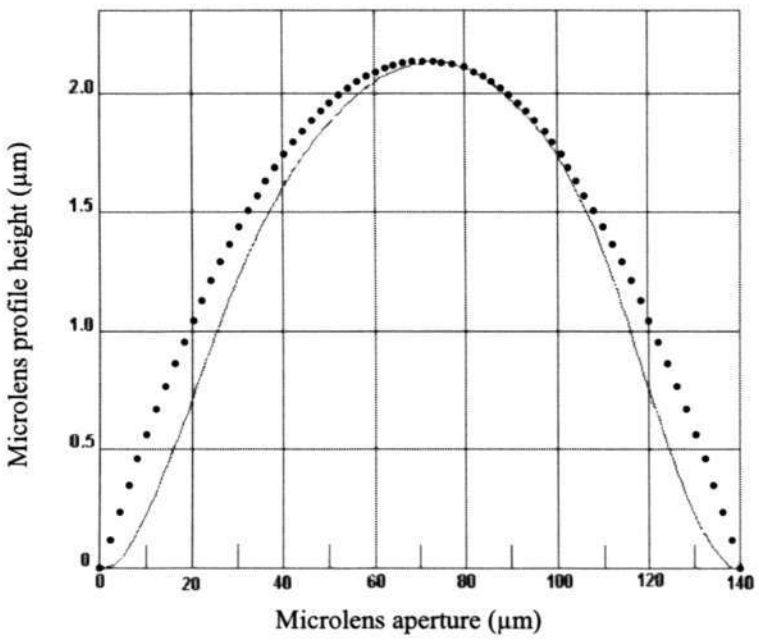

Fig.4-16. 2-D surface profile of the microlens, dotted line and solid line represent the theoretical and measured profile respectively

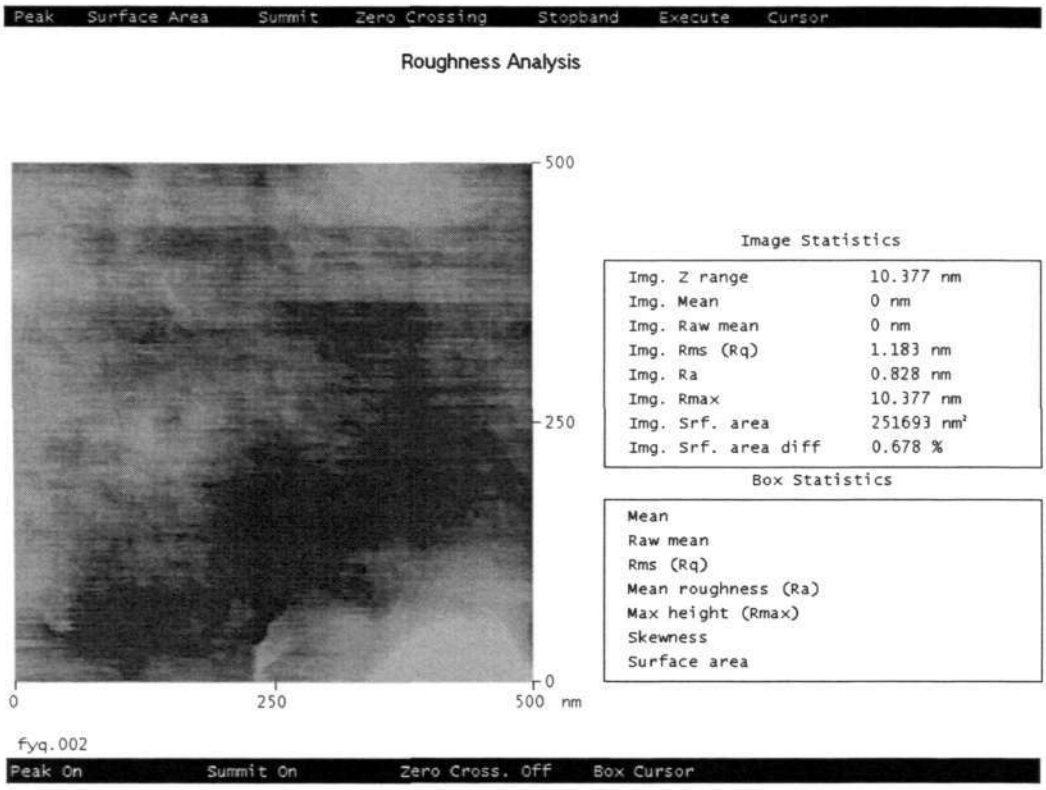

Figure 4-17. Surface roughness measured in the top area of the fabricated microlens.

4.4 Fabrication of microlens in self-development sol-gel glass by using an amplitude mask

As we can see from the previous section, the volume growth of the self-development sol-gel glass can be controlled accurately so that a microlens can be formed. However, this process needs a precise calibration of the relationship between volume growth and the optical density of the grey scale mask. I addition, a grey scale mask is very expensive and not readily available to use.

In this section, we show some results of fabrication of microlens in self-development sol-gel glass by using a binary amplitude mask. With an amplitude mask, we can control the final lens surface profile by controlling the exposure time of the sol-gel glass to UV light precisely. This method can be considered as an

alternative to the fabrication of microlens since it is cost-effective as well as a single step fabrication process. The experiment is the same as that shown in Fig.4-5 except that the grey scale mask was replaced by a binary amplitude mask.

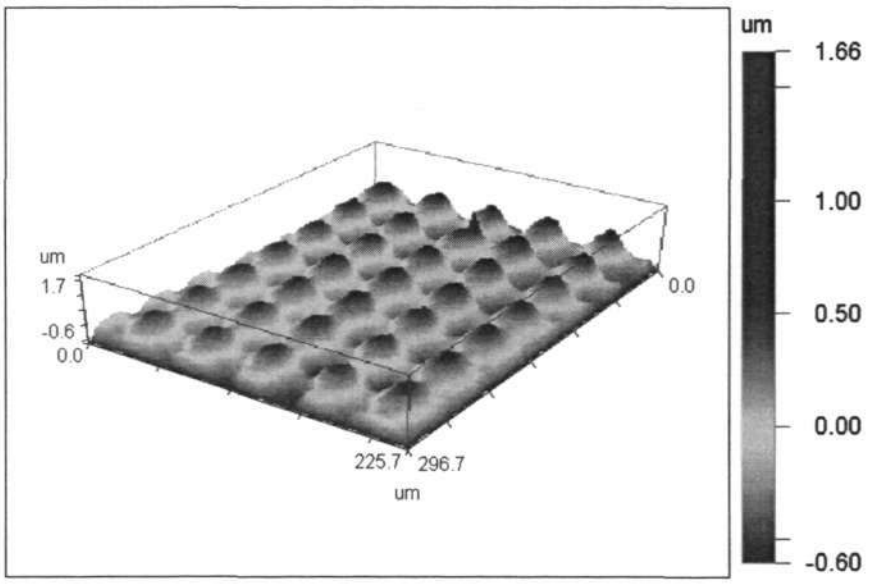

Figure 4-18 shows a microlens array fabricated in self-development sol-gel glass by using a binary amplitude mask. The surface profile was measured by an optical interferometer. The amplitude mask used in this experiment is shown in Figure 4-19.

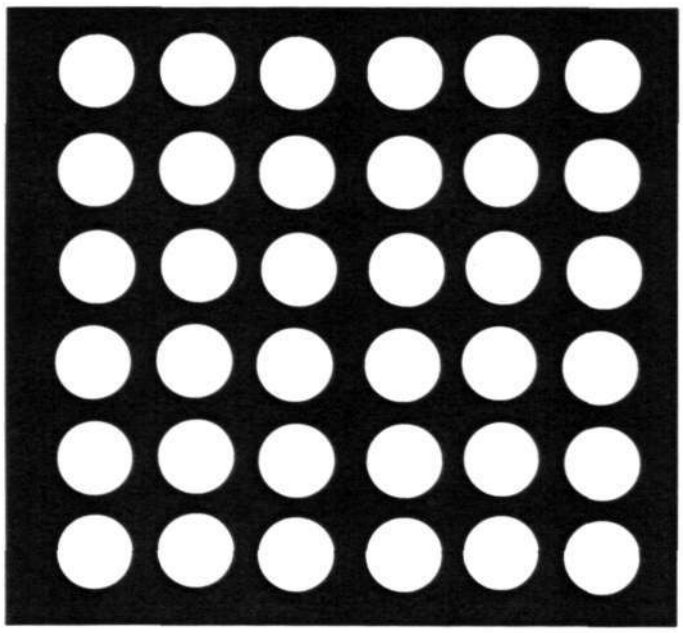

Figure 4-19. The amplitude mask used for fabrication of microlens array in self-development sol-gel glass.

The dark area is coated with chromium to block UV light and the bright area is transparent to allow UV light to pass through.

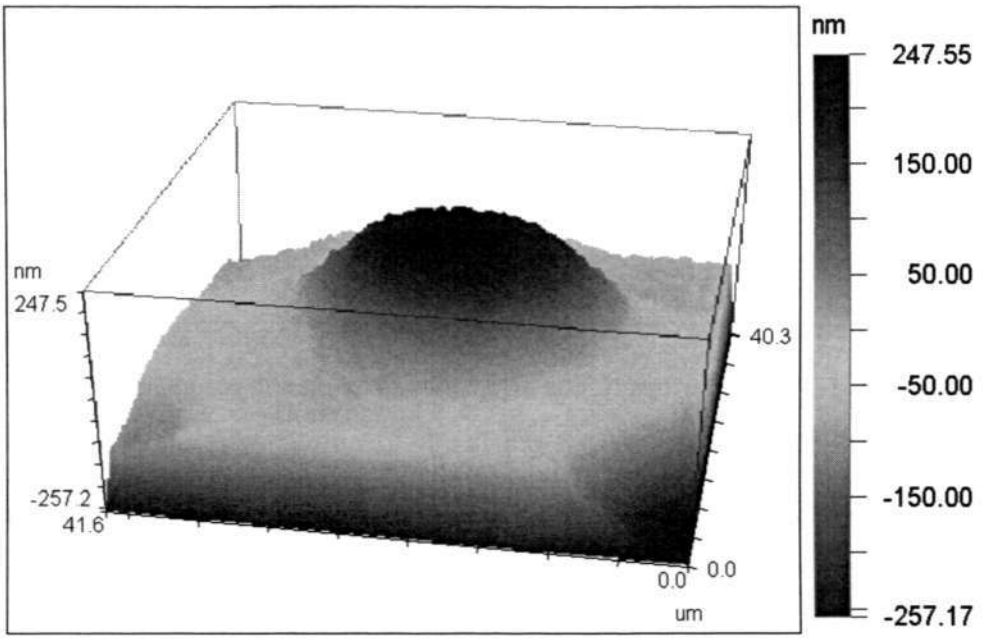

Figure 4-20. 3-dimensional surface profile of a microlens fabricated in sol-gel glass by an amplitude mask.

Figure 4-20 shows one of the microlens fabricated in self-development sol-gel glass with a height of about 500nm. The exposure time is about 22min. It can be seen that this microlens dose not possesses a spherical surface profile. We furthermore found out that a circular cone microlens array can be obtained with this process. Figure 4-21 shows a 3-dimensional profile of a circular cone microlens array. The height of the microlens is about 1.4 μm.

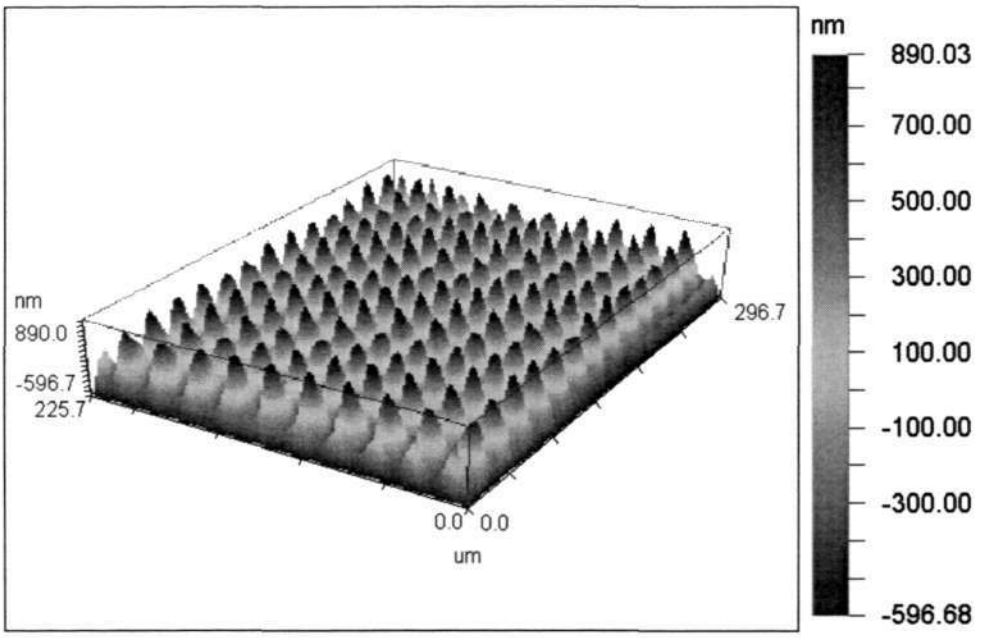

Figure 4-21. A circular microlens array fabricated in sol-gel glass by using an amplitude mask.

Circular cone microlens array has a large object field and can be used for some special applications such as 360° illumination and image processing applications. However, circular cone microlens array is very difficult to fabricate by using traditional photolithography method. Usually, an expensive grey scale mask is used to fabricate such a three dimensional structure. The method that is demonstrated in this work provides us an alternative choice to realize such a complex microstructure. More importantly, it is a simple and cost effective method. A binary mask rather than a grey scale mask is used to produce the cone microlens array. In addition, this is a single step fabrication process as after UV irradiation the cone microlens structure is formed. A development process is not required to reveal the cone microlens structure.

4.5 Discussions and conclusions

We have demonstrated the control of the volume growth of the hybrid sol-gel film by using a grey scale mask. Three gratings with periods of 20 μm, 11μm and 6μm were fabricated. The AFM pictures of the fabricated gratings stated that the grating depth has a positive relationship with grating period and the surface roughness has an opposite relationship with grating period. Thus, we can conclude that this self-development photosensitive hybrid sol-gel glass is very suitable for the fabrication of large period gratings and large dimensional optical elements with good surface smoothness by using a grey scale mask.

To demonstrate the fabrication of large size micro-optical elements with multilevel structures in self-development photosensitive hybrid sol-gel glass, a commercialized HEBS grey scale mask was employed and a 10μm film thickness sol-gel sample was used. The calibration results showed that the maximum surface relief thickness induced by the UV light exceeds 1.3 μm, which implies that a 2p phase delay in the visible wavelength has been realized. As an example, two blazed gratings with period of 200 μm and 100 μm, and depth of more than 900nm were fabricated. Similar to the reflowing technique, due to the absence of chemical treatment in the process, the preliminary results showed that the self-development technique has an advantage over the development process based technology in excellent surface smoothness.

Furthermore, we have demonstrated the fabrication of microlens in self-development photosensitive hybrid sol-gel glass by using a user defined grey scale high-energy beam-sensitive mask. The surface relief thickness of the sol-gel film is related to the electron beam induced optical densities in an HEBS grey scale mask.

With the calibrated results, a grey scale mask for microlens was fabricated and a microlens with a 140 μm diameter and a 2.13 μm sag height was obtained. The measured surface profile has been found to be in good agreement with the desired profile. This method possesses a great potential of producing high quality micro-optical elements with good surface smoothness.

Finally, we also demonstrated that it is possible to fabricate microlens in self-development sol-gel glass by using an amplitude mask. A circular microlens array with a sag height of more than 1μm was fabricated successfully.

Chapter 5. Mass fabrication of microlens arrays with high numerical aperture in hybrid sol-gel glass by using soft-lithography method

With the fast development of photonics technology, diffractive optics and micro-optics play a more and more important role in photonics application such as optics communications. Microlenses and microlens arrays as microoptical elements are key elements in many microoptical systems for optical coupling and optical interconnection applications. When microlens is used as a coupler, it can improve the coupling efficiency from laser diode to optical fibre, optical fibre to optical fibre, optical fibre to waveguide, optical fibre to detector and so on [35-55]. Many fabrication methods have been proposed for the fabrication of microoptical elements and microlenses [56-72]. These methods can be classified into two types. One is using traditionally microlithographic method to fabricate microoptical elements in photoresist or polymer and then transferring the pattern into substrate of glass or silicon by dry etching method. The other is using a pulse laser beam or focused ion beam to blaze the glass or silicon material directly to form a microlens structure. The disadvantages of these two methods are that they are time consuming and too expensive since they require special equipment. Thus, it is very attractive to develop a low cost and fast fabrication method.

In this chapter, we first give a brief review of soft-lithography method and then introduce this method into mass fabrication of microlens array in photosensitive hybrid sol-gel glass. The soft-lithography method involves three main steps. The first step is fabrication of a microoptical element master; the second step involves

the forming of a polydimethylsiloxane (PDMS) replica; and the last step requires the transferring of the expected microoptical structure into sol-gel glass.

5.1 Overview of the mass fabrication method by using a PDMS replica

To introduce the hybrid sol-gel material to commercial applications in industry, it is necessary to develop a simple and reliable fabrication technique so that the advantages of the sol-gel materials can be realized significantly as a low-cost and high-volume solution. Several methods have been used for mass fabrication of microlenses including hot pressing, injection molding and polydimethylsiloxane PDMS replica. In these methods, the microlenses were built in polymer materials, where the polymers were used as a transitional patterning layer for transferring the structures into silica or quartz substrates by dry etching. It is known that due to the etching process, both surface profile fidelity and surface smoothness control are difficult tasks. The presence of these process drawbacks makes the dry etching technique unsuitable for the mass production of microlenses. As for the method which uses a PDMS replica, the cylindrical photoresist island was firstly transferred into sol-gel film and it was followed by an annealing process to produce microlenses. However, reflowing sol-gel is a high temperature process and the reflowing temperature and time should be controlled accurately.

The fabrication method by using a PDMS replica is called soft-lithography method. In this method, an elastomeric replica or mold, PDMS replica, is used to transfer the pattern or structure from a master. This method, firstly developed by Y.Xia and G.Whiteside, includes microcontact printing, replica molding, microtransfer molding, micromolding in capillaries and solvent-assisted micromolding [73-80]

and these applications have since been employed by the developers in the chemical and biology fields. In all these cases, an elastomeric stamp or mold is used to transfer the pattern to the substrate rather than the rigid inorganic materials that is commonly used in microfabrication. The most important advantage of soft-lithography method is that it is not necessary to use a rigid master. Instead, a soft master such as a patterned photoresist or polymer sample can be used as a master directly. In addition, after we obtain a PDMS replica, it can be thrown away after using several times since it is very fast (several hours) and convenient to make a PDMS replica. Moreover, soft-lithography requires remarkable little capital investment and can be implemented in a very simple way. It can be carried out in the ambient laboratory environment and will not be subjected to the limitations set by optical diffraction and optical transparency. It provides alternative routes for fabrication structures with a feature size in the scale of smaller than 100nm without the need for advanced lithographic techniques. It also offers access to new types of surfaces, optical structures, sensors, prototype devices, and systems that could be difficult to fabricate by photolithographic procedures.

As discussed in our previous work, the sol-gel material has demonstrated its advantage of being used in a single development step fabrication [33, 35] as well as single self-volume growth step fabrication [36]. However, in these reports, the total height of the fabricated micro-optical elements was limited by the relative thickness that was achieved in the development and volume growth process respectively. In the past, due to the UV photosensitive response of the sol-gel material, its thickness was limited to a few microns in many cases.

To overcome the difficulties for fabrication of thick micro-optical elements in the

sol-gel material, in this section, we introduce the application of the PDMS replica technique in the sol-gel fabrication process. In this work, a master copy of microlens array in photoresist was firstly formed using a reflowing technique. The PDMS was then spun onto the master and cured to get a replica of the microlens array. Next the PDMS replica was impressed onto the thick photosensitive sol-gel glass to transfer the microlens array and the sol-gel glass was densified by UV curing. Since the reflowing process in photoresist has been well developed for reasonable high thickness, the proposed PDMS replica process has allowed us to increase the thickness of the sol-gel glass significantly.

5.2 Fabrication of microlens by using soft-lithography method

The fabrication processes involve three main steps, which are illustrated in Fig.5-1 schematically. The first step was based on the reflowing process for the fabrication of master microlens in photoresist. After the establishment of the microlenses in the photoresist, the second step was implemented simply by a PDMS replication process. Finally, the microlenses in sol-gel glass was achieved by impressing the PDMS replicated structures in the sol-gel material, followed by a UV cure to solidify the structures in the sol-gel glass. The process details are listed as follows:

In the first step, according to the matured reflowing technique as described in [37-38], an AZ5214 positive photoresist was used and melted at a temperature of 190^0C. Once the microlenses were obtained, the PDMS was spun onto the microlens array and then cured at a temperature of 100^oC for 1 hour or room temperature for 24 hours. The cured PDMS replica is elastic, hydrophobic and can be peeled off from the microlens master. Since the PDMS replica is hydrophobic, it is difficult for us to spin the sol solution onto it directly. Alternatively, we pressed the PDMS replica

onto the soft photosensitive sol-gel film. The detail of the preparation of the photosensitive sol solution can be found in previous section. Since the cured PDMS is optically transparent, the photosensitive sol-gel film impressed with the PDMS replica can be exposed to UV light through the PDMS replica. The UV exposure was implemented by a Q 2001CT UV-mask contact aligner (Quintel Corporation) with a peak emission at 365nm wavelength and an irradiance of 15mW/cm^2. The exposure time was 30min so that the sol-gel film can be polymerised and stabilized completely. After the UV curing, the PDMS replica was peeled off from the sol-gel microlens. It is observed that the resulted microlens was hard enough such that the postbake process may not be necessary.

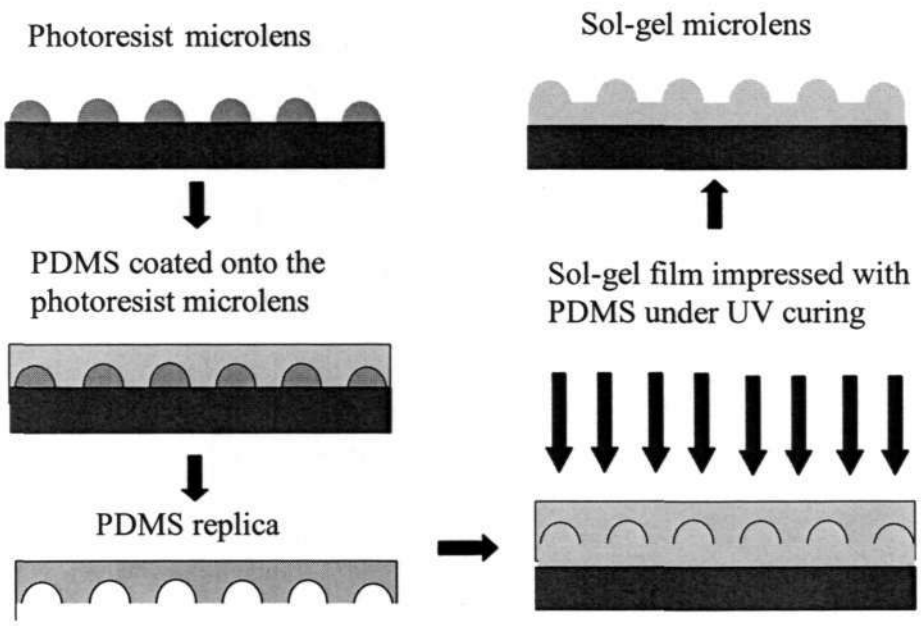

Fig.5-1. Flowchart of the microlens fabrication process.

By using the above method, microlens arrays with a numerical aperture ranging from 0.3 to 0.5 were successfully fabricated. Figure 5-2 shows the SEM pictures of fabricated microlens array.

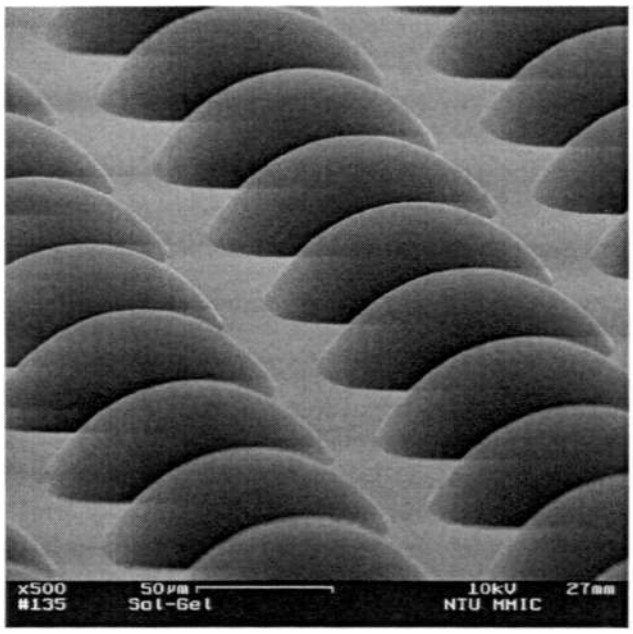

Fig.5-2a.

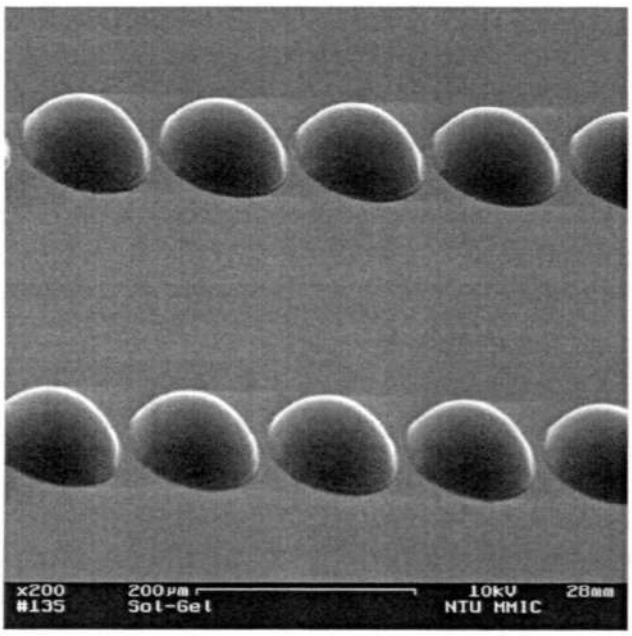

Fig.5-2b

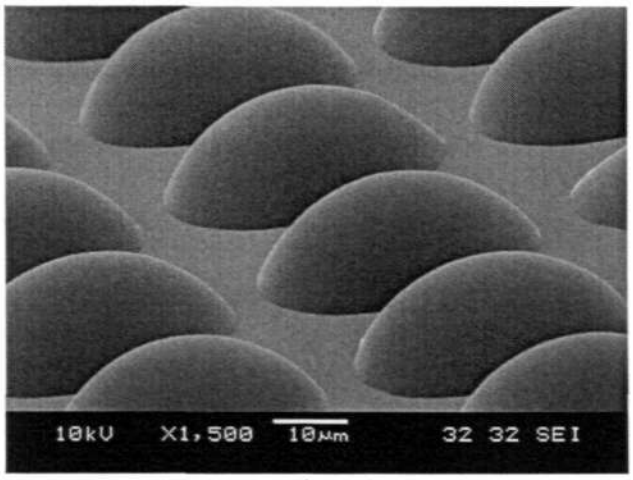

Fig.5-2c

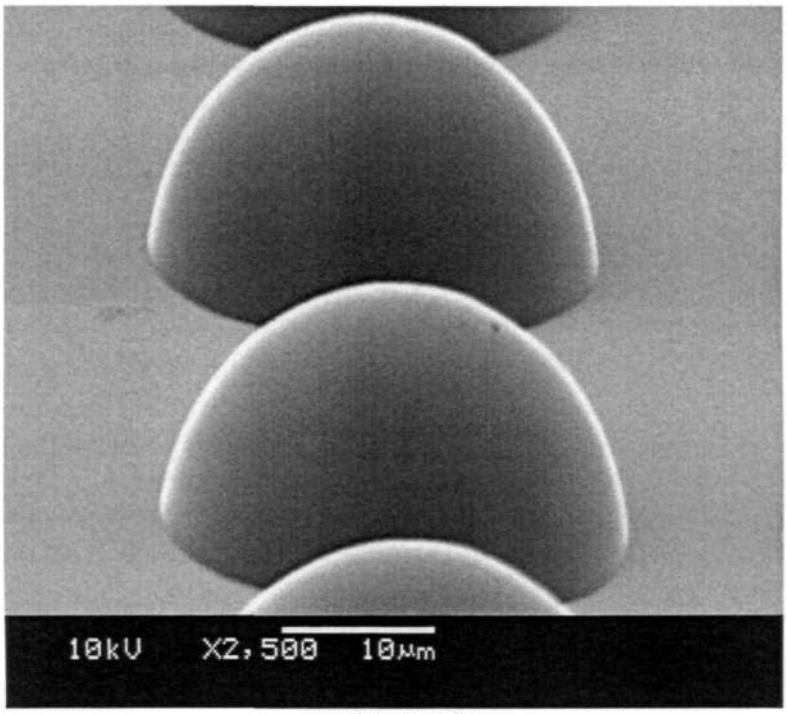

Fig.5-2d

Figure 5-2. Fabricated sol-gel microlens array with a numerical aperture of 0.3 (Fig.2a), 0.44 (Fig.2b), 0.46 (Fig.2c) and 0.5 (Fig.2d).

To demonstrate the fidelity of the fabrication process, we compare the surface profile of the photoresist microlens with that of the sol-gel microlens. Figure 5-3 shows SEM picture and two-dimensional surface profile of a microlens with a diameter greater than 200 μm, built in photoresist and sol-gel material respectively.

The pictures in the left column show the photoresist microlenses and the pictures in the right column show the sol-gel microlenses. It is seen from Figure 5-3 that the microlenses sag heights are 26.19 μm and 26.15 μm for the photoresist microlens and sol-gel microlens respectively, which gives a vertical replication error of 40 nm (0.15%) compared to the sag height of the photoresist microlens. The microlens apertures are 233.5 μm and 232.4 μm for photoresist microlens and sol-gel microlens respectively, which gives a lateral replication error of 1.1 μm (0.47%) compared to the photoresist microlens aperture. The small replication error (less than 1%) implied that the sol-gel material has small shrinkage after UV curing and the replication method shows excellent replication fidelity.

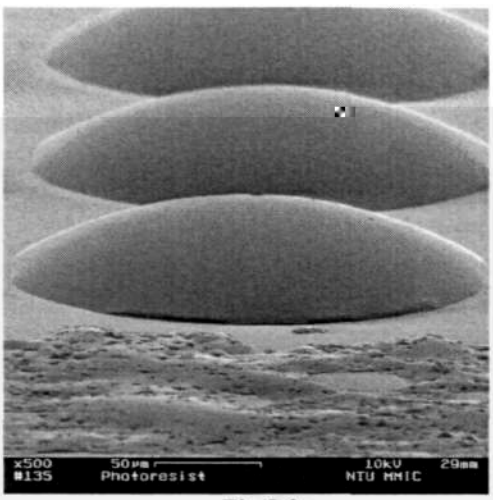

Fig.5-3a

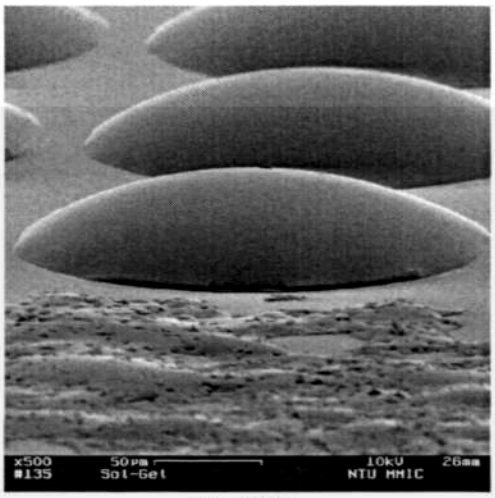

Fig.5-3b

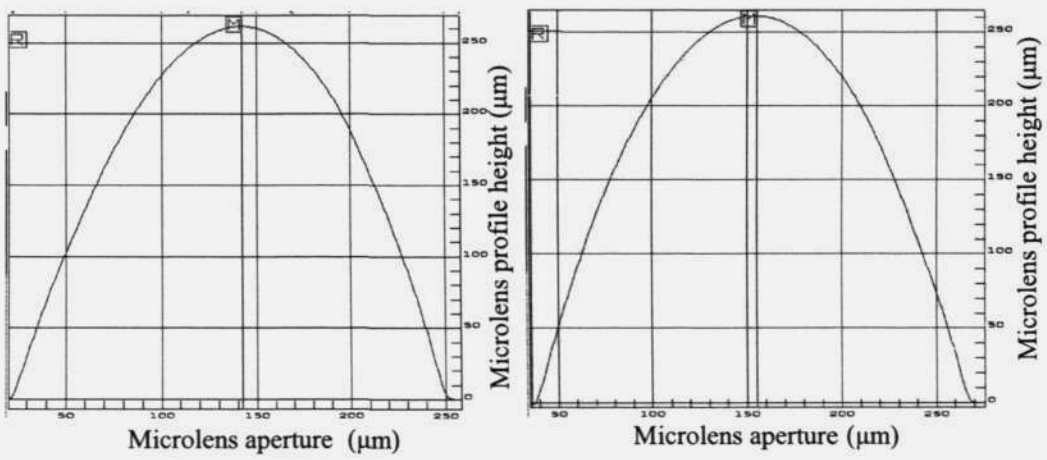

Fig.5-3c

Figure 5-3. SEM pictures of microlenses fabricated in photoresist (Fig.5-3a) and sol-gel glass (Fig.5-3b) and their two-dimensional surface profile Fig.5-3c (Left one for photoresist microlens and right one for sol-gel microlens).

We have found out that smaller feature size of less than 10nm can also be replicated into sol-gel material by this method. We demonstrated this by a simple experiment and the result is shown in Figure 5-4. In Figure 5-4, a rather rough surface with particles in 10nm scale or smaller is fabricated by E-beam lithography in PMMA and replicated in sol-gel glass. It can be seen that all the particles including lines of about 100nm, have been replicated from PMMA into sol-gel exactly. This experiment shows that this method has a great potential for fabrication of sub-10nm

structures or even smaller feature size structures. We are now trying to explore its use for replication of nanooptical elements.

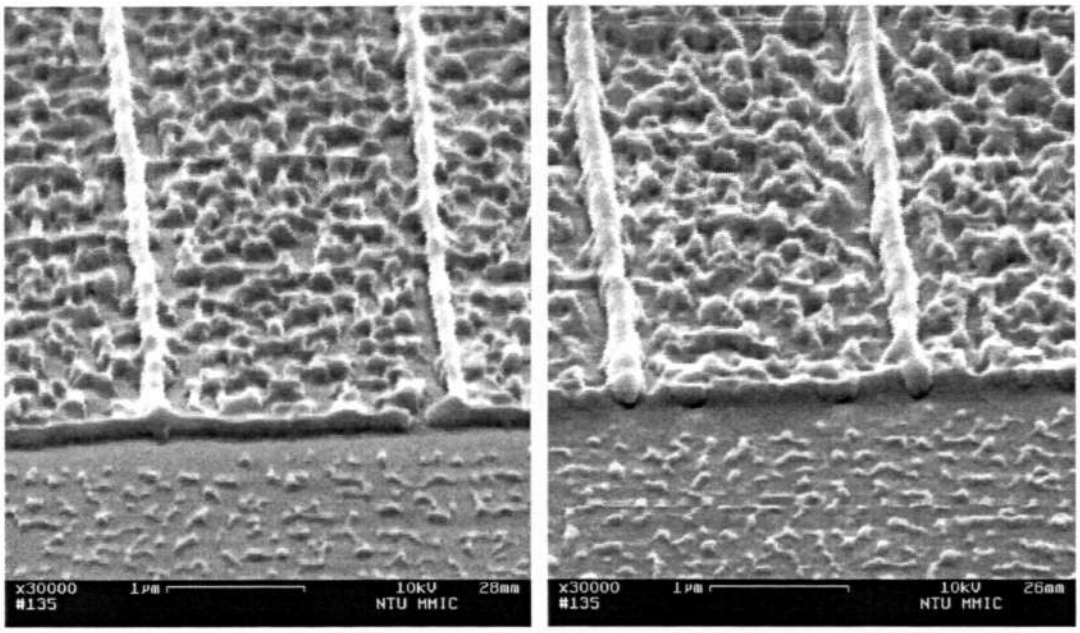

Figure 5-4. SEM pictures of a rough surface in PMMA (left) and in Sol-gel glass (right) respectively.

5.3. Conclusions

In this chapter, we developed a novel method based on soft-lithography to fabricate microlens array in hybrid sol-gel glass. It is seen that this method is fast and cost effective. More importantly, this approach enables us to fabricate microlens with a high numerical aperture of up to 0.5.

Chapter 6. Characterization of sol-gel microlens

Although microlens array has attracted many attentions and various fabrication methods have been proposed and developed, the characterization method of sol-gel microlens array still has many rooms for development. Many authors have done much work to characterize microlens [81-89]. In this chapter, we try to characterize the sol-gel microlens fabricated by soft-lithography. The main optical properties we try to measure include focal length, point spread function and modulation transfer function, which are sufficient to give an accurate evaluation of a microlens about its imaging quality.

6.1. Focal length

The focal length of a microlens is very small, usually in the sub-millimeter scale. Generally, for a fixed aperture of microlens, the higher the numerical aperture, the shorter the focal length. For sol-gel microlens used for fibre coupling, the diameter is about 120μm and the numerical aperture is no less than 0.3, thus the focal length is below 200μm. For such a short focal length, it is difficult to be tested by Nodal Slide Bench, which is widely used in optical shop testing [90]. An alternative is to use Twyman-Green interferometer that was invented and patented by F.Twyman and A.Green in 1916. Initially, Twyman-Green interferometer was used for testing of prisms and microscope objective, but recently, it has been frequently used for testing of microlenses. There are also other methods available to test the focal length of microlens, for example using a confocal microscope, grating interferometric method and so on [91, 87]. However, these two methods are difficult to implement. To measure microlens focal length by using confocal microscope, an ultra-precision motor stage is required and for the grating

interfeometirc the data process is very complicated. In comparison, it is very easy and convenient to test the focal length of microlens using the Twyman-Green interferometer.

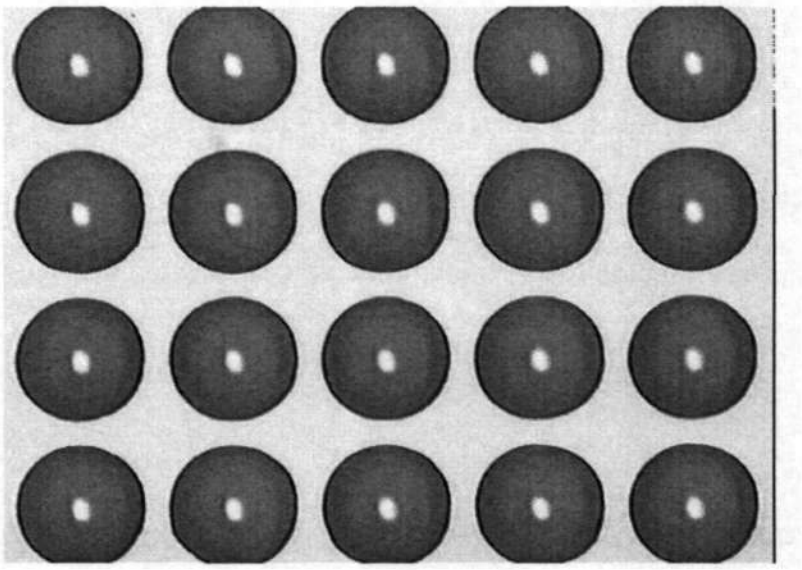

Fig.6-1. Picture of a sol-gel microlens array with a pitch of 125μm imaged by a 10× microscope.

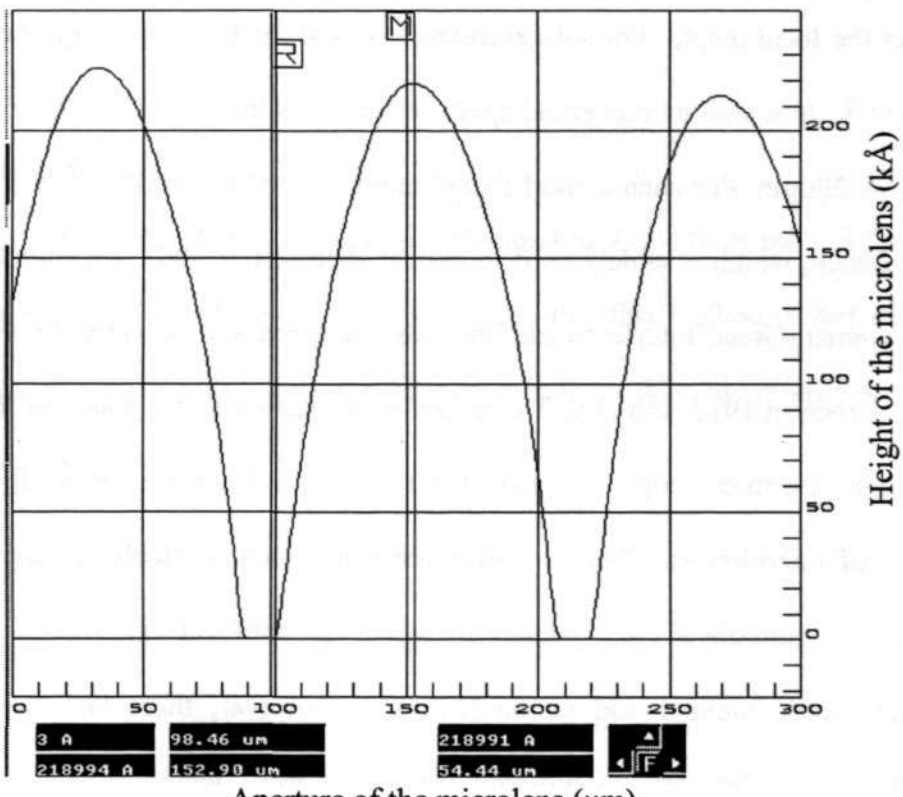

Fig.6-2. Surface profile of the microlens array measured by a surface profiler.

Fig.6-1 shows the sol-gel microlens imaged by a 10× microscope to be tested. This microlens array has a pitch of 125 μm. Fig.6-2 shows the surface profile of the microlens measured by a Dektak surface profiler. It is seen from the figure that the microlens has a diameter of 120 μm and a sag height of 22 μm. From the measurement results we can get a rough idea about the focal length and numerical aperture of the microlens by using the following equation,

$$f = 2 \quad \frac{(D/2)^2 + h^2}{2h}$$
$$NA = \frac{D/2}{f} \tag{6-1}$$

where f is the focal length, D is the diameter, h is the sag height and NA is the numerical aperture of the microlens. By substituting the measured value of the diameter and sag height, the focal length and numerical aperture calculated is 160μm and 0.34 respectively.

Fig.6-3 shows the optical setup and layout of optical path of the Twyman-Green interferometer used for characterization of the focal length of microlens. To describe the working principle briefly, a laser beam with a wavelength of 633nm is collimated and splited by a beam splitter into two parts, where one is the testing beam and the other is the reference beam. The testing beam penetrates through Lens 2 and the microlens array and then gets reflected by mirror 2 to interfere with the reference beam reflected by mirror 1. The interference fringes are captured by a CCD camera and displayed in a computer. The determination of the focal length by using Twyman-Green is based on the principle as explained by Fig.6-4. In Fig.6-4a, the focal spot of the microlens and the focal spot of lens 2 are in the same position such that the testing beam is reflected by mirror 2 and recollimated by microlens. And then the collimating testing beam is deflected by beam splitter and meets with

the reference beam on the camera screen. Since these two beams have the same wavefront curvature, they will interfere and the interference fringes displayed on the computer screen should be straight lines with the same period as shown in Fig.6-5. At this time, we should record the position of lens 2 as P1. Next lens 2 is then moved axially towards the microlens. When the focal spot of lens 2 impinges onto the microlens vertex as shown in Fig 6-4b, the testing beam is recollimated again so that the interference fringes is again displayed as black and white straight lines. The position P2 of the lens 2 is recorded again. Clearly, the distance between P2 and P1 should be the focal length of the microlens.

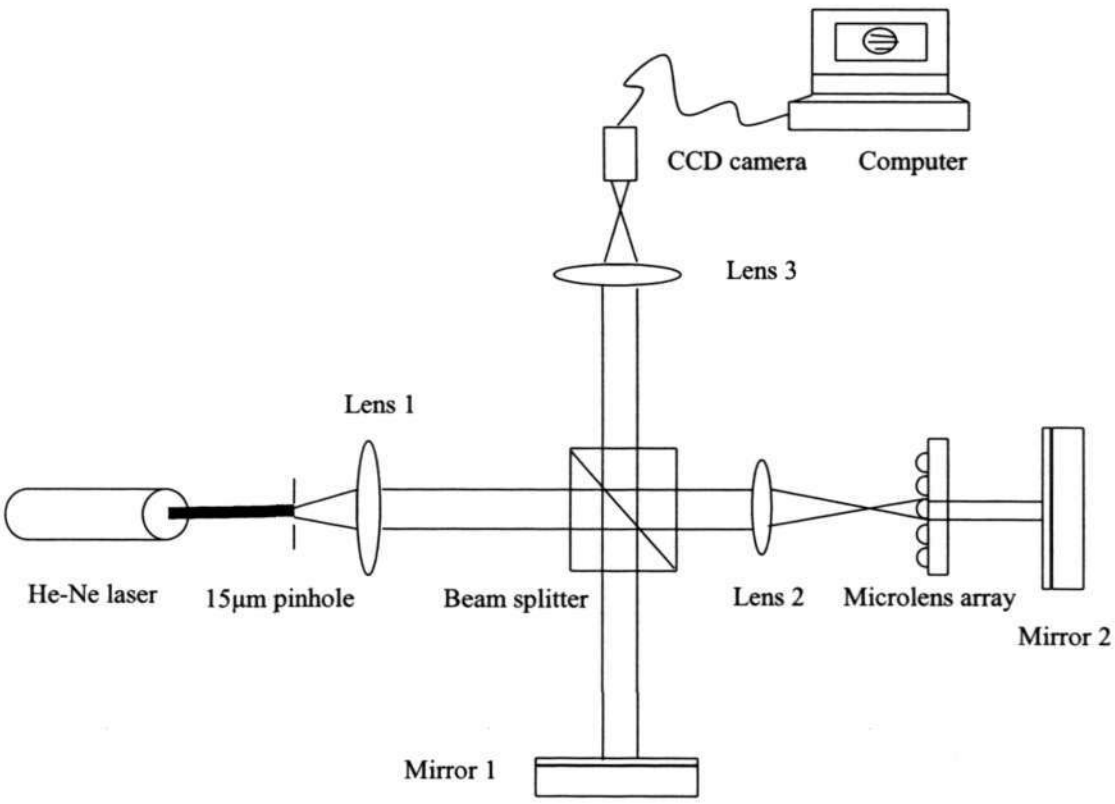

Fig.6-3. Twyman-Green interferometer used for focal length measurement for microlenses.

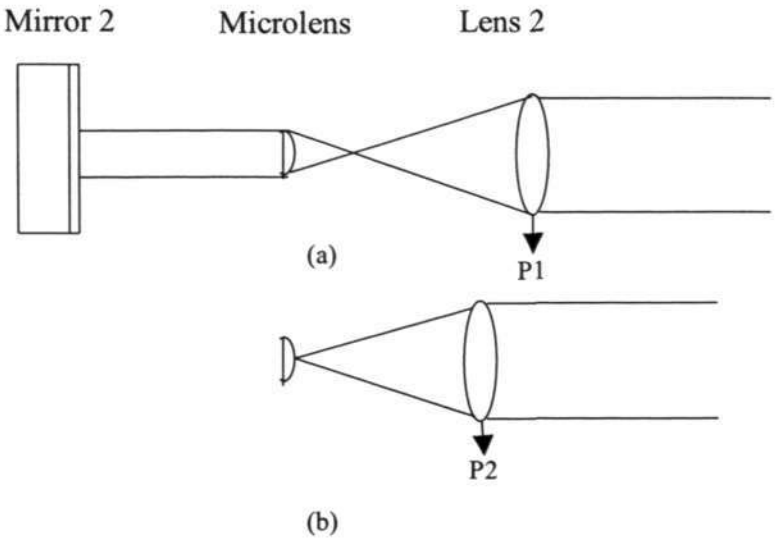

Fig.6-4. Principle for focal length measurement for microlenses.

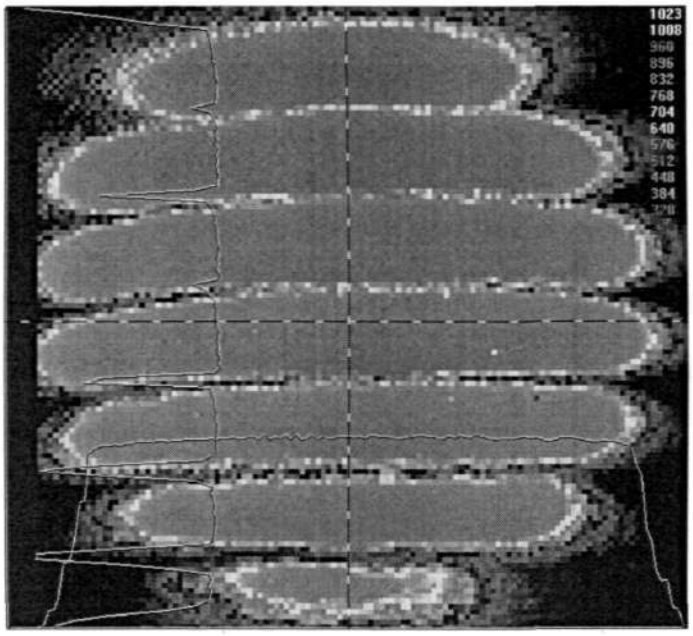

Fig.6-5. Interference fringes.

By using above method, the focal length of a microlens with a diameter of 110 μm and a sag height of 22 μm was measured. The movement of the lens 2 is implemented by mounting it onto a 5-axis precision stage that has a resolution of 10 μm. The measured focal length is 126 ±10 μm. However, compared with the focal

length of 159.5μm calculated by using the diameter and sag height that were measured by a Dektak surface profiler, these two values have a large discrimination and the value measured by optical method is smaller than that predicted by surface profiler. As the optical method performed by the Tywman-Green interferometer is relatively an accurate method, we can conclude that the geometrical parameters measured by surface profiler is not so reliable. In fact, as the microlens has a small diameter of 110 μm, the stylus of surface profiler may not always scan through the center of the microlens. This implies that the measured sag height is likely to be smaller than the real one. Thus, the focal length calculated by this smaller sag height will be larger than the real focal length. This explains well why the focal length measured by the optical method is smaller than that predicted by surface profiler.

6.2. Point spread function

To test the imaging quality of an optical system, the most direct method is to measure its point spread function (PSF). PSF is defined as the intensity distribution in image plane that is transformed by an optical system from a point object in infinite distance. The following formula is used to compute PSF of an optical system [92],

$$I(\xi,\eta) = A\int_{-\infty}^{+\infty}\int \delta(x-x_0, y-y_0)P(x,y;\xi,\eta)d_x d_y \qquad (6\text{-}2)$$

Where $P(x,y;\xi,\eta)$ is denoted as PSF, $\delta(x-x_0, y-y_0)$ is Dirac delta function centered at x_0 and y_0, A is the irradiance of point object. By evaluating above equation, we can get,

$$I(\xi,\eta) = AP(x_0, y_0;\xi,\eta) \qquad (6\text{-}3)$$

It can be seen from equation (6-3) that the intensity distribution in image plane produced by a point source is proportional to PSF. For a microlens with a circular aperture, PSF is proportional to the well know Airy disc distribution as shown by the following equation [93],

$$\frac{I}{I_0} = \left[\frac{2J_1(kr\rho / z)}{kr\rho / z}\right]^2 \tag{6-4}$$

Where J_1 is the first order Bessel function, $k = \frac{2\pi}{\lambda}$ is wavenumber, r is the radius of microlens, $\rho = \left(\xi^2 + \eta^2\right)$ is the radial cooridinate in the image plane and z is the distance from the microlens to image plane.

PSF can be measured by imaging the focal spot of the microlens, produced by a plane wave incident on it. A plane wave can be considered as a point source from infinity.

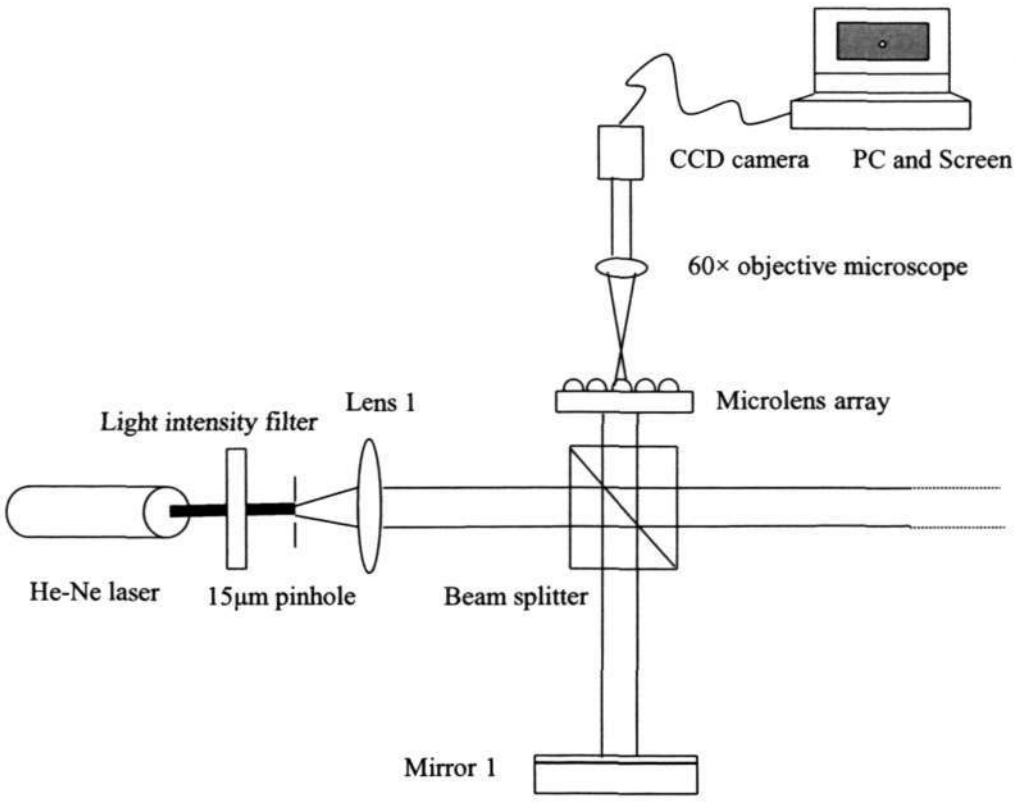

Fig.6-6. Optical setup for point spread function (PSF) measurement for microlenses.

In our experiment, we measure the PSF of the microlens by a slight modification of the Twyman-Green interferometer optical setup. The details of the optical setup for measurement of PSF is shown in Fig.6-6. Since we only need a plane wave that is collimated by the filter and lens 1, we removed mirror 2 and used the beam reflected from Mirror 1. The collimated plane wave incidents onto the microlens array will produced an array of focal spots in the focal plane. Since the focal spot is very small (usually in the several micron meter scale), a microscope with a high amplification is required to image the focal spot of the microlens. In our experiment, we use a microscope with an amplification of 60× and numerical aperture of 0.86. Since the microlens' numerical aperture is about 0.3, this microscope is good enough to image the focal spot produced by the microlens. It is noted that the microscope is attached onto the front of the CCD camera directly to eliminate the

alignment between them and this procedure is also convenient as the experiment can be implemented in day light environment. In addition, a light intensity filter is needed when imaging the focal spot of the microlens. This is because the optical intensity is encircled on a very small spot and thus the light intensity is too high to be sensed by the CCD camera.

Another very important factor is that we must calibrate the real size of a pixel of the image captured by the CCD camera. This procedure is done by imaging an amplitude binary grating that is patterned in a chromium coated glass plate. A grating having a pitch of 6μm was imaged by the CCD camera and saved as a bitmap picture. Fig.6-7 shows the picture of a 6 μm grating. The calibration results showed that one pixel of the image represents 0.176 μm. The reason why the image is not very clear is because the optical table being not stable, induces the vibration of the optical setup always exists. As shown clearly in Fig.6-7, the grating has a spread trace caused by the vibration of the optical setup.

To image the grating, the microlens array in the optical setup shown in Fig.6-6 is replaced by a grating plate. After the calibration is finished, the grating plate is removed and the microlens array is inserted into the beam path. By moving the microlens' position and monitoring the focal spot displayed on the screen, the PSF of the microlens can be captured at the point when the focal spot has a maximum intensity. The movement of the microlens is controlled by mounting it onto a 5-axis precision stage. The intensity of the focal spot is monitored by the CCD camera that has the function to display the real time intensity of the captured beam spot.

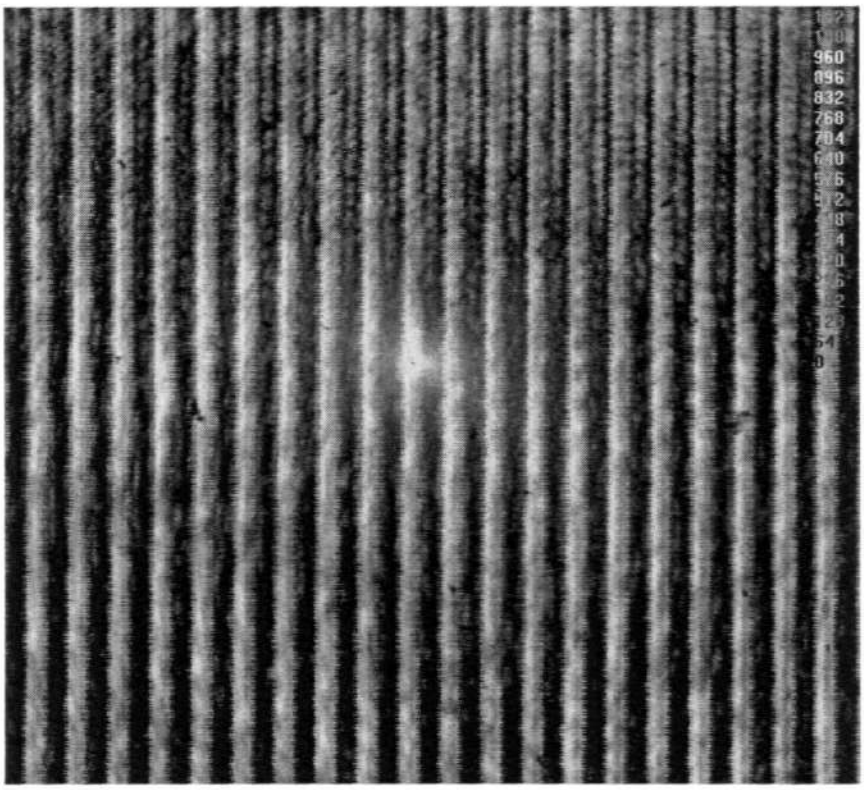

Fig.6-7. A 6μm-period grating imaged by a CCD camera that is used for calibration of a pixel size in image plane.

Figure 6-8 shows the PSF of the microlens with a diameter of 110μm and a sag height of 22 μm. Fig.6-8a shows the image of PSF captured by CCD camera and Fig.6-8b shows the section profile. It can be seen from Fig.6-8b that the intensity of outer ring is very low compared to the center peak. It should noted that since the picture in Fig.6-8 is not the same scale as Fig.6-7, one cannot compare the two figures pictorially to obtain the real size of the PSF. An accurate derivation of the real size of PSF is obtained by analyzing the original pictures captured by CCD camera. Through calibration of the image, we know that one pixel represents 0.176μm, so by analyzing the PSF image we found that the diameter of the PSF's first ring is 2.8 μm. Comparing with the diffraction limited of 1.8 μm, shown in Fig.6-9, the measured value is reasonable although it is slightly larger.

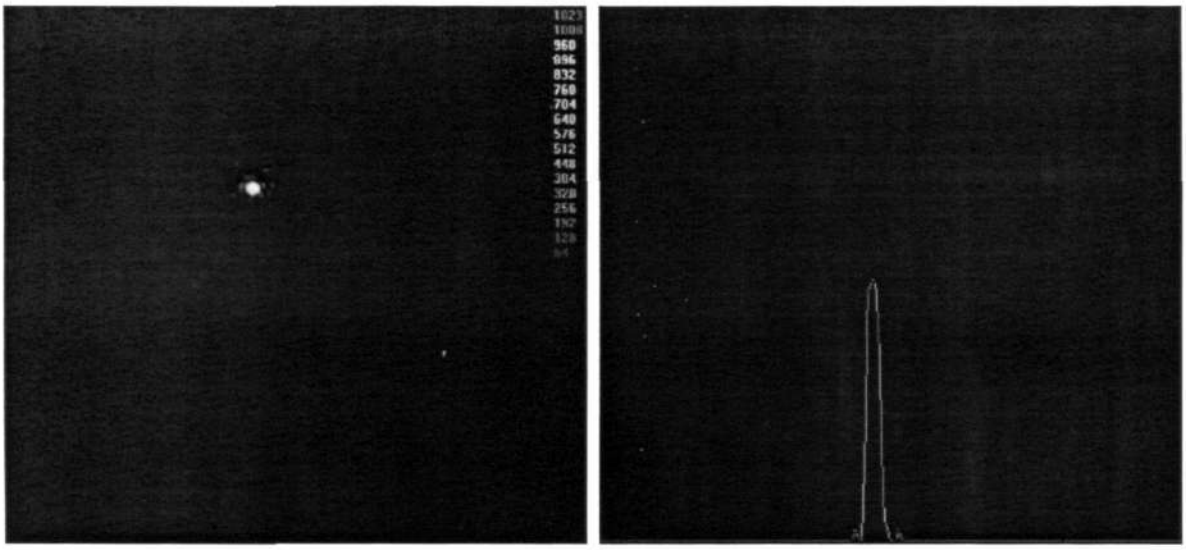

(a) (b)

Fig.6-8. PSF of a microlens measured by an optical setup shown in Fig.6-6. (a).

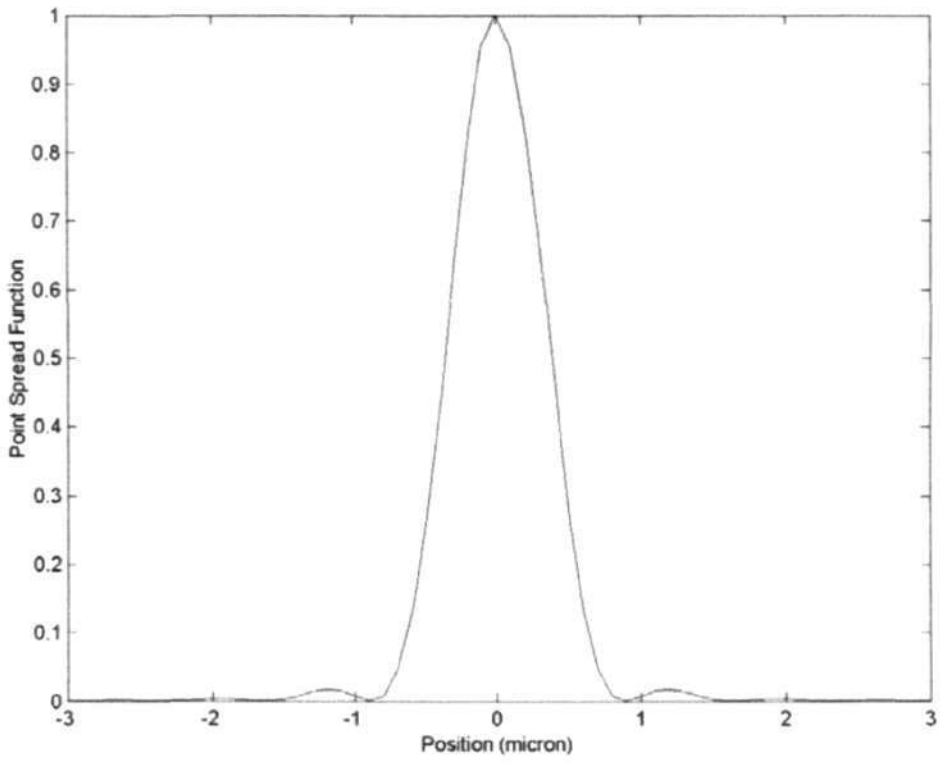

PSF imaged on CCD camera, (b) PSF profile along the diameter.

Fig.6-9. Simulated point spread function.

6.3. Modulation Transfer Function

A more accurate evaluation of imaging quality of an optical system should be its modulation transfer function. To derive the modulation transfer function, one can take the Fourier transform of the PSF shown in the following equation,

$$OTF = FFT(P) \tag{6-5}$$

where, P is PSF and FFT denotes the Fourier transform. OTF is known as the optical transfer function (OTF) that is not normalized. OTF is a complex value and can be expressed as [94],

$$OTF = MTF(\xi,\eta)e^{i\psi(\xi,\eta)} \tag{6-6}$$

where MTF is known as the modulation transfer function and $\psi(\xi,\eta)$ denotes the phase transfer function. Generally, MTF is expressed as a normalized shape.

To get the experimental MTF, one has to take a Fourier transform of measured PSF. This procedure is realized with the help of Matlab. Fig.6-10 shows the MTF of the same microlens derived from PSF. Fig.6-10a shows the 3-dimensional profile and Fig.6-10b shows the 2-dimensional profile with diffraction limited MTF. It is seen from Fig.6-10b that the measured MTF departs from the diffraction limited and it decreases at a faster rate.

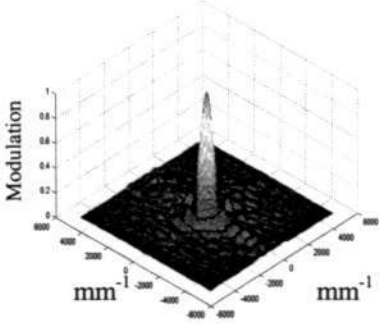

Fig.6-10a

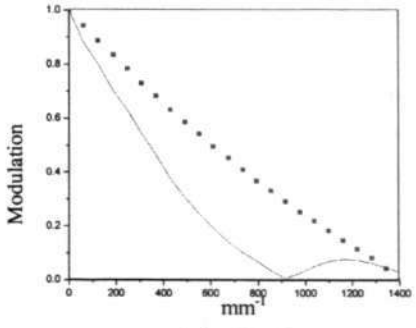

Fig.6-10b

Fig.6-10. Experimental MTF 3D (left) and 2D (right).

6.4. Conclusions

The microlens array fabricated by soft-lithography in hybrid sol-gel glass was characterized to evaluating its optical properties. A Twyman-Green interferometer was set up and applied for measurement of the focal length of microlens. The measured results is different from that predicted by the surface profiler as the surface profiler is only a rough tool to evaluate the focal length of the microlens. In addition, the PSF of the fabricated microlens was imaged by a CCD camera with a 60× microscope attached onto its front. The measured result agrees well with diffraction limited one. Based on the PSF obtained from experiment, the MTF of the microlens was derived and seems close to the diffraction limited except that it decreases faster.

Chapter 7. Design and application of sol-gel microlens for fibre coupling

Optical Fibre is a key element in optics communication circuits and many other photonics applications. In general, optical fibre can be melted and adhered to each other. However, in some cases, optical fibres cannot be connected directly and there is difficulty to transmit optical energy from one fibre to the other. An example is the received optical energy at a detector from an output fibre that is pig tailed. In this case, an external coupler have to be used to convert the astigmatized beam in air into a matching mode that can propagated in an optical fibre so that the maximum optical power can be coupled and received.

Lens, being a very common optical element, is widely used in optical imaging systems such as camera, microscope, telescope and so on. Microlens as a microoptical element has been used for optical interconnection in many cases in photonics. The main feature of microlens is its miniature size and that it is compatible with microoptical systems and optical communication systems.

In this chapter, a high efficiency microlens coupler is designed for fibre-to-fibre coupling. To design a microlens coupler, the Code.V optical design software is used due to its powerful function in lens design.

7.1 Introduction of Code.V software for photonics simulation

Code.V was originally developed as a tool for designing and analyzing image forming optical systems such as microscopes, cameras, laser scanners, and scientific instruments [95]. While for many photonics systems, there are many

components such as microlens that has a similar function used in microoptical systems. Therefore Code.V has a great potential for photonics modeling application. However, there are some advantages and disadvantages. The advantages of using Code.V for photonics modeling lie in three aspects. Firstly, Code.V can model an extremely broad range type of systems and provide powerful optimization and analysis capabilities, as well as a robust macro language for extending its calculations. Secondly, Code.V can handle systems with many surface types, diverse materials (including gradient index), general diffraction gratings, multi-wavelength, different polarization properties (including birefringence), multi-layer coatings, and even user-defined properties. It provides analysis options such as diffraction beam propagation (BPR), diffraction-based evaluations including polarization effects (e.g., point spread function and encircled energy), and many types of geometrical optics-based calculations. Finally, Code.V provides a special feature of calculating diffraction-based coupling efficiency (also known as insertion loss). This calculation is normally based on the standard diffraction point spread function, which includes the effects of polarization and coatings. It is also possible to calculate coupling efficiency by importing data from the more rigorous beam propagation (BPR), although, in this case, polarization and coating effects are not included. The disadvantage of using Code.V for photonics modeling is it cannot be used for modeling integrated optics or waveguide-type systems. Code.V is used to model discrete components such as lenses, prisms, mirrors, filters, gratings, gradient index rods, and polarizing elements.

If Code.V is used for modeling fibre-microlens-fibre coupling, two kinds of elements, the optical fibre and the microlens should be modeled. Modeling of microlens is a basic function of Code.V. However, there is a problem when Code.V

is used for modeling fibres. In most cases, the optical fibres themselves are not modeled in Code.V, and usually do not need to be modeled, as Code.V is typically used to design components that interface with optical fibres. Due to this, another way of defining the properties of the light emerging from a fibre that is then processed by the device we wish to model is required. For certain analysis, such as coupling efficiency, the input properties of a fibre needs to be defined too. Code.V has these capabilities. When Code.V is applied to photonics systems, it can perform many analyses. Code.V can perform geometrical calculations such as simple ray tracing, spot diagrams, and encircled energy, which are useful in the early stages of component design. To evaluate system performance, Code.V uses the diffraction point spread function (PSF) or, more often, the coupling efficiency (CEF), which is derived from the PSF. Code.V macros allow us to study CEF vs. Wavelength, which is important for WDM systems. The beam propagation feature (BPR) also enable us to examine the amplitude and phase of a beam anywhere in the system. BPR is a powerful feature, but it requires careful attention to issues of sampling to get the most accurate results. In addition, tolerance analysis is also available.

Another powerful function when Code.V is used for photonics systems modeling is that it provides a powerful optimization engine called AUTO (for automatic design). This feature systematically varies system parameters to reduce the size of a specified "error function" that correlates with image quality.

7.2 Functions of Code.V when used for modeling of fibre coupling

Code.V has integrated a function of beam propagation method into its package. Beam propagation is the only accurate method for analyzing diffraction beam in scalar domain in optical systems. When Code.V is used for the modeling of fibre

coupling, the beam propagating in all systems is modeled by a diffraction-based beam propagation method. Beam propagation traces a beam through an optical system, using diffraction-based propagation techniques in conjunction with geometrical ray tracing and displays the intensity and phase at selected surfaces. The input beam can be specified in terms of intensity or phase using an interferogram file, or an array of complex numbers read from a worksheet buffer, or as a Gaussian field distribution. Alternatively, the input beam is specified as a spherical wavefront, with or without aberrations, using LDW specifications.

Beam propagation (BPR) is different from other diffraction analysis methods in CODE.V. In PSF and CEF (which uses PSF data by default), the program assumes that all diffraction takes place at the exit pupil of the system, with a pupil shape and position derived from ray tracing. BPR also uses ray tracing, but it converts back and forth between a wave and a ray representation of the beam. This means it can handle diffraction effects anywhere in the system, not only at the exit pupil. In some situations, BPR and PSF will give almost identical results, while in others, BPR is the only accurate calculation (e.g., with a diverging Gaussian beam in a long air space between optical elements and/or fibres).

In the following, a brief introduction of beam propagation and its derivation is described.

Beam propagation method was first formulated by Van der Donk and Lagasse [96] and then improved by Gribble and Arnold [97] in 1998, Enrico Nichelatti and Giulio Pozzi [98] in 1998 respectively. Here, only the formulation derived by Enrico Nichelatti and Giulio Pozzi is introduced.

1. Paraxial Approximation

Propagation of a monochromatic wave in the scalar approximation is described by the scalar homogenous Hemholtz equation

$$\nabla^2 E(\vec{r}) + \frac{4\pi^2}{\lambda^2} n^2(\vec{r}) E(\vec{r}) = 0, \tag{7-1}$$

Where $\vec{r} \equiv (x, y, z)$, E is the wave function, ? is the wavelength in vacuum, n is the index distribution, and ∇^2 represents the Laplacian operator.

Assuming the z direction for the optical axis, then it can be simplified to,

$$\nabla_\perp{}^2 \psi(\rho, z) + i\frac{4\pi}{\lambda} n(0,z) \frac{\partial \psi}{\partial z}(\rho, z) + \frac{4\pi^2}{\lambda^2}\left[n^2(\rho, z) - n^2(0,z)\right]\psi(\rho, z) = 0 \tag{7-2}$$

Where, $\psi(\rho, z)$ is the normalized wave function with respect to the energy flux along z.

2. BPM equation

Suppose the wave function propagates from a plane $Z=Z_0$, the object plane, to $Z=Z_N$, the image plane. The spatial region between Z_0 and Z_N is subdivided into N slices of equal thickness and separated by N-1 planes at $Z=Z_k$ (k=1,…, N-1), with $\delta z = z_{k+1} - z_k$.

The wave propagation from Z_0 to Z_N is represented as,

$$\psi(\rho, z_N) = \hat{S}_{N-1}\hat{P}_{N-1}\hat{S}_{N-2}\hat{P}_{N-2}\cdots\hat{S}_1\hat{P}_1\hat{S}_0\hat{P}_0\psi(\rho, z_0) + O(\delta z^2) \tag{7-3}$$

Where $\hat{P}_k$ and $\hat{S}_k$ are the following operators,

$$\hat{P}_k \equiv \exp\left(i\frac{\lambda\delta z}{4\pi n_{0,k}}\nabla_\perp{}^2\right) = 1 + i\frac{\lambda\delta z}{4\pi n_{0,k}}\nabla_\perp{}^2 + O(\delta z^2) \tag{7-4}$$

$$\hat{S}_k \equiv \exp\left(i\frac{\pi}{\lambda}\frac{n_k{}^2 - n_{0,k}{}^2}{n_{0,k}}\delta z\right) = 1 + i\frac{\pi}{\lambda}\frac{n_k{}^2 - n_{0,k}{}^2}{n_{0,k}}\delta z + O(\delta z^2) \tag{7-5}$$

These two exponential form of operators guarantees that the numerical process is energy conserving.

To compute the coupling efficiency, the point spread function of the beam is firstly calculated by beam propagation. Then the coupling efficiency can be computed by evaluating the overlap integral of the complex PSF and the fiber mode profile, appropriately normalized. The equation used is that PSF is a complex quantity and the mode profile is a scalar quantity.

$$CE = \frac{\left|\iint (PSF \bullet \mathrm{mod}\, e)\right|^2}{\iint PSF \times PSF^* \bullet \iint \mathrm{mod}\, e^2} \tag{7-6}$$

For Code V, the coupling efficiency is calculated based on the formula above. The PSF of the beam that incidents on the front-end surface of the receiving fibre is firstly simulated by using the beam propagation method, then substitute the PSF (in complex form) in the above formula to get the coupling efficiency. This is a relatively rigorous method.

7.3 Designing a microlens as a fibre-to fibre coupler

The most important consideration in the fibre-microlens-fibre coupling problem or any other coupling problem is mode matching. So far, to the best of our knowledge there are hardly literatures concerning a detailed design of microlens couplers. Here we present a detailed design of microlens coupler for fibre-to-fibre coupling by employing a beam propagation method. The dependence of coupling efficiency on the microlens aperture radius, numerical aperture and spherical aberration is discussed thoroughly. With this method, a coupling efficiency of more than 95% can be obtained. The method is also helpful for other problems associated with the microlens.

7.3.1 Gaussian beam propagating in free space and definition of fibre-microlens-fibre coupling problem

It is well know that the intensity distribution of the optical beam emitting out from optical fibre has a Gaussian shape. The waist ω_0 of the Gaussian beam is expressed as [99],

$$\omega_0 = 0.65 + \frac{1.619}{V^{3/2}} + \frac{2.879}{V^6} .a \tag{7-6}$$

where ω_0 is the waist of Gaussian beam, a is the core diameter and V is the waveguide parameter expressed as the following formulation,

$$V = 2\pi \frac{a}{\lambda_0} NA \tag{7-7}$$

where, NA is the numerical aperture of the waveguide.

This Gaussian beam coming from the fibre propagates in free space with a divergent mode and as a result its beam size will expand with the beam propagating forward. The expanded beam radius is given by the following equation,

$$\omega = \omega_0 \left[1 + \left(\frac{\lambda z}{\pi \omega_0^2} \right)^2 \right]^{\frac{1}{2}} \tag{7-8}$$

For a typical single mode fibre $\omega_0 = 5.2\,\mu m$. If we use a wavelength of 1.55μm laser source, then the expanded beam radius vs. propagation distance can be illustrated by the curve in Fig.7-1,

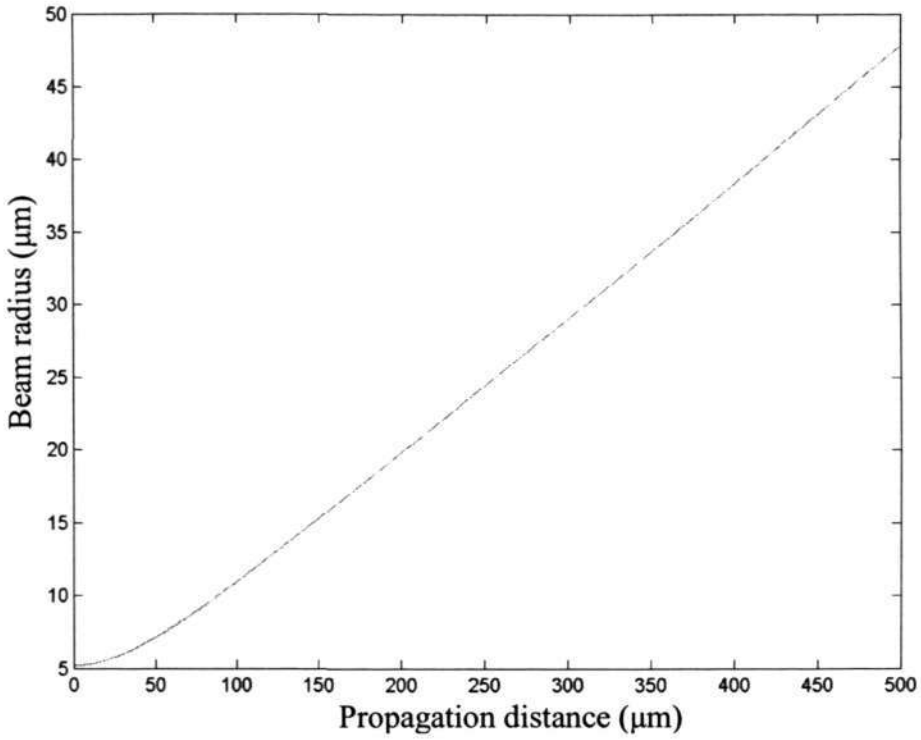

Fig.7-1. Expanded beam radius vs. propagation distance.

Clearly shown in Fig.7-1, the beam radius is expanding and if it incidents directly on the receiving optical fibre, a large optical loss will definitely happen. This loss is called longitude loss and the formula is expressed as follows,

$$L = -\log\left(\frac{4}{\frac{\lambda^2 z^2}{\pi^2 \omega_0^2}}\right) \tag{7-9}$$

From the above equation, a relationship between coupling loss and propagation distance can be calculated and it is shown in Fig.7-2. As can be seen from Fig.7-2, the optical coupling loss increases as the propagation distance increases.

Specifically, at a propagation distance of 110 μm, optical coupling loss reduces 3dB, which means that 50% optical intensity has been lost.

To increase the coupling efficiency, a microlens coupler is an alternative method. The aim of the introduction of microlens into fibre coupling system is to convert the divergent beam mode into a matching mode that can be accepted as much as possible to propagate in optical fibre.

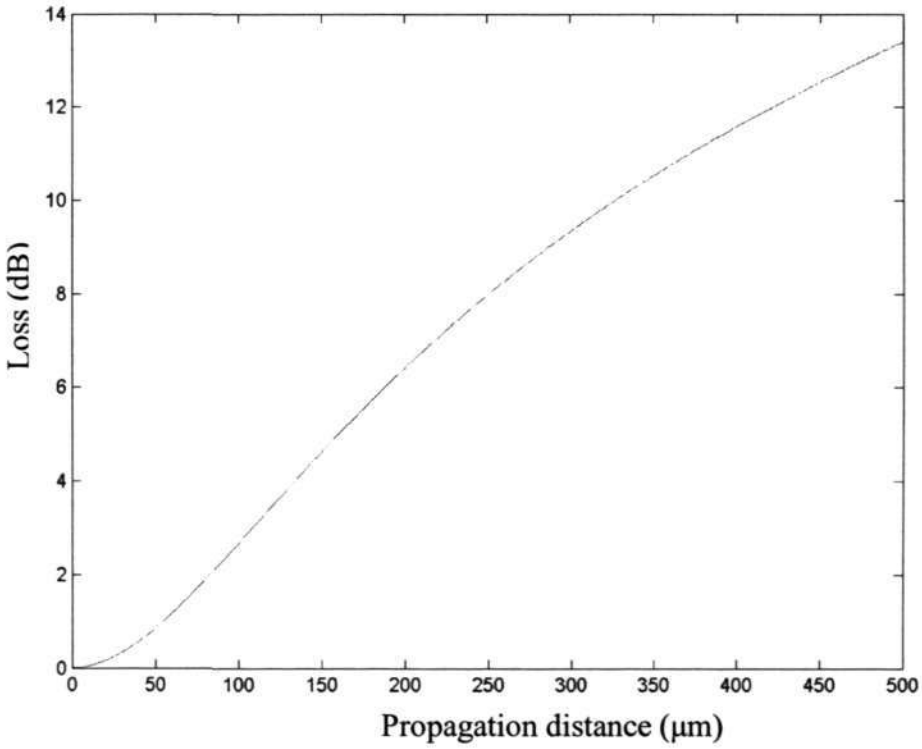

Fig.7-2.Optical coupling loss vs. propagation distance.

7.3.2 General considerations for fibre-microlens-fibre coupling problem

Since the output mode from a single mode fibre is divergent and the beam will be expanded with propagation in air, a microlens has to be used to converge the divergent beam into a specific beam mode suitable for further propagation in fibre. The typical mode of a single mode fibre has a diameter of 10.5 μm, which equals to the diameter of Airy disc of a microlens with a numerical aperture of 0.18 at wavelength of 1.55 μm. The Airy disc diameter is given by,

$$D = \frac{1.22\lambda}{NA} \tag{7-10}$$

where λ is 1.55 μm and *NA* is the numerical aperture of the microlens. Clearly, it is seen that the higher the numerical aperture of the microlens, the smaller the diameter of the beam mode can be converted. Thus, to contract the expanding beam mode, the numerical aperture of the microlens must be larger than 0.18.

In addition, aperture radius of the microlens is usually chosen as 60 μm so as to be compatible with the 125 μm cladding diameter of the fibre. Such microlens is also suitable for fibre array coupling to avoid crosstalking of signals between the adjacent fibres. For a point source with an object numerical aperture of 0.144, a 400 μm object distance will make the expanding wavefront from the point source fill out the microlens aperture. From geometrical optics point of view, if the object distance is twice as the focal length, the transverse magnification will be 1. So a microlens with a focal length of 200 μm can be used as a converter for fibre-to-fibre coupling. Thus, the initial parameters of the microlens are listed in Table 7-1.

Object distance	Focal length	Aperture radius of microlens
400 μm	200 μm	60 μm

Table 7-1. The starting parameters of microlens coupler

For a plano-convex microlens, the sag height can be determined by the following equations,

$$NA = \frac{r}{f}$$
$$h = (n-1)f - \sqrt{(n-1)^2 f^2 - r^2} \tag{7-11}$$

where f is the focal length, r is the aperture radius of the microlens, h is the sag height and n is the refractive index. In the case of $NA=0.3$, $r=60$ μm and $n=1.5$, the sag height of 20 μm can be determined by simple calculations based on the above

equations.

By employing beam propagation method, the beam mode that inputs onto the front end of the receiving fibre has a radius of 5 μm. The corresponding coupling efficiency versus misalignment is evaluated and shown in Figure 7-3. It is seen that the maximum coupling efficiency can be up to 95%.

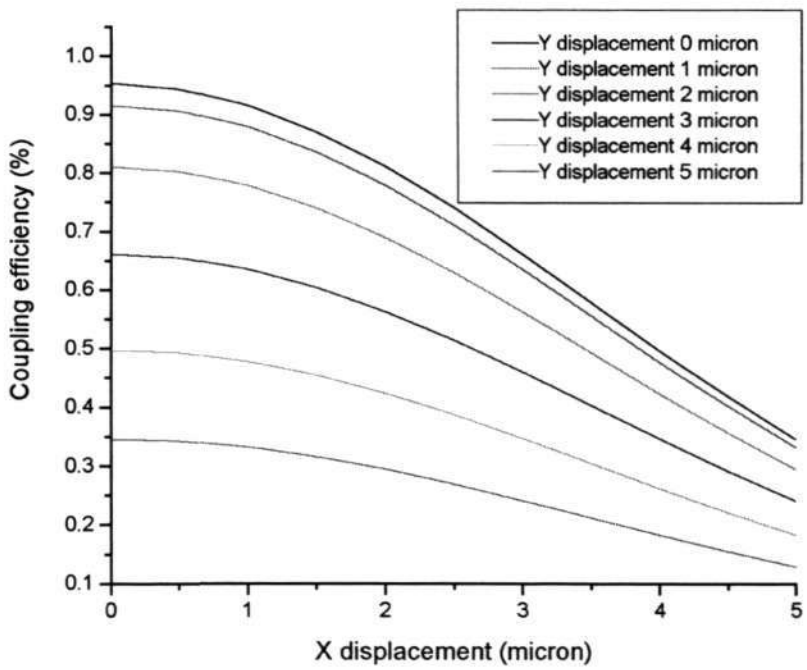

Figure 7-3. Coupling efficiency versus misalignment for microlens with an aperture radius of 60 μm and a sag height of 20 μm.

7.3.3 Coupling efficiency versus aperture radius of microlens with a fixed numerical aperture

In the previous section, we have implemented a design of a microlens coupler with a numerical aperture of 0.3, with the microlens aperture radius fixed as 60 μm. In this section, we discuss the impact of the aperture radius of the microlens on the coupling efficiency with a fixed numerical aperture.

To analyze the impact of aperture radius on the coupling efficiency, five microlens couplers with the same numerical aperture of 0.3 but different aperture radii of 30μm, 60μm, 120μm, 180μm and 240μm are analyzed respectively. A comparison of the impact on the coupling efficiency is listed in Table 7-2. It is seen that, with the same numerical aperture, the bigger the radius, the larger the sag height, the lower the coupling efficiency and the bigger the lateral spherical aberration. Obviously, to keep the same numerical aperture, the sag height has to be increased. For microlens with an aperture radius of 240 μm, the sag height needs to be as large as 80 μm, which is usually difficult to fabricate in practice. The coupling efficiency reduces to less than 90% if the radius increases to a value larger than 120 μm. For example, if the radius is increased to 240 μm, the coupling efficiency will be reduced to 63.8%. Clearly, the reduction of coupling efficiency accompanies the increase of lateral spherical aberration. Since the fiber coupling is an on-axis system, the main aberration is lateral spherical aberration. Thus, it is necessary to investigate the effect of lateral spherical aberration on the coupling efficiency. It can be seen from the Table 7-2 that, the lateral spherical aberration increases from 11.3 μm to 90.6 μm following the increase of the aperture radius of the microlens. As a conclusion, these lateral spherical aberrations respectively correspond to 1.8, 3.6, 7.2, 10.7 and 14.4 times of the Airy disc diameter of 6.3 μm for a microlens with a 0.3 NA. A higher lateral spherical aberration means that the converting beam mode has a larger difference from an ideal Gaussian function although the radius is close to the typical mode radius of 5.2 μm, therefore a lower coupling efficiency is expected. Figure 7-4 shows the beam modes incident onto the front end of the receiving fiber through microlenses with different radius but the same numerical aperture. It is seen in the figure that the magnitude of the bright ring surrounding

the center circular bright spot becomes stronger and stronger with the increase of the microlens radius, which means more and more energy is redistributed into the outer ring of the beam mode so that the converted beam mode becomes more and more divergent from the required beam mode for the fibre. Thus we can see the coupling efficiency becomes lower with the increase of the microlens radius.

Radius	30μm	60μm	120μm	180μm	240μm
Sag height	10μm	20μm	40μm	60μm	80μm
Mode radius	4.4μm	5.0μm	5.6μm	5.4μm	5.2μm
Coupling efficiency	94.3%	95.4%	90.4%	79.3%	63.8%
Lateral spherical aberration	11.3μm	22.5μm	45.1μm	67.6μm	90.6μm

Table 7-2. List of sag height, mode radius, lateral spherical aberration and coupling efficiency for microlenses with different radius but the same numerical aperture.

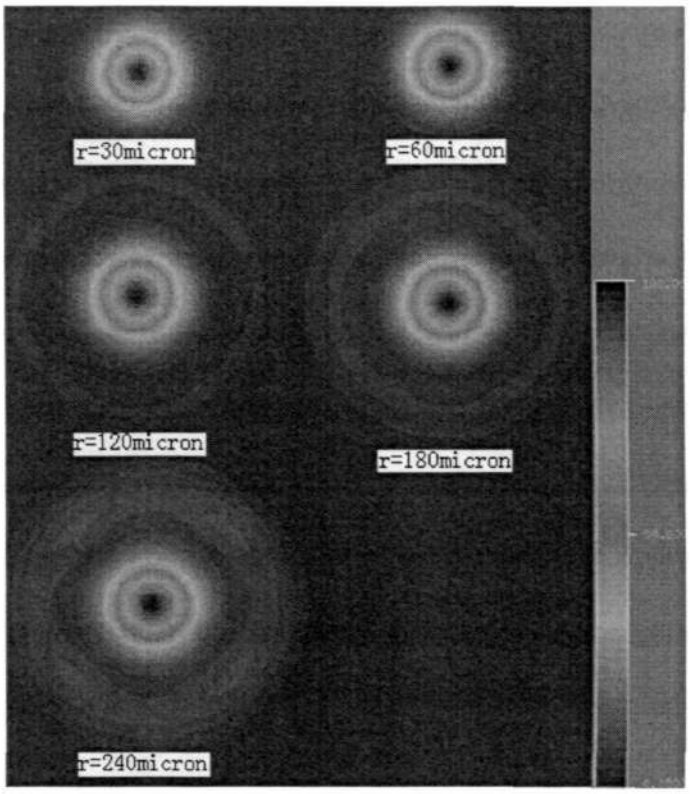

Fig. 7-4. Beam modes converted by microlenses with different radius.

7.3.4 Coupling efficiency versus numerical aperture with a fixed radius of microlens

It is shown from the previous section that the minimum numerical aperture of the microlens should be 0.3 if the aperture radius of the microlens is smaller than 60 μm. If the numerical aperture is fixed, the coupling efficiency will be reduced as the radius of the microlens is increased. In this section, we will discuss the relationship between the coupling efficiency and the numerical aperture of the microlens when the radius is fixed at 60 μm.

Table 7-3 shows the coupling efficiency relating to the microlens parameters for different numerical apertures. It is seen from the table that all three microlens couplers can realize a coupling efficiency of above 95%. The beam mode radii are nearly the same. For lateral spherical aberration, it shows that the higher the

numerical aperture, the smaller the lateral spherical aberration. However, if we further consider the Airy disc diameter, it gives 6.3 μm for the 0.3 NA, 4.7 μm for the 0.4 NA and 3.8 μm for the 0.5 NA respectively. The lateral spherical aberration in each NA case is found to be about 3.6 times of its corresponding Airy disc diameter. This means that the impact of lateral spherical aberration on the coupling efficiency is invariable for NAs of 0.3 and above. Thus, for fibre-microlens-fibre coupling systems, a high numerical aperture will always give a high coupling efficiency. However, concerning the practical fabrication, we prefer the microlens with a numerical aperture of 0.3, which requires the minimum sag height so that it is easier to be fabricated.

Numerical aperture	0.3	0.4	0.5
Sag height	20 μm	30 μm	60 μm
Mode radius	5.0 μm	4.9 μm	4.8 μm
Lateral spherical aberration	22.5 μm	16.9 μm	13.5 μm
Coupling efficiency	95.3%	95.5%	95.2%

Table 7-3. List of sag height, mode radius, lateral spherical aberration and coupling efficiency for microlenses with different numerical aperture but the same radius.

7.4 Application of sol-gel microlens fabricated by soft-lithography for fibre coupling

In this section, We demonstrated the application of sol-gel microlens for fibre coupling. A plano-convex microlens coupler was designed for fibre-to fibre coupling with Code.V optical design software. The main concern in this design is to define a microlens that can make a perfect matching of propagation modes between the output fibre and the receiving fibre. The coupling efficiency is estimated by fitting the beam profile calculated by beam propagation method onto the front end

of the receiving single mode fibre with the standard propagation mode. The designed microlens has a diameter of 80μm and a sag height of 13μm. The wavelength used in the design is 1550nm and the glass material used in the design is BK7_SCHOTT that has a refractive index of 1.5, which is compatible with the sol-gel glass we used. Fig.7-5 shows the beam intensity distribution on the front of the receiving fibre calculated by Beam Propagation method. The beam intensity radius at the $1/e^2$ of the peak intensity is 5.6μm that is very close to the standard mode radius of 5.2μm for the single mode fibre. Fig 7-6 shows the simulated coupling efficiency against the misalignment. The maximum coupling efficiency can be as much as 0.3dB (93%).

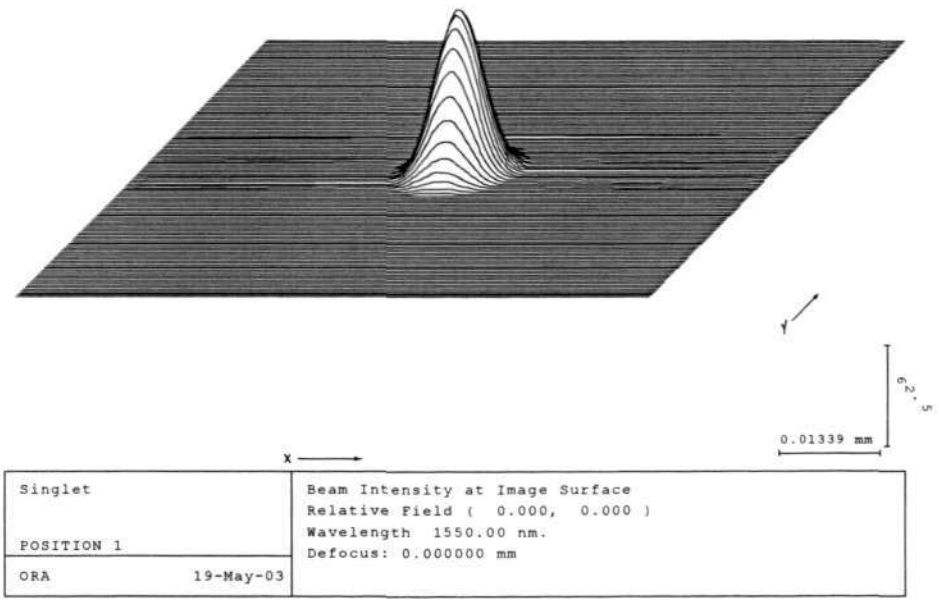

Fig.7-5. Beam intensity distribution on the front of the receiving fibre.

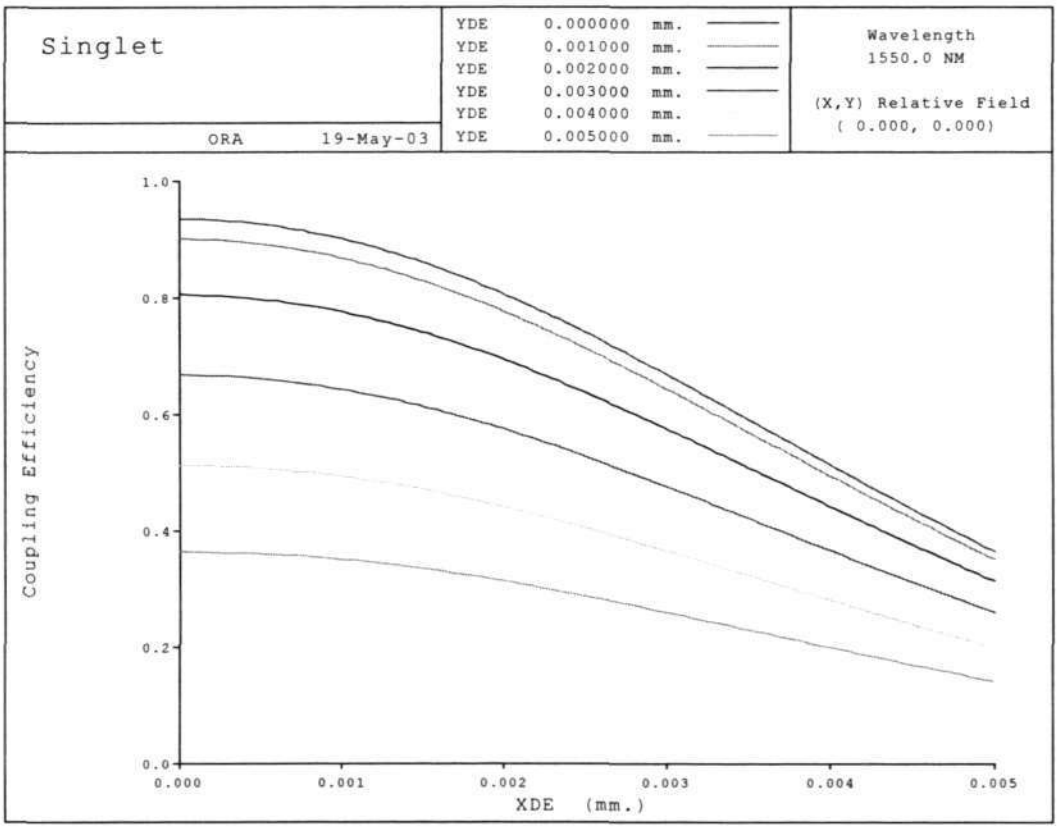

Fig.7-6. Coupling efficiency against the misalignment.

Based on above design, we fabricated a microlens array by using soft-lithography method in sol-gel glass. A 32×32 microlens array with a pitch of 85μm and each lens having a diameter of 80μm was fabricated. Figure 7-7a shows the sol-gel microlens array imaged by a Scanning Electron Microscope (JEOL SEM). The surface profile shown in Fig.7-7b was measured by a Dektak surface profiler (Veeco Metrology). Surface roughness is also a very important parameter for an optical element. The fabricated microlens surface roughness as shown in Fig.7-8 is characterized by scanning a random area of 500nm×500nm on the microlens by an AFM. The measured root mean square (RMS) value is 0.482 nm, which shows a good quality optical surface that is comparable with BK7 glass.

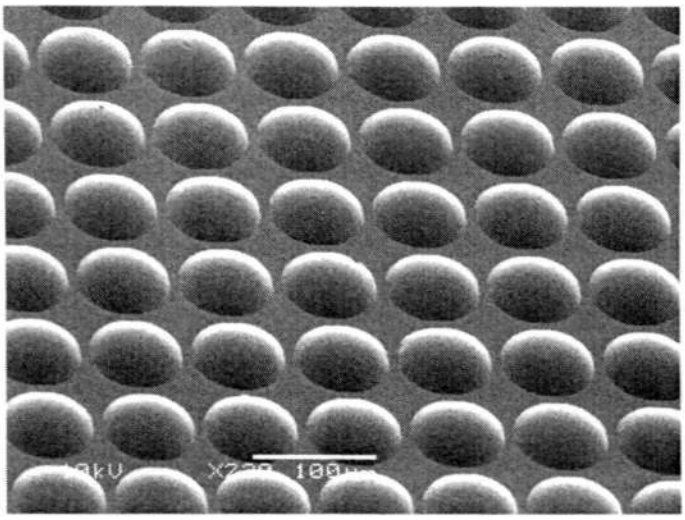

Fig.7-7a. SEM picture of a sol-gel microlens array, each lens has a diameter of 80μm

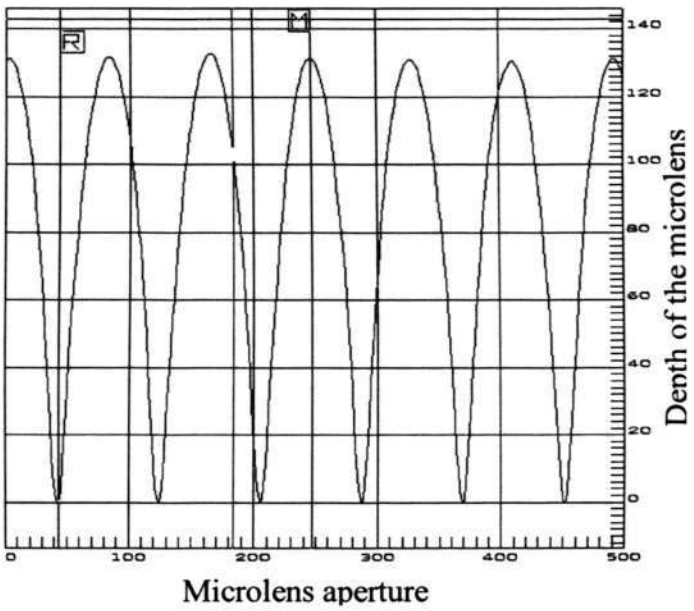

Fig.7-7b. Surface profile of the microlens array.

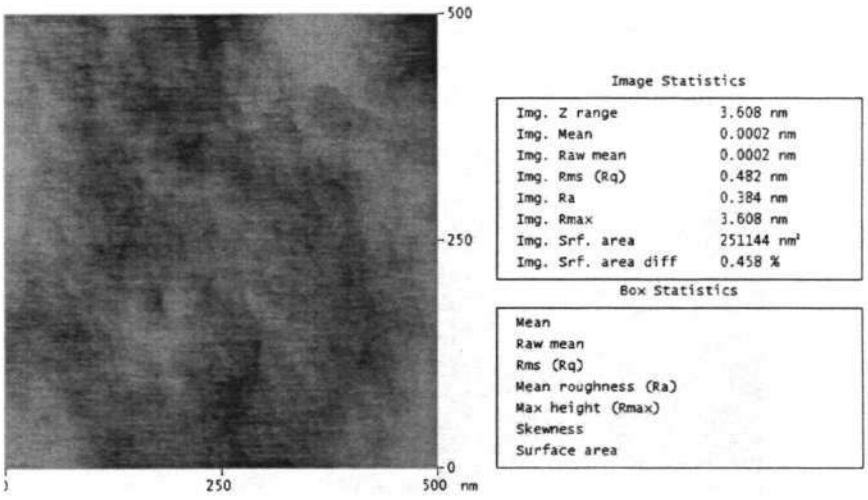

Fig.7-8. Surface roughness of the microlens characterized by an AFM.

The fabricated sol-gel microlens was used as a coupler between two single mode fibres. To evaluate its coupling efficiency, we implemented an experiment as shown in Fig 7-9.

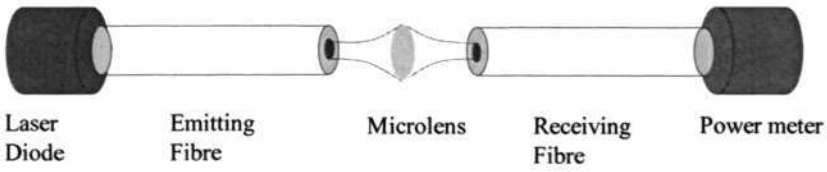

Fig.7-9. Optical setup for fibre-to-fibre coupling using a microlens.

In this experiment, we first fixed the distance between the two fibres according to the design. Then, we aligned the two fibres accurately by observing that the power coupled into the receiver fibre was the maximum. Finally, we inserted the microlens in the middle of the fibres and aligned the three elements to maximize the coupling power. The two fibres and the microlens were mounted individually on three five-axis precision stages that have a resolution of 10μm. The measured coupling efficiency is 2.2dB (60%), which is about 2/3 of the theoretical maximum coupling efficiency 93%. This is because the coupling efficiency is highly dependent on the

system alignment. It is indicated in Fig. 7-6 that the efficiency dropped to less than 3dB (50%) with a 5μm misalignment. In the coupling experiment, since the stage resolution is limited to 10μm, the reduced coupling efficiency in the measurement is reasonable. With an ultra precision stage, achieving higher efficiency is feasible.

7.5 Conclusions

In this chapter, we've discussed a detailed design of fibre-microlens-fibre coupling system by employing beam propagation method. The analysis results show that a larger radius microlens has a lower coupling efficiency if the numerical aperture is fixed. Furthermore, if the aperture radius of the microlens is fixed, the microlens must have a numerical aperture of 0.3 or above to provide a high coupling efficiency.

Based on the proposed optical design theory of fibre-microlens-fibre coupling, we fabricated a sol-gel microlens array by using soft-lithography introduced in chapter 5 and applied this microlens array for fibre coupling, a 60% coupling efficiency in experiment was obtained. Compared with the coupling efficiency predicted by theoretical simulation, 93%, a further improvement of coupling efficiency could be made by employing an ultra precision alignment setup.

Chapter 8. Conclusions and recommendations

8.1 Conclusions

Nowadays, microoptical elements have found many applications such as optics interconnection, information processing, and optics communications, *et al.* To fabricate microoptical elements with a cost-effective and simple approach has attracted many attentions. Photosensitive hybrid sol-gel glass has been showing a great potential for fabrication of microoptical elements for photonics applications. In this thesis, much work about photosensitive hybrid sol-gel glass has been done to further improve its application in photonics. The work is summarized as follows,

1. Developed a new recipe of photosensitive sol-gel glass. The new sol-gel glass shows a great optical property, the average transmittance in visible and infrared band is as large as 95%.
2. The photosensitive sol-gel glass has been characterized by using variable fabrication method including holographic interference method, laser direct writing technique, mask aligner plus a grey scale mask, electron beam lithography. The calibration results were used for the fabrication of microoptical elements with a continuous surface relief structure. Many microoptical elements and diffractive optical elements including blazed gratings, sinusoidal gratings, and refractive microlens were fabricated.
3. Developed a novel mass fabrication method and this method was used to fabricate microlens array for fibre-to-fibre coupling. The maximum coupling efficiency measured is 2.2dB (60%), while the theoretical coupling efficiency simulated by using Code.V optical design software is more than 93%.

4. The fabricated sol-gel microlens was characterized by optical method to evaluate its optical properties such as focal length, point spread function and modulation transfer function.

8.2 Recommendations for future research

We have demonstrated that the hybrid sol-gel material can be used for fabrication of microoptical elements such as diffractive gratings, microlens array and so on. The fabricated microlens array also was applied for fibre coupling to enhance coupling efficiency. However, there are still much future works to do to explore and expand the application of this kind of sol-gel material. The following are some specific chanllenge and improvement to be made for the future work,

1. To explore more application of sol-gel microoptical elements for photonics.

   In this thesis, only one practical application of sol-gel microlens was demonstrated. But actually there are many other applications for microlens and microlens array such as microlens can be used as collimating lens for laser diode, microlens array can be used for coupling of fibre array to fibre array or fibre array to arrayed waveguide graing.

   However, when applied the sol-gel microlens array as a coupler or as a collimating lens, the big challenge is how to mount the microlens array and how to control the alignment precisely.

2. To explore and find a new cost-effective and fast fabrication method so that the sol-gel material can be used for mass fabrication of microoptical elements.

   Soft-lithography is a potential mass fabrication method. However, the fabrication method introduced in this thesis is only pertained to fabrication of microlens and also unfortunately the process is all manually controlled.

As a mass fabrication method for industrial use, the process must be controlled by machine as much as possible and also other microoptical elements besides microlens such as diffractive gratings can be fabricated.

Based on above requirement, transfer molding is a possible solution. By combining transfer molding method and softlithography method, we can fabricate any microoptical elements in hybrid sol-gel material. In this process, you must have a microoptical elements master, and then make a replica in PDMS. Once you get a PDMS replica, this replica is used as a mold to impress into the sol-gel material to form the required microstructure. The challenge for this transfer molding method is how to control the pressure precisely as the mold material is PDMS that is a rubber like material and is subject to an elongation upon pressure.

3. To explore and develop a method so that the nanostructure or nanooptical elements can be fabricated in sol-gel material.

   X-ray lithography could be a candidate for fabrication of nanooptical elements in sol-gel material. However, one has to characterization the sensitivity of this sol-gel material to X-ray exposure energy and thus to optimize appropriate process parameters to fabricate a quality nanooptical elements in sol-gel material. Of course, X-ray lithography is a very expensive tool and seems unsuitable for industry use so far.

In a word, it is very attractive to fabricate microoptical or nanooptical elements in sol-gel material and even in a mass production method, however much work need to do to realize this aim.

Author's publications

Journal publications

1. Weixing Yu and X-C Yuan, "Patternable photosensitive hybrid material cuts cost for fabrication of microoptical elements for photonics applications", J. Mat. Chem. Vol.14, 2004, 821-823.
2. Weixing Yu and X-C Yuan, "Localized self-volume growth in hybrid sol-gel glass induced by UV radiation with a grey scale mask", Applied Optics. Vol.43, No.3, 2004, 575-578.
3. Weixing Yu and X-C Yuan, "Fabrication of multilevel structures in self-developemnt photosensitive sol-gel glass by a grey scale mask", Optical Engineering Letters. Vol.42, No.12, 2003, 3411-3412.
4. Weixing Yu and X-C Yuan, "A Simple Method for Fabrication of Thick Sol-gel Microlens as a Single Mode Fibre Coupler", IEEE Photonics technology Letters, Vol.15, No.10, 2003, 1410-1412.
5. Weixing Yu and X-C Yuan, "Point-to-Point UV laser direct writing initiated volume growth in Hybrid sol-gel glass for 3D microfabrication", Optics Letters, Vol.28, No.17, 2003, 1573-1575.
6. Weixing Yu and X-C Yuan, "UV induced controllable volume growth in hybrid sol-gel glass for fabrication of a refractive microlens by use of a grey scale mask", Optics Express, Vol.11, 2003, 2253-2258.
7. Weixing Yu and X-C Yuan, "Variable surface relief gratings in hybrid sol-gel glass fabricated by holographic interference", Optics Express, Vol.11, 2003, 1925-1930.

8. W.X. Yu and X-C Yuan, "Fabrication of refractive microlens in hybrid SiO2/TiO2 sol-gel glass by electron beam lithography", Optics Express, Vol.11, 2003, 899-903.
9. X. -C. Yuan, W. X. Yu, N. Q. Ngo and W. C. Cheong, "Improved sol-gel thin film for fabrication of multilevel structures using an HEBS grey scale mask", Optical Engineering Letters. Vol.42, No.12, 302-303, 2003.
10. W. X. Yu, X. -C. Yuan, N. Q. Ngo, W. X. Que, W. C. Cheong and V. Koudriachov, "Single- step fabrication of continuous surface relief micro-optical elements in hybrid sol-gel glass by laser direct writing", Optics Express, Vol.10, No.10, 2002, 443-448.
11. X. –C. Yuan, W. X. Yu, N. Q. Ngo and W. C. Cheong, "Cost-effective fabrication of microlenses on hybrid sol-gel glass with a high-energy beam–sensitive grey-scale mask", Optics Express, Vol.10, No.7, 2002, 303-308.
12. X. -C. Yuan, W. X. Yu, N. Q. Ngo and W. C. Cheong, "Improved linear response to UV exposure and its interpretation of SiO_2/TiO_2 hybrid sol-gel glass", J. Phys. D: Appl. Phys. Vol.35, No 17, L81-L84, 2002.

Conference proceedings

1. Weixing Yu, X-C Yuan, N.Q.Ngo and V.Kudryshov, "Design and Fabrication of Sol-gel Microlens array as a fibre-to-fibre and fibre-to-waveguide coupler", SPIE International Symposium, Micromachining and Microfabrication, Part of Photonics West. San Jose, California USA, (2004).
2. Weixing Yu, X-C Yuan, N Q Ngo, W C Cheong, V. Kudryshov, "Characterization of TiO2/SiO2 Hybrid Sol-Gel Glass and its Use for Fabrication of Micro-Optical Elements", CLEO Pacific Rim, Taipei, (Taiwan), (2003).

3. X.-C. Yuan, W X Yu, W C Cheong, V Koudriachov, S H Tao and Q N Ngo, "Surface relief micro-optical elements built in hybrid sol-gel glass", Proceedings of SPIE. Vol. 4924, September 2002, pp.76-81.

Bibliography:

1. H. Ghafoori-shiraz and T. Asano, "Microlens for coupling a semiconductor laser to a single-mode fibre," Opt. Lett. 11, 537-539, 1986.

2. H. Honmou and M. Itoh, "Highly efficient optical coupling of laser diode array to single-mode fibre array with heat-treated hemispherical microlens," Lasers and Electro-Optics Society Annual Meeting, 1993. LEOS '93 Conference Proceedings. IEEE , 15-18 Nov 1993, 476 –477.

3. J.S. Leggatt, M.C. Hutley, "Microlens arrays for interconnection of singlemode fibre arrays ," Electronics Letters , Volume: 27 Issue: 3 , 31 Jan 1991, 238-240.

4. C.-Y.Li, J.Chisham, M.Adrews, S.I.Najafi, J.D.Mackenzie and N.Peyghambarian, "Sol-gel integrated optical coupler by ultraviolet light imprinting," Electronics Letters, Vol.31, No.4, 1995,271-272.

5. M.A.Fardad, T.Touam, P.Meshkinfam, R.Sara, X.M.Du, M.P.Andrews and S.I.Najafi, "UV-light imprinted Bragg grating in sol-gel ridge glass waveguide with almost 100% reflectivity," Electronics Letters, Vol.33, No.12, 1997, 1069-1070.

6. S.Iraj Najafi, T.Touam, R. Sara, M.P.Andrews, and M.A.Fardad, "Sol-gel Glass waveguide and grating on silicon," Journal of Lightwave Technology, Vol.16, No.9, 1998, 1640-1646.

7. Amir Fardad, Mark Andrews, Galina Milova, Ali Malek-Tabrizi, and Iraj Najafi, "Fabrication of ridge waveguides: a new solgel route," Appl. Opt. 37, 2429-2434, 1998.

8. M.A.Fardad and M.Fallahi, "Sol-Gel Multimode Interference Power Splitters," IEEE Photonics Technology Letters, Vol.11, No.6, 1999, 697-699.

9. P.Ayras, J.T.Rantala, S.Honkanen, S.B.Mendes, N.Peyghambarian, "Diffraction gratings in sol–gel films by direct contact printing," Optics Communications, Vol.16, No.2, 1999,215–218.

10. P. Ayrasa, J.T. Rantalab, R. Levya, M.R. Descoura, S. Honkanena, N. Peyghambarian, "Multilevel structures in sol-gel thin Ælms with a single UV-exposure using a grey-scale mask," Thin Solid Films, Vol.352, 1999, 9-12. Letter.

11. J.T. Rantalaa, R.S. Pennera, S. Honkanena, J. Vahakangasb, M. Fallahia, N. Peyghambarian, "Negative tone hybrid sol-gel material for electron-beam lithography," Thin Solid Films, Vol.345, 1999, 185-187. Letter.

12. J.T.Rantala, R.Levy, L.Kikimaki and M.R.Descour, "Direct UV patterning of thick hybrid glass films for micro-opto-mechnical structures," Electronics Letters, Vol.36, No.6, 2000, 530-531.

13. H.J.Jiang, X.-C.Yuan, Y.Zhou, Y.C.Chan, Y.L.Lam, "Single-step fabrication of diffraction gratings on hybrid sol-gel glass using holographic interference lithography," Optics Communications, Vol. 185, 2000, 19-24.

14. Hongjin Jiang, Xiaocong Yuan, Zhisheng Yun, Yuen-Chuen Chan, Yee-Loy Lam, "Fabrication of microlens in photosensitive hybrid sol–gel films using a grey scale mask," Materials Science and Engineering C Vol.16, 2001, 99–102.

15. X-C Yuan, H J Jiang and W C Cheong, "Characterization of photosensitive hybrid sol-gel glass with high-energy beam-sensitive scale-scale mask in single-step fabrication of blazed gratings," J. Phys. D: Appl. Phys. Vol. 34, No 23, 2001, 1-4.

16. A. M. Mailhot, A. Elyamani and R. E. Riman, "Reactive atmosphere synthesis of sol-gel heavy metal fluoride glasses", J. Mater. Res., Vol. 7, No. 6, 1992, 1534.

17. M.P. Stevens, "Polymer Chemistry", 2nd ed. (Addison-Wesley, London, United Kingdom, 1975), pp. 17, 21.

18. K. Saravanamuttu, X. M. Du, S. I. Najafi, and M. P. Andrews, "Photo-induced Structural Relaxation and Densification in Sol-Gel Derived Nanocomposite Thin Films; Implications in Integrated Optics Device Fabrication," Can. J. Chem. 76 (1998) 1717.

19. D. L. Ou and A. B. Seddon, "Near- and mid-infrared spectroscopy of sol–gel derived ormosils: vinyl and phenyl silicates", J. Non-Cryst. Solids. 210 (1997) 187.

20. Oun-Ho Park, Ji-In Jung, and Byeong-Soo Bae. "Photoinduced condensation of sol-gel hybrid glass films doped with benzil dimethyl ketal", J. Mater. Res. 16 (2001) 2143.

21. Canyon Materials Inc website: www.canyonmaterials.com.

22. Jens Neumann, Kay S.Wieking, Detlef Kip, "Direct Laser Writing of Surface Reliefs in Dry, Self-Developing Photopolymer Films," Appl. Opt. 38, 5418-5421 (1999).

23. J. T. Rantala, R. S. Penner, S. Honkanen, J. Vahakangas, M. Fallahi and N. Peyghambarian, "Sol-Gel Hybrid Glass Diffractive Element by Direct Electron-Beam Exposure," Electronics Letters 34, 455-456 (1998).

24. W. C. Cheong, X-C. Yuan, V. Koudriachov and W. X. Yu, "High sensitive SiO2/TiO2 hybrid sol-gel material for fabrication of 3 dimensional continuous surface relief diffractive optical elements by electron-beam lithography," Opt. Express 10, 586-590 (2002).

25. H.J. Jiang, X-C. Yuan,Y. Zhou, Y.C. Chan, Y.L. Lam, "Single-step fabrication of diffraction gratings on hybrid sol-gel glass using holographic interference lithography," Opt. Commun. 185, 19-24 (2000).

26. Juan Ferrera, M. L. Schattenburg, and Henry I. Smith, "Analysis of distortion in interferometric lithography" J. Vac. Sci. Technol. B 14(6), 4009-4013 (1996).

27. Danièle Blanc, Serge Pelissier, "Self-Processing of Surface-Relief Gratings in Photosensitive Hybrid Sol-Gel Glasses," Adv. Mater. 11, 1508-1511 (1999).

28. Danièle Blanc, Serge Pelissier, "Fabrication of sub-micron period diffraction gratings in self-processing sol-gel glasses," Thin Solid Films. 384, 251-253 (2001).

29. Danièle Blanc, Serge Pelissier and J. M. Bergheau, "A solid mechanics approach to surface relief formation in photosensitive hybrid sol-gel materials," Appl. Phys. A 75, 1-3 (2002).

30. J. T. Rantala, A. H. O. Kärkkäinen, J. A. Hiltunen, M. Keränen, T. Kololuoma and M. R. Descour, "UV light induced surface expansion phenomenon of hybrid glass thin films," Opt. Express. 8, 682-687 (2001).

31. Hamad S. Alhokai, "Fabrication of photoresist microlens arrays," Microelectronics, 1998. ICM '98. Proceedings of the Tenth International Conference on. 49-52 (1998).

32. R. R. A. Syms, A.S. Holmes, W. Huang, V.M. Schneider, and M. Green, "Development of the SC-RTA Process for Fabrication of Sol-Gel Based Silica-on-Silicon Integrated Optic Components," J. of Sol-Gel Science and Technology 13, 509-516 (1998).

33. Walter Däschner, Pin Long, Robert Stein, Chuck Wu, and S. H. Lee, "Cost-effective mass fabrication of multilevel diffractive optical elements by use of a single optical exposure with a greyscale mask on high-energy beam-sensitive glass," Appl. Opt. 36, 4675-4680 (1997).

34. X-C Yuan, W.X Yu, N.Q.Ngo and W. C. Cheong, "Cost-effective fabrication of microlenses on hybrid sol-gel glass with a high-energy beam–sensitive grey-scale mask," Opt. Express., Vol.10, pp. 303-308, 2002.

35. M.T. Gale, "Replication techniques for diffractive optical elements", Microelectronic Engineering, Vol.34, pp. 321-339, 1997.

36. A.Sayah,V.K.Parashar and M.A.M.Gijs, "Micro-replication of optical lenses in glass using a novel sol gel technology," Micro Electro Mechanical Systems, 2002. The Fifteenth IEEE International Conference, pp.516-519, 2002.

37. W.X.Yu, X-C Yuan, N.Q.Ngo, W.X.Que, W.C.Cheong and K. V. Koudriachov, "Single step fabrication of continuous micro-optical elements in hybrid sol-gel glass by laser direct writing," Opt. Express, Vol.10, pp. 443-448, 2002.

38. Weixing Yu and X-C Yuan, "Point-to-point UV laser direct writing initiated volume growth in hybrid sol-gel glass for 3D mcirofabrication," Optics Lett. Vol.28, No.17, 2003, 1573-1575.

39. P. Heremans , Member, IEEE, M. Kuijk, Member, IEEE, R. Vounckx, Member , IEEE, and G. Borghs, "Mushroom Microlenses: Optimized Microlenses by Reflow of Multiple Layers of Photoresist," IEEE Photonics Technology Letters, Vol.9, pp. 1367-1369, 1997.

40. Hamad H. Alhokail, "Fabrication of photoresist microlens arrays," Microelectronics, 1998. ICM '98. Proceedings of the Tenth International conference on, pp. 49-52, 1998.

41. B. P. Keyworth, D. J. Corazza, J. N. McMullin, and L. Mabbott, " Single-step fabrication of refractive microlens arrays", Appl. Opt. Vol. 36, No. 10, 2198-2202, 1997.

42. M.T.Gale, "Replication techniques for diffractive optical elements", Microelectronic Eng. Vol.34, 321-330, 1997.

43. Takashi Okamoto, Miwa Mori, Tamae Karasawa, Seiichiro Hayakawa, Iwao Seo, and Heihachi Sato, "Ultraviolet-cured polymer microlens arrays", Appl.Opt. Vol.38, No.14, 2991-2996, 1999.

44. T. R. Jay and M. B. Steen, "Preshaping photoresist for refractive microlens fabrication," in Proc. SPIE, 1993, p. 275.

45. Z. L. Liau, D. E. Mull, C. L. Dennis, and R. C. Williamson, "Large numerical- aperture microlens fabrication by one-step etching and mass transport smoothing," Appl. Phys. Lett., vol. 64, pp. 1484–1486, 1994.

46. G. M. Peake, S. Z. Sun, and S. D. Hersee, "GaAs microlens arrays grown by shadow masked MOVPE," J. Electron. Mater., vol. 26, pp. 1134–1138, 1997.

47. Y.-S. Kim, J. Kim, J.-S. Choe, Y.-G. Roh, H. Jeon, and J. C. Woo, "Semiconductor microlenses fabricated by one-step wet etching," IEEE Photon. Technol. Lett., vol. 12, pp. 507–509, May 2000.

48. M. T. Gale and K. Knop, "The fabrication of fine lens arrays by laser beam writing," in Proc. SPIE, vol. 398, 1983, pp. 347–353.

49. Z. D. Popovic, R. A. Sprague, and G. A. Neville Connell, "Technique for monolithic fabrication of microlens arrays," Appl. Opt., vol. 27, p. 1281, 1988.

50. P. Heremans, member, IEEE, J. Genoe, M. Kuijk, R. Vounckx, and G. Borghs, "Mushroom Microlenses: Optimized Microlenses by Reflow of Multiple layers of Photoresist", IEEE PHOTONICS TECHNOLOGY LETTERS, VOL. 9, NO. 10, 1367-1369, 1997.

51. Michael R. Wang and Heng Su, "Multilevel diffractive microlens fabrication by one-step laser-assisted chemical etching upon high-energy-beam sensitive glass", Opt. Lett. Vol.23, No.11, 876-878, 1998.

52. M. Fritze, M. B. Stern, and P. W. Wyatt, "Laser-fabricated glass microlens arrays", Opt. Lett. Vol.23, No.2, 141-143, 1998.

53. Daniel M. Hartmann, Osman Kibar, and Sadik C. Esener, "Optimization and theoretical modeling of polymer microlens arrays fabricated with the hydrophobic effect", Appl. Opt. Vol.40, No.16, 2736-2746, 2001.

54. Takashi Okamoto, Miwa Mori, Tamae Karasawa, Seiichiro Hayakawa, Iwao Seo, and Heihachi Sato, "Ultraviolet-cured polymer microlens arrays", Appl. Opt. Vol.38, No.14, 2991-2996, 1999.

55. M. Wakaki, Y. Komachi, and G. Kanai, "Microlenses and microlens arrays formed on a glass plate by use of a CO2 laser", Appl. Opt. Vol. 37, No. 4, 627-631, 1998.

56. H. Ghafoori-shiraz and T. Asano, "Microlens for coupling a semiconductor laser to a single-mode fibre", Opt. Lett. Vol.11, No.8, 537-539, 1986.

57. J.S.Leggatt and M.C.Hutley, "Microlens arrays for interconnection of single mode fibre arrays", Electronics Letters. Vol.27, No.3, 238-240, 1991.

58. Gohji Nakagawa, Kazunori Miura, Masao Makiuchi and Mitsuhiro Yano, "High efficient coupling between LD array and optical fibre array using Si microlens array", IEEE Photonics Technology Letters. Vol.5, No.9, 1056-1058, 1993.

59. Maria Kufner, Stefan Kufner, Pierre Chavel and Michael Frank, "Monolithic integration of microlens arrays and fibre holder arrays in poly(methyl methacrylate) with fibre self-centering", Opt. Lett. Vol.20, No.3, 276-279, 1995.

60. R. A. Modavis and T. W. Webb, "Anamorphic microlens for laser diode to single-mode fibre coupling," J. Lightwave Technol., vol. 7, pp. 780–798, July 1995.

61. Suning Tang, Ting Li, Feiming Li, Charles Zhou and Ray T.Chen, "A holographic Waveguide Microlens Array for Surface-Normal Optical interconnects", IEEE Photonics Technology Letters. Vol.8, No.11, 1498-1450, 1996.

62. G.C.Boisset, B.Robertson, W.S.Hsiao, M.R.Taghizadch, J.Simmons, K.Song, M.Matin, D.A.Tompson and D.V.Plant, "On-Die Diffractive Alignment Structures for Packaging of Microlens Arrays with 2-D optoelectronic Device Arrays", IEEE Photonics Technology Letters. Vol.8, No.7, 918-920, 1996.

63. L. G. Cohen and M. V. Schneiher, "Microlens for coupling junction lasers to optical fibres," Appl. Opt., vol. 13, pp. 94–89, 1997.

64. H.F.B.Ozelo, L.E.M. de Barros Jr, B.Nabet, L.G.Neto, M.A.Romero, J.W.Swart, "MSM photodetector with an integrated microlens array for

improved optical coupling", SBMO/IEEE MTT-S IMOC'99 Proceedings, 605-608, 1999.

65. Hao-Lin Chen, Daniel Francis, Tho Nguyen, Wupen Yuen, Gabriel Li, and Connie Chang-Hasnain, "Collimating Diode Laser Beams from a Large-Area VCSEL-Array Using Microlens Array", IEEE Photonics Technology Letter, Vol.11, No.5, 506-508, 1999.
66. Fu Yong-Qi, Ngoi Kok Ann Bryan and Ong Nan Shing, "Diffractive optical elements with continuous relief fabricated by focused ion beam for monomode fibre coupling", Opt. Express. Vol.7, No.3, 141-147, 2000.
67. S. Eitel, S. J. Fancey, H.-P. Gauggel, K.-H. Gulden, W. Bächtold and M. R. Taghizadeh, "Highly Uniform Vertical-Cavity Surface-Emitting Lasers Integrated with Microlens Arrays", IEEE Photonics Technology Letters. Vol. 12, No. 5, 459-461, 2000.
68. Yongqi Fu and Ngoi Kok Ann Bryan, "Investigation of hybrid microlens integration with vertical-cavity surface-emitting lasers for free-space optical links", Optics Express. Vol.10, No.9, 413-418, 2002.
69. H. Honmou and M. Itoh, "Highly efficient optical coupling of laser diode array to single-mode fibre array with heat-treated hemispherical microlens," Lasers and Electro-Optics Society Annual Meeting, 1993. LEOS '93 Conference Proceedings. IEEE , 15-18 Nov 1993, 476 –477.
70. J.S. Leggatt, M.C. Hutley, "Microlens arrays for interconnection of singlemode fibre arrays ," Electronics Letters , Volume: 27 Issue: 3 , 31 Jan 1991, 238-240.

71. Jun Yao, Zheng Cu , Fuhua Gao, Yixiao Zhang, Yongkang Guo, Chunlei Du, Hongjun Zeng, Chuankai Qiu, "Refractive micro lens array made of dichromate gelatin with grey-tone photolithography", Microelectronic Engineering. Vol. 57–58, 729–735, 2001.

72. Yongqi Fu and Ngoi KokAnn Bryan, "Semiconductor Microlenses Fabricated by One-Step Focused Ion Beam Direct Writing", IEEE TRANSACTIONS ON SEMICONDUCTOR MANUFACTURING, VOL. 15, NO. 2, 229-231, 2000.

73. X.M.Zhao, Y. Xia, G.M.Whitesides, "Soft lithographic methods for nano-fabrication", J.Mater.Chem, 1997, 7, 1069-1074.

74. D.Qin, Y.Xia, J.A.Rogers, R.J.Jackman, X.M.Xhao,G.M.Whitesides, "Microfabrication, microstructures and microsystems", Top.Carr.Chem, 1998, 194, 1-20.

75. G.M.Whitesides, Y.Xia, "Soft lithography", Anna. Rev.Mater.Sci 1998, 28, 153-184.

76. A.Kumar, G.M.Whitesides, "Features of gold having micrometer to centimeter dimensions can be formed through a combination of stamping with an elastomeric stamp and an alkanethiol 'ink' followed by chemical etching", Appl. Phys. Lett, 1993, 63, 2002-2004.

77. Y.Xia, E.Kim, X-M Zhao, J.A.Rogers, M.Pretiss, G.M.Whitesides, "Complex optical surfaces formed by replica molding against elastomeric masters", Science 1996, 273, 347-349.

78. X.M.Zhao, Y.Xia, G.M.Whitesides, "Fabrication of three-dimensional micro-structures: Microtransfer molding", Adv.Mater. 1996, 8, 837-840.

79. E.Kim, Y.Xia, G.M.Whitesedes, "Polymer microstructures formed by molding in capillaries", Nature.1995, 376, 581-584.

80. E.Kim, Y.Xia, X-M.Zhao, G.M.Whitesides, "Solvent-assisted microcontact molding: A convenient method for fabricating three-dimensional structures on surfaces of polymers", Adv. Mater.1997, 9, 651-654.

81. Daniel M. Hartmann, Osman Kibar, and Sadik C. Esener, "Characterization of a polymer microlens fabricated by use of the hydrophobic effect", Opt. Lett. Vol.25, Nol13, 975-977, 2001

82. Geun Young Yoon, Takahisa Jitsuno, Masahiro Nakatsuka, and Sadao Nakai, "Shack Hartmann wave-front measurement with a large F-number plastic microlens array", Appl.Opt. Vol.35, No.1, 188-192, 1996.

83. Horst, O. Falkensto¨fer, N. Lindlein, and J. Schwider, "Characterization of microlenses using a phase shifting shearing interferometer," Opt.Eng. vol.33, 2680-2686, 1994.

84. Moises Cywiak, Manuel Servýn, and Fernando Mendoza Santoyo, "Vibrating knife-edge technique for measuring the focal length of a microlens", Appl.Opt. Vol. 40, No.28, 4947-4952, 2001.

85. Alexander Buttner and Uwe D. Zeitner, "Calculation of the average lenslet shape and aberrations of microlens arrays from their far-field intensity distribution", Appl.Opt. Vol.41, No.32, 6841-6848, 2002.

86. C. Quan, S.H. Wang, C.J. Tay, I. Reading, Z.P. Fang, "Integrated optical inspection on surface geometry and refractive index distribution of a microlens array", Opt. Comm. Vol. 225, 223–231, 2003.

87. H.J. Tiziani, T. Haist, S. Reuter, "Optical inspection and characterization of microoptics using confocal microscopy", Optics and Laser in Eng. Vol.36, 403-415, 2001.

88. Ph Nussbaumyx, R V¨olkely, H P Herzigy, M Eisnerz and S Haselbeckz, "Design, fabrication and testing of microlens arrays for sensors and microsystems", Pure. Appl. Opt. Vol.6, 617-636, 1997.

89. H. Ottevaere, B. Volckaerts, J. Lamprecht, J. Schwider, A. Hermanne, I. Veretennicoff and H. Thienpont, "Two-dimensional plastic microlens arrays by deep lithography with protons: fabrication and characterization", J. Opt. A: Pure Appl. Opt. Vol.4, S22–S28, 2002.

90. Daniel Malacara, "Optical shop tesing", Second Edition, Chapter 18, pp.735.

91. M. De Angelis, S. De Nicola, P. Ferraro, A. Finizio, G. Pierattini, T. Hessler, "An interferometric method for measuring short focal length refractive lenses and diffractive lenses", Optics Communications 160 1999, 5–9.

92. Optics, 3rd Ed., Eugene Hecht, Addison-Wesley, Don Mills Ontario, pp.543-549, 1998.

93. Optics, 3rd Ed., Eugene Hecht, Addison-Wesley, Don Mills Ontario, pp.459-465, 1998.

94. Robert. R. Shannon, "The art and science of optical design", Cambridge University Press, 1997, pp.269.

95. Photonics modeling guide, user's guides, Code.V release notes of 9.2 version.

96. J. Van der Donk and P. E. Lagasse, Electron. Lett. 16, 292, 1980.

97. J. J. Gribble and J. M. Arnold, "Beam-propagation method ray equation," Opt. Lett. 13, 611-613,1988.

98. Enrico Nichelatti and Giulio Pozzi, "Improved beam propagation method equations," Appl. Opt. 37, 9-21, 1998.

99. Marcus D, "Theory of dielectric waveguide," Bell Syst. Tech. J., 56, 73.